AIR FORCE ACADEMY

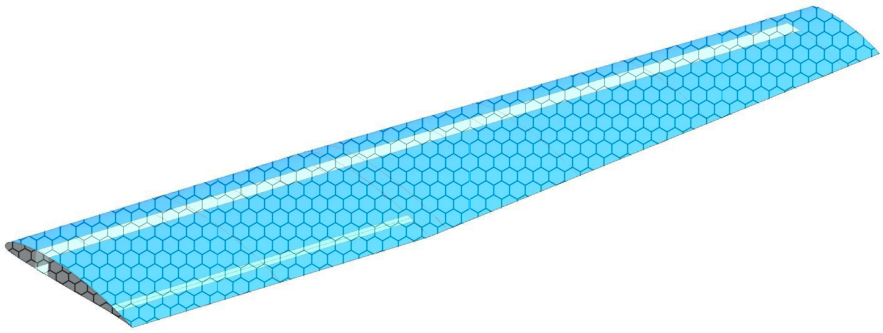

Graphene-Based Epoxy Resin Application on Laminated Composite Materials for Aeronautical Structures

António Luís Monteiro Oliveira

ALFAL/ENGAER 139925-L

Thesis to obtain the Master of Science Degree in

Military and Aeronautical Sciences - Aeronautical Engineering

Examination Committee

Chairperson:	BGEN/ENGAER 086084-A João Rui Ramos Nogueira
Supervisor:	TCOR/ENGAER 129905-A Luís Filipe da Silva Félix
Co-Supervisor:	Eng. Rui Pedro Silva
Member of the Committee:	Prof. Dr. André Calado Marta

Sintra, December 2022

Dedicated to my beloved family.

Acknowledgments

I would like to express my deepest appreciation to both my supervisors, TCOR Luís Félix and Eng. Rui Silva. Since the beginning of this thesis, they have provided enormous care for the development of this work. With their deep knowledge sharing and guidance, I was able to evolve and progress towards an even greater quality thesis. Also, their daily availability and commitment to this work, especially in its final stages, proved to be crucial to meet the delivery deadline. Moreover, their critical and constructive mindset helped me to overcome some of my difficulties in the process of making this thesis.

The completion of this thesis would have never been possible without the support of several other parties to whom I equally express my gratitude.

Special thanks to Graphenest S.A. for providing the necessary graphene-based and non-based epoxy resins. Without it, the main goal of this thesis could not have been achieved.

I am grateful to TEN Vasco Coelho for helping me during the experimental phase of this thesis, where he taught me the necessary skills on how to produce laminated composite panels, proving to be a helping hand when needed.

Many thanks to Dr. Virginia Infante and Ph.D. student João Marques for the availability to use the flexural testing machine from the Mechanical Engineering Department of *Instituto Superior Técnico* and for the help provided during the testing phase.

I am also thankful to TEN Paulo Sá for providing his wing model's CAD and FEM files, which served as the baseline design for the numerical analysis. Without them, the numerical phase of this project would have taken much longer, making it impossible to complete it on schedule.

I would like to extend my sincere gratitude to Dr. José Miranda Guedes for his precious help on the finite element analysis of laminated composites. His judgement, and know-how, proved to be fundamental during the discussion of the problems found during the computational phase.

The following acknowledgments are addressed to those who were indirectly involved in the development of this thesis, either personally or morally.

To Hapaxes, I salute you all for the difficulties we overcame together and for providing all kinds of adventures and special moments. A special thanks to my dear comrades Arriscado, Félix, Nunes, and Rocha, with whom I shared the totality of the course. Teamwork, cooperation, and resilience are some of the virtues I am proud to have acquired thanks to you, and without them, becoming an aeronautical engineer would have proven to be a more demanding challenge.

Finally, I would like to dedicate this thesis to my parents and grandparents. Their support during the last six years was, and still is, priceless. Without it, my academic and educational path would have been very different, and to them, I owe everything.

Resumo

O grafeno é um material recente, cujas propriedades permitem que este venha a substituir ou complementar outros materiais em diversas aplicações. Dada a sua elevada rigidez, este abre portas para a sua utilização em estruturas aeronáuticas, que além de verem as suas propriedades mecânicas melhoradas, permite também uma diminuição do peso destas.

O objetivo principal deste trabalho é a caraterização de materiais compósitos laminados feitos de três matrizes distintas, por forma a avaliar o impacto que o grafeno produz nas propriedades mecânicas dos laminados. Será também estudada a implementação de grafeno em estruturas aeronáuticas, mais propriamente na matriz epoxy que constitui os materiais compósitos das estruturas da asa de um veículo aéreo não tripulado de classe I ($<$ 25 kg).

Inicialmente foram realizados ensaios de tração e flexão com provetes produzidos com três matrizes diferentes: a matriz usada no Centro de Investigação da Academia da Força Aérea; a matriz aditivada com grafeno produzida pela Graphenest S.A.; e a matriz base sem grafeno, utilizada na produção da anterior. Os ensaios foram realizados com fibras de carbono bidirecionais e unidirecionais, até à rotura do material, sendo que se obtiveram melhorias de 6,2% nos módulos de elasticidade entre a matriz com grafeno e a primeira.

Por fim, estas propriedades foram utilizadas para o projeto da asa, recorrendo a uma análise por elementos finitos. Foram realizadas análises lineares de estática e de estabilidade, e comparando a matriz aditivada com a primeira, obtiveram-se diminuições de 0,6% a 6,2% nas tensões e de 6.1% no deslocamento.

Palavras-chave: grafeno, materiais compósitos laminados, ensaios experimentais, elementos finitos, veículo aéreo não tripulado.

Abstract

Graphene is a recent material whose properties allow it to replace or complement other materials in various applications. Given its high rigidity, it opens the door for its use in aeronautical structures, which apart from having their mechanical properties improved, it also allows for weight reduction of such structures.

The main objective of this work is to characterize laminated composite materials made of three different matrices, in order to evaluate the impact that graphene has on the mechanical properties of laminates. The implementation of graphene in aeronautical structures is also studied, specifically, in the design of a wing structure for a class I unmanned aerial vehicle ($<$ 25 kg).

Initially, tensile and bending tests were carried out with specimens manufactured with three different matrices: the matrix used at the *Centro de Investigação da Academia da Força Aérea*; the graphene-based matrix produced by Graphenest S.A.; and the base matrix used in the production of the previous one, but without graphene. Tests were carried out with bidirectional and unidirectional carbon fibers until material failure occurred. Improvements of 6.2% in the modulus of elasticity between the graphene matrix and the first one were obtained.

Finally, the obtained properties were implemented on the wing design, using finite element analysis. Linear static and linear buckling analyses were performed, and decreases of 0.6% to 6.2% in stress and 6.1% in displacement were obtained, when comparing the graphene-based matrix with the first one.

Keywords: graphene, laminated composite materials, experimental testing, finite element, unmanned aerial vehicle.

Contents

List of Figures

List of Tables

Abbreviations

CAD Computer-Aided Design.

CF Carbon Fibers.

CIAFA *Centro de Investigação da Academia da Força Aérea*.

CNC Computer Numerical Control.

CVD Chemical Vapor Deposition.

eVTOL Electric Vertical Take-Off and Landing.

FEM Finite Element Method.

GO Graphene Oxide.

IST *Instituto Superior Técnico*.

LPE Liquid-Phase Exfoliation.

RGO Reduced Graphene Oxide.

RT Room Temperature.

S.D. Standard Deviation.

UAV Unmanned Aerial Vehicle.

Nomenclature

Greek symbols

Δ	Parameter variation.
ε	Strain.
ε'	Strain rate.
ε_f	Flexural strain.
ν	Poisson's ratio.
ρ	Density.
σ	Stress.
σ_f	Flexural stress.
σ_{yy}	Axial stress with respect to the y-axis.

Roman symbols

A	Area.
b_1	Width.
C	Stiffness tensor.
E	Young's modulus.
E_f	Flexural modulus.
F	Applied load.
F_d	Design safety factor.
G	Shear modulus.
h	Thickness.
I_x	Area moment of inertia with respect to the x-axis.
IQR	Interquartile range.

K_C Critical stress intensity factor.

L Test span.

L_0 Gauge length.

L_3 Overall length.

$LBound$ Lower boundary.

m Mass.

M_x Bending moment with respect to the x-axis.

Q_1 First quartile.

Q_3 Third quartile.

R^2 Coefficient of determination.

S Compliance tensor.

s Deflection.

$UBound$ Upper boundary.

UT Ultimate tensile strength.

V Volume ratio.

v Volume.

v' Speed.

W Weight ratio.

x, y, z Position in the Cartesian coordinate system.

Subscripts

c Relative to the composite.

f Relative to the fiber.

h Relative to the hardener.

i, j, k, l Matrix/tensor indexes.

int Intrinsic breaking.

m Relative to the matrix.

r Relative to the resin.

WP Worst principal direction.

Superscripts

^{o}	Initial state configuration.

Chapter 1

Introduction

1.1 Motivation

With less than two decades of being discovered, graphene is a material that can provide great properties enhancements in several fields of science and engineering. Its excellent electric and thermal conductive properties, as well as mechanical properties, are some examples that can be highlighted. Furthermore, it is the strongest material, making it a hundred to three hundred times stronger than most common steels. The Graphene Council (n.d.) states that combining graphene with other materials to form new hybrid ones has great benefits. This thesis will focus on mechanical properties enhancement in aeronautical structures designs, where graphene is an excellent candidate to be incorporated in the composition of most engineering structures materials.

Aeronautics is one of the most recent branches of all transportation methods, having been created in the beginning of the past century. It has had a fast growth especially due to its application in both World Wars. During this period, engineers sought stronger and faster airplanes that could carry up their mission without failing. Wood, silk, and cotton which had previously been the major constituents of aircraft structures, were rapidly replaced by metal alloys. After the Second World War, commercial aircraft use in transportation rose, alongside with the emerging jet airplanes. Operators wanted faster, safer, and comfortable aircraft while maximizing their profits. This way, laminated composite materials started to be incorporated in aeronautical structures, replacing aluminium and other alloys. This led to the rise of flight endurance and range, materials durability, flight safety, and reduction of maintenance costs.

As can be seen in Figure 1.1, during the past five decades, Airbus jet aircraft started with a low number of composite structures used in the A300 (1974), which was the world's first commercial aircraft to employ them (Airbus, n.d.). These were mainly glass fiber fairing panels from the fin leading edge ("Composite materials in the Airbus", 1989). Since then, it increased to an all-time high of 53% of the A350's (2015) structures being made of composite materials. One of the main reasons that led to the replacement of metal alloys for composites was the weight reduction which led to increased efficiency of the aircraft. The other is related to the fiber's orientation. Depending on how forces are applied in each

structure, one can design them according to their intended behaviour.

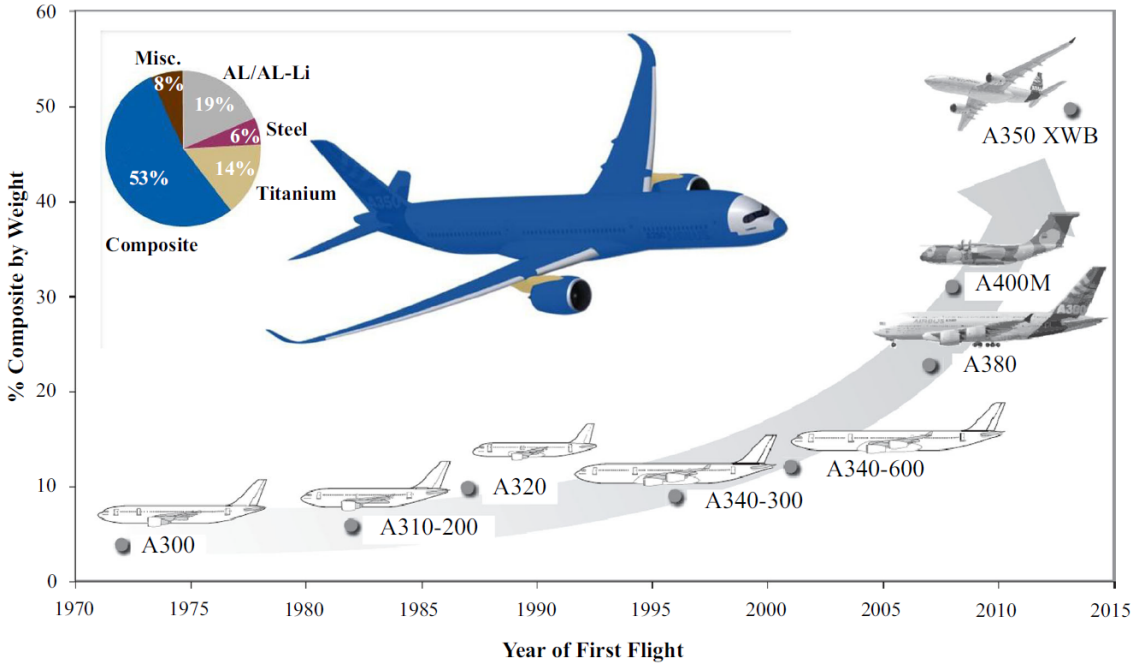

Figure 1.1: Evolution of composites usage in Airbus aircrafts. Retrieved from Xu et al. (2018).

1.2 Topic Overview

Graphene is a carbon-based material arranged in a two-dimensional honeycomb lattice (hexagonal) as can be seen in Figure 1.2. Its basic form naturally derives from graphite's delamination. Alongside fullerene and graphyne, graphene is one of the most common carbon nanomaterials. Graphene differs from the previous two because of its two-dimensional arrangement. Consisting often of a thickness of one or a few layers, meaning a nanoscale dimension, the other two generally have larger scales ("ISO/TS 80004-13:2017", 2017). Graphene can be obtained with a different number of layers, making its properties change. Monolayer graphene represents one layer, and if more are stacked one obtains few-layer graphene for two to five layers. From six to ten layers one has multilayer graphene, and for more than ten layers it is called graphene nanoplatelets (V. Kumar, Kumar, Lee, & Park, 2021).

Considering its properties, graphene has great potential for application on aircraft structures. Nonetheless, there are still challenges to overcome before graphene can become a go-to solution. Papageorgiou, Kinloch, and Young (2017) allege that high-quality and well-defined graphene production on a large scale is still a difficult task to perform. Besides that, they also state the challenge to obtain graphene's great properties while producing adequate dispersions.

Graphene can be used in different forms. In this work, graphene is manufactured and incorporated in an epoxy matrix, HexaMatrix by Graphenest S.A., a Portuguese graphene-based solutions provider.

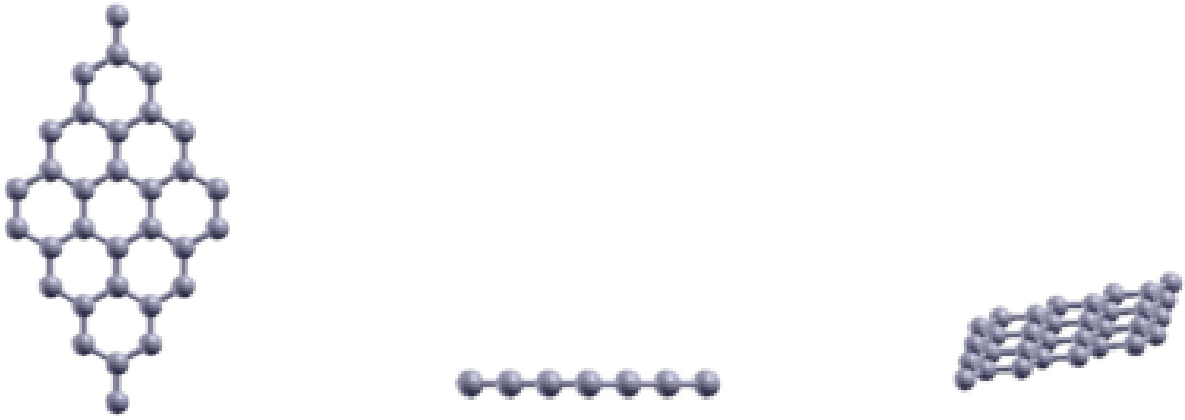

(a) Graphene top view (b) Graphene side view (c) Graphene perspective view

Figure 1.2: Graphene layer views. Retrieved from ISO/TS 80004-13:2017 (2017).

1.3 Objectives

In order to study the effect of incorporating graphene on the composite matrix, extensive experimental work will be performed. This study will determine the stress values and mechanical properties of several specimens subjected to tensile and flexural tests. In order to compare with conventional composites, HexaMatrix will be compared with SR8200, which is the epoxy matrix currently used in the *Centro de Investigação da Academia da Força Aérea* (CIAFA), and with HexaMatrix neat resin (without graphene). All specimens will be manufactured with carbon fibers (CF) used in CIAFA by hand layup.

Once the mechanical properties have been investigated, a comparative study will be conducted to determine the impact of different resins on several aircraft structures. To achieve this goal, the wing structure and its main spar from Alves et al. (2021) Class I electric vertical take-off and landing (eVTOL) unmanned aerial vehicle (UAV), with a maximum take-off weight of 25 kg, will be designed using SR8200 and HexaMatrix resins.

The main goal of this report is to evaluate the impact of graphene-based resin incorporation in the matrix of the laminated composite with carbon fibers. The study will have two main purposes:

- Evaluate the mechanical properties of laminated carbon composite specimens:
  - Build specimens containing three different resins by the hand layup method. SR8200 (currently in use in CIAFA), HexaMatrix neat resin, and HexaMatrix (with graphene);
  - Perform tensile and flexural tests using ISO standards;
  - Analyse the obtained results and conclude the final approximate mechanical properties of each laminated type;
  - Infer on the improvement of the mechanical properties due to the addition of graphene on the epoxy matrix.
- Study the impact of graphene on aircraft structure design:
  - Structural design of a UAV Class I main spar and wing, using the three resins;

– Comparison of results and discussion of the impact graphene had on the structures.

The development of this study will be aided by some software. Either the design and the finite element analysis from the computational design of the wing will be held on Siemens NX. While the analysis of data and further calculations will be made in Excel spreadsheets.

1.4 Thesis Outline

In order to reproduce the studies mentioned in the report's objectives, this thesis is structured in the following way:

Chapter 1 is the introduction to the work. It comprises the motivation for studying this material, the topic overview which introduces graphene and what will be studied about it, and also the goals and layout for the project's report.

Chapter 2 contains the state-of-the-art on graphene, laminated composite materials, and structural analysis. These are the three main pillars for the development of this thesis, and through which, bibliographic research will substantiate the obtained results.

Chapter 3 encompasses the specimens' production and testing. The mechanical properties of the materials are analysed and discussed for further use.

Chapter 4 starts with an explanation of the original wing model that will serve as the starting point for the numerical solution. It will address the implementation of the obtained laminate properties in the aeronautical structures and the results of the structure's response to the applied loads.

Chapter 5 is the conclusion of the master thesis report. It summarizes the achieved outcomes from the investigation and the difficulties found during the implementation of both parts. Recommendations for further development of the project are also given at the end of this chapter.

Chapter 2

Fundamental Concepts and State-of-the-Art

2.1 Graphene, a New Material

2.1.1 Historical Overview

Graphene is a two-dimensional monoatomic carbon allotrope, which has emerged during this present century as an exotic material, gaining worldwide attention for its exceptional thermal, optical, and mechanical properties, among others (Singh et al., 2011). Looking back through history, for centuries physicists have been discovering new elements and materials, and in the middle of the 18^{th} century, British chemist Benjamin Brodie discovered through the mixture of acids and graphite a ”carbonic acid” which was known as graphon (Dreyer, Park, Bielawski, & Ruoff, 2010). Years later, the scientific community came to know that what he had discovered was, in fact, a suspension of graphene oxide (Geim, 2012).

Over the next century, scientists made important advancements where Ulrich Hofmann and Hans-Peter Boehm investigated further graphene-oxide suspension and discovered the first carbon monolayer structures. However, due to poor characterization methodology this material could not be confirmed and/or characterized, and only in our present time could it be achieved. Graphene was first unambiguously produced and identified in 2004, by the group of Andre Geim and Konstantin Novoselov, though they credited Hanns-Peter Boehm and his co-workers for the experimental discovery of graphene in 1962, where Boehm introduced for the first time the term graphene in 1986 (Geim, 2012). Boehm, Setton, and Stumpp (1986) state that the ending term -ene is commonly used for fused polycyclic aromatic hydrocarbons, such as naphthalene and anthracene. Furthermore, a single carbon layer of the graphitic structure is the smallest part of its composition, meaning that the term graphene layer should be used for the simplest carbon structure.

Through crystallography techniques, researchers already knew that graphite was composed of stacked layers of carbon material (graphene layers), just like a deck of cards or a ream of paper. It was only a

matter of time until a scientist inevitably discovered this material.

In 2004, Professor Andre Geim and Konstantin Novoselov, at the time researchers at the University of Manchester, in the United Kingdom, applied a simple graphite peeling method. This was all achieved by just using simple adhesive tape, commonly known as the ”Scotch Tape” technique, which is a micromechanical cleavage process. This method had to be applied repeatedly to get one atom thick layers and finally obtain isolated graphene (“This Month in Physics History: October 22, 2004: Discovery of Graphene”, 2009). With this discovery, six years later, they were awarded the Nobel Prize in the field of physics.

2.1.2 Graphene Production Methods

There are several methods to synthesize graphene that can be divided into two groups. The first is top-down where macro components, such as graphite, can be reduced into smaller elements. The second is bottom-up where smaller elements are built up until graphene is obtained. While the first can cost-effectively make greater amounts of graphene, the second group can only produce smaller quantities of higher-quality graphene with higher costs (Z. Zhang, Fraser, Ye, Merle, & Barralet, 2019). Some production techniques from both methods are to be presented shortly.

2.1.2.1 Top-Down Methods

Mechanical Exfoliation

Is the process of removing layers from the original material, which is graphite, through mechanical methods. Recalling the scotch-tape method applied by Geim and Novoselov, it was one of the exfoliation types of processes. Cooper et al. (2011) state that until today, no other method can produce such high quality and high mobility graphene flakes as this one. However, this being almost a proof of concept method, it is time demanding and a limited quantity of graphene can be extracted from this. On the one hand, it can be produced with very good quality for its needs. On the other hand, it is difficult to supply the high demand that increases year after year for new applications and new products.

Liquid-Phase Exfoliation (LPE)

Liquid-phase exfoliation is the main method for cost-effective production of great-quality graphene in large amounts, being broadly adopted by academic research and the industrial sector (Li et al., 2020). In this process, graphite is converted into graphene by overcoming the van der Waals force between sheets (Allen, Tung, & Kaner, 2010).

This method has been optimized and patented by Graphenest S.A. to produce the graphene that will later be used in the epoxy matrix. It consists in applying ultrasound (cativation) on dispersed graphite in a liquid medium in order to convert graphite into graphene layers (Z. Zhang et al., 2019). Graphenest managed to increase its graphene throughput due to its patented process and continuous process optimization. Commonly, other parameters involved in the process, such as the temperature and used solvents, highly affect the exfoliation efficiency.

Chemical Oxidation-Reduction

Graphite oxidative exfoliation is considered to be one of the most promising processes to obtain graphene oxide (GO). This method consists in introducing oxygen groups in graphite, during the oxidation phase, in order to overcome the van der Waals forces, increasing the interlayer distance between graphite sheets. To obtain graphite oxide, its chemical composition and structure are controlled by the use of oxidizing agents, reaction conditions, and the synthesis procedure chosen. After this, sonication is performed in a solvent, such as ethanol or water, converting graphite oxide into GO. Then, reduction methods, such as thermal, chemical, electrochemical, or microwave, can be applied to obtain reduced graphene oxide (RGO) (N. Kumar et al., 2021).

Each of these reduction methods has different efficiencies in removing oxygen functional groups, and therefore different levels of purity (Z. Zhang et al., 2019). This approach is relatively cheaper for producing higher quantities of RGO, however, the number of defects due to the presence of oxygen will dictate its final quality.

2.1.2.2 Bottom-Up Methods

Chemical Vapor Deposition (CVD)

As for the production of large graphene sheets, this is a better method and one of the most successful, while still getting high structural quality. In CVD, carbon is supplied through synthesis gas and the graphene layer will grow on a metal that is also used as a catalyst (Cooper et al., 2011). An example of the CVD process, selecting nickel (Ni) as the substrate, consists of dissolving carbon into the metal followed by its precipitation on the substrate while cooling the last one. The product is then placed in a vacuum and high-temperature chamber with diluted hydrocarbon gas. The deposition process begins with the incorporation of small quantities of carbon atoms into the substrate. After that, carbon atoms will diffuse onto the nickel substrate and form graphene layers (Singh et al., 2011). Problems with this method can be defects and wrinkles in the material which might affect the stability of the product. All this is derived from the transfer of graphene from the growth substrate to a substrate of interest. The complexity of the process and the high energy demand can be other cons of using CVD to produce graphene (Papageorgiou et al., 2017).

Epitaxial Growth

This method uses compounds with a similar crystalline hexagonal structure to that of graphene. Graphene layers will grow continuously to the crystal structure of the substrate (Z. Zhang et al., 2019). Silicon carbide (SiC) is the most common precursor due to its crystalline hexagonal form. A thermal treatment will release silicon from the compound, leading to a rearrangement of the carbon atoms into graphene. An advantage of this method compared to the previous one is that it does not require a final transfer of graphene from the growth substrate to a different one, leading to lower defects (Coraux, N'Diaye, Busse, & Michely, 2011).

2.1.3 Graphene Structure and Mechanical Properties

In its structure, monolayer graphene is composed of just one single layer of carbon atoms, 0.335 nm thick (Tang et al., 2014), that connect each other through *sigma* bonds, which are the strongest of all covalent bonds. Each carbon atom connects to three equal atoms, and each bond is 0.142 nm in length. The connections occur in the sp2 hybridization, leaving a fourth orbital unconnected. By doing that, graphene's crystal structure forms a hexagonal lattice shape. The fourth bond is a π bond, oriented in the 3rd dimension (which is perpendicular to the graphene plane) and carbon atoms are then hybridized together to form the π- and π^*-bands. These bands are responsible for enhancing the electronic properties of graphene (Cooper et al., 2011).

Several techniques are used for characterizing graphene and identifying functional groups and/or morphological modifications on the graphene sheets: Raman, Fourier-transform infrared (FTIR), and x-ray photoelectron (XPS) spectroscopies; transmission electron (TEM), and atomic force (AFM) microscopies, and also thermogravimetric analysis (TGA) (Fraga, Sobrinho, Carvalho, & Ghislandi, 2020).

What led most investigators to race for the discovery of graphene was the possibility to drive current technologies beyond their limits, and push future applications and new technologies into our everyday lives. For this reason, most of the firsts scientific articles and journals focused on electrical properties, which presented the most groundbreaking characteristics. Eventually, with more tests being run, mechanical properties were brought to light. Besides these aforementioned properties, graphene also gathers splendid thermal and optical properties, which can be translated into very high thermal conductivity and huge transparency. Single-layer graphene absorbs only 2.3% of incident light (Nair et al., 2008). It also exhibits Quantum Hall Effect at room temperature (RT). This effect is the capacity of a solid conductor while being charged with an electric field, to produce voltage difference when a magnetic field is applied perpendicular to the electric field (Britannica, 2021). This will cause graphene to behave as a semiconductor (Flynn, 2010).

Graphene's exceptional mechanical properties are due to the structure bonds' stability which withstands in-plane deformations (Papageorgiou et al., 2017). Stiffness, strength, and toughness will be introduced according to several authors. These properties depend on several factors, such as if it is mono, few, or multilayer, its lateral size, crystallinity, and oxide reduction level. The following data is addressed to monolayer graphene produced with different methods by different authors.

Stiffness is a mechanical property which determines how flexible a material can be when subjected to an applied load. According to Lee, Wei, Kysar, and Hone (2008), graphene's elastic response is nonlinear due to the stress/strain curve having to tend to the intrinsic breaking stress. These measurements were made through a series of tests using AFM nanoindentation to measure the mechanical properties. As of conclusion from the uniaxial extension test, the authors say nonlinear effects can be ignored, thus leading to a Young's modulus value (E) of 1.0 ± 0.1 TPa.

Strength is the stress value for which a specimen breaks during a constant rate extension/load. Lee et al. (2008) found an intrinsic breaking strength value (σ_{int}) of 130 ± 10 GPa at a strain (ε_{int}) of 0.25. Intrinsic strength is defined as the strength measured in materials that do not have the presence of slow

crack growth or fatigue. This led to a higher interest in the study of brittle fracture (Kurkjian, Biswas, & Yuce, 1996).

Toughness is the capability of a material to deform and absorb energy before a fracture occurs, while under stress. Regarding fracture toughness. this is described as the necessary stress to propagate a preexisting defect and is very relevant for engineering applications (Iowa State University - Center for Nondestructive Evaluation, n.d.). A usual parameter used to represent this property is the critical stress-intensity factor K_C. P. Zhang et al. (2014), on their pre-cracked graphene tests, measured the average critical stress intensity factor (K_C) of 4.0 ± 0.6 MPa$\sqrt{m}$. Table 2.1 presents a brief summary of the monolayer graphene mechanical properties presented above.

Table 2.1: Summary of monolayer graphene mechanical properties.

E **[TPa]**	σ_{int} **[GPa]**	ϵ_{int}	K_C **[MPa**$\sqrt{m}$**]**
1.0 ± 0.1	130	0.25	4.0 ± 0.6

2.1.4 Graphene-Based Epoxy Resin

In this thesis, multilayer graphene will be mixed in the epoxy resin with a 2 wt% concentration ratio. One of the main goals explained in the introduction of this document is to study the mechanical properties improvements by adding graphene to the epoxy resin that will compose laminated composite materials. This section presents the state-of-the-art where pristine epoxy resins are compared with graphene-based ones.

M. A. Rafiee et al. (2009) made a comparative study between graphene platelets, single-walled carbon nanotubes, and multi-walled carbon nanotubes. All of them are in a concentration ratio of 0.1 wt% of resin. Graphene nanocomposites outperformed the other two. Its Young's modulus was 31% greater than the pristine epoxy resin. The ultimate tensile strength and the first mode fracture toughness also increased by 40% and 53%, respectively.

In a different study, Martin-Gallego, Bernal, Hernandez, Verdejo, and Lopez-Manchado (2013) tried different concentration ratios of functionalized graphene sheets in the epoxy resin. They determined the Young's modulus and the ultimate tensile strength for 0, 0.25, 0.5, 0.75, and 1.5 wt%, and the last one got the best scores of all. Young's modulus grew more than 50% from 1.63 GPa (0 wt%) to 2.47 GPa (1.5 wt%). As for the strength it showed an increase from 58.9 MPa (0 wt%) at an extension of 5.9% to 68.5 MPa (1.5 wt%) at 3.7%. Which means it increased more than 16%, while the extension decreased approximately 2%.

Regarding graphene nanoplatelets produced by Graphenest S.A. and mixed with Sicomin SR 8100 epoxy resin and SD 8100 hardener, Parente et al. (2022) performed bending tests on the matrix containing different graphene concentrations and pre-cured at different temperatures. Figure 2.1 presents the obtained results from the study. In general, better results can be obtained with a half-term concentration between 0 and 1 wt%. Higher bending stress can be obtained for lower pre-cure temperatures, while higher stiffness can be achieved with temperatures around 25 to 30 ℃.

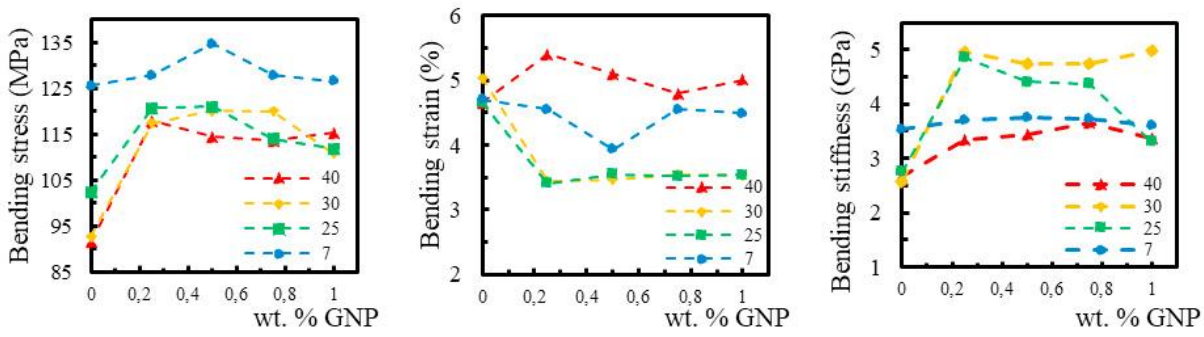

(a) Bending Stress. (b) Bending Strain. (c) Bending Stiffness.

Figure 2.1: Effect of graphene concentration on the epoxy matrix and pre-cure temperature. Retrieved from (Parente et al., 2022).

2.1.5 Laminated Composite Materials Using Graphene-Based Epoxy Resin

Mechanical properties values previously mentioned represent only the graphene-based epoxy resin. Besides the previously mentioned parameters, such as graphene production methods and the epoxy matrix used, new parameters will be added to this section leading to a large spectrum of how to apply graphene in laminated composite materials. Only carbon fiber reinforcements are to be used in the composition of the laminates. Still, different types of stacking and ply orientations can be applied, where the type of fiber yarn entanglement is also a process variable.

Thorough research on experimental results on laminated composites using graphene-based matrix led to little results similar to what is to be tested. Most will include graphene incorporation in the fibers, or the use of carbon nanotubes or GO instead of purer forms of graphene.

Shokrieh and Kondori (2020) tensile tested the longitudinal and transversal directions of unidirectional carbon fibers reinforced with an epoxy matrix containing 0, 0.1, 0.25, and 0.5 wt% of graphene nanoparticles. Toray T300 unidirectional carbon fibers with 12K filaments per tow were used. Specimens were produced via the hand layup method. Table 2.2 presents the obtained tensile results of the epoxy matrix and both laminate directions.

Table 2.2: Unidirectional carbon laminates' Young's modulus. Retrieved from (Shokrieh & Kondori, 2020).

Graphene Concentration [wt%]	$E_{\mathbf{m}}$ **[GPa]**	$E_{\mathbf{longitudinal}}$ **[GPa]**	$E_{\mathbf{transversal}}$ **[GPa]**
0	2.51	92.25	4.95
0.1	2.74	92.37	5.39
0.25	2.93	92.46	5.76
0.5	2.95	92.47	5.80

Katti et al. (2021) performed tensile tests on bidirectional carbon fiber mats reinforced with epoxy

resin containing GO. One of the experiments had epoxy chains previously grafted onto GO, and only then GO was incorporated into the epoxy matrix. The fiber stacking was $[0/90]_8$, and laminates were produced via vacuum infusion. Table 2.3 presents the laminates' 0° direction (longitudinal) ultimate tensile strength (UT) and Young's modulus.

Table 2.3: Bidirectional carbon laminates' ultimate tensile strength and Young's modulus. Retrieved from (Katti et al., 2021).

Laminates	UT_1 **[MPa]**	E_1 **[GPa]**
Epoxy + CF	733	64
Epoxy + CF + GO	778	66
Epoxy + CF + Epoxy grafted GO	822	65

2.1.6 Applications in Aeronautical Structures

In a wide range of fields for graphene applications, one can highlight some avionic uses: the replacement of silicon used in field effect transistors; application in energy storage and conversion devices, in solar cells, photodetectors, and many more ("This Month in Physics History: October 22, 2004: Discovery of Graphene", 2009)(Singh et al., 2011).

Continuing with the line of thought of the motivation for this thesis, graphene can be applied in two different ways. The first comprises the addition of graphene to the epoxy resin to improve the resin's mechanical properties. The second is graphene-reinforced carbon fibers, where strength and stiffness can both be enhanced compared to traditional carbon fibers (M. Rafiee, Nitzsche, Laliberte, Thibault, & Labrosse, 2019). In both methods, graphene allows the decrease of the structural weight. This leads to more efficient aircraft, thus creating cleaner aircraft with lower emissions.

Adding graphene to structures could also enable electrical signals to propagate through it, leading to the concept of smart structures. These could carry data signals while stress and strain could be measured during the flight due to this multifunctional properties of graphene. From a more extreme point of view, graphene can be used for self-healing structures. Defects in its lattice can be repaired at the atomic level by simply applying new graphene mixed with other materials (Aerospace Technology Institute & The University of Manchester, 2018).

Besides graphene being incorporated in structural materials, it can also be present as an aircraft paint coating. Due to graphene's electrical properties, special coatings have been developed to bridge radar detection, decreasing aircraft radar cross-section and making it more stealth to enemy radars. They can reduce drag and be used in de-icing systems. These coatings can also provide lightning strike protection, and the fact that graphene can provide hydrophobicity for repelling water means it can also reduce corrosion in structures. It can also relate to the propulsion system where graphene can integrate fuel cells and batteries that can have their lifespan improved and get faster cycle times (Aerospace Technology Institute & The University of Manchester, 2018).

2.2 Laminated Composite Materials

In this section, the laminated composite production and their mechanical properties testing will be addressed. This information is used to characterize the materials for the wing structure design.

2.2.1 Production Method

A composite material comprises two or more materials to create one new material (Dorworth et al., 2009). Benefiting from the properties of both materials, one can adapt the end product to the application requirements. Laminated composites are fiber reinforcements bonded together by a matrix material to form a stack of plies. Different types of fiber and matrices can be used during the production phase, where the number of plies can be adjusted in accordance with the desired mechanical properties.

The three most common types of fibers used on laminated composites are carbon, glass, and aramid fibers. The objective is to discover the mechanical properties of carbon fiber-reinforced laminates, but glass fibers will also be used in the experimental methodology as gripping tabs. Two different types of carbon fibers, produced by Rebelco, were selected for the proposed methodology: bidirectional plain weave and unidirectional tape.

As for the matrix, epoxy resin systems are used, which are the focus of this study. Table 2.4 shows a summary of the material that will be used to manufacture the laminated composite specimens. From now on, each matrix will be referred to as Resin 1, 2, and 3, as presented in the table.

Table 2.4: Composites for the production of laminates.

Fibers	Bidirectional Carbon Fabric, 3K, High Strength, Plain Weave, 160 g/m^2
	Unidirectional Carbon Tape, 6K, High Resistance, 215 g/m^2
Resin 1	Sicomin SR 8200 + Hardener: SD 7206
Resin 2	Graphenest pristine HexaMatrix (no graphene)
Resin 3	Graphenest HexaMatrix

Several methods and techniques can be employed to manufacture laminated composites. Some use open molding, where the material is exposed to room conditions during the production. Others use close molding which means ambient conditions can be controlled, and usually, the mold shapes both sides of the laminate (Dorworth et al., 2009).

Wet layup molding is the method chosen for the preparation of the specimens. Usually, the resin is impregnated into the fibers using a roller or a squeegee (see Figure 2.2(a)). The use of vacuum bagging, which is a closed molding process, enhances the quality of the final product by aiding the impregnation process and removing the epoxy resin excess from the produced composite laminates (see Figure 2.2(b)). This will guarantee the compaction and consolidation of the laminate plies by means of a pressure difference between the inside and the outside of the bag. Several films are placed in between the laminate and the vacuum bag. The bleeder/breather mechanism allows for an excess of the matrix

to be removed from the laminate, while other films can be used to enhance properties that modify the final laminate (Dorworth et al., 2009).

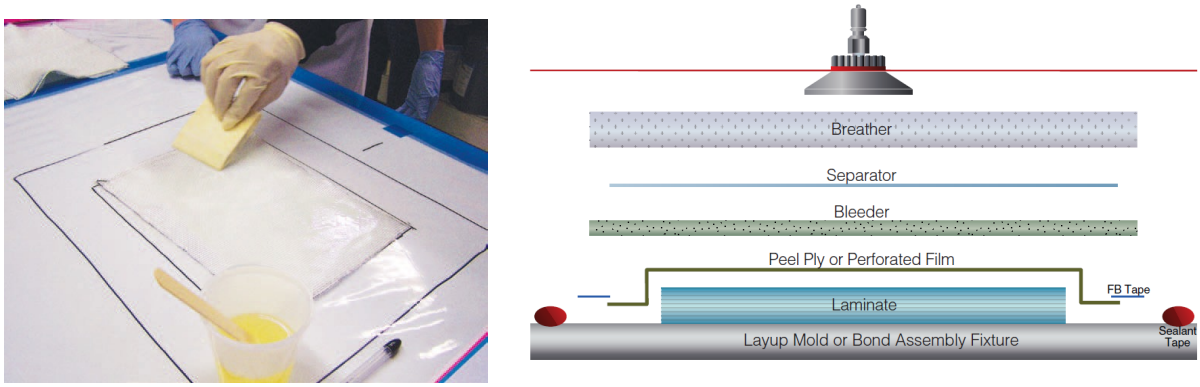

(a) Hand layup - Wet layup

(b) Vacuum bagging

Figure 2.2: Production method. Retrieved from Dorworth et al. (2009).

2.2.2 Mechanical Testing

Through thorough testing based on ISO standards, specimens will be subjected to tensile and bending tests carried out at the laboratory in order to determine their mechanical properties. These standards also explain how to build such specimens according to each required test, namely their sizes, thicknesses, and ply orientation.

2.2.2.1 Tensile Testing

The purpose of this test is to obtain the stress-strain response of a constant rectangular laminated cross-section area subject to a traction or compression force. After obtaining the laminated response, one can calculate the specimen's material properties, which are the ultimate tensile strain and stress, the tensile modulus of elasticity, and the Poisson's ratio.

For bidirectional carbon reinforcements, ISO/DIS 527-4 (2020a) standard defines that samples must have a minimum of 5 specimens per test condition. The standard also defines four types of test specimens depending on the type of composite and the usage of tabs. Type 3 specimens were chosen for the experiments. The minimum dimensions for a laminated bidirectional fiber composite are presented in Table 2.5.

Specimens composed of unidirectional fiber have their production specifications mentioned in ISO/DIS 527-5 (2020b). This standard also states that a minimum of 5 specimens per test condition must be tested. For this case, type A specimens are to be produced according to specifications presented in Table 2.5.

Table 2.5: Tensile specimen geometry recommendations. Adapted from ISO/DIS 527-4 (2020a) and ISO/DIS 527-5 (2020b).

Figure 2.3 Symbol's	Designation	Type 3 [mm]	Type A [mm]
L_3	Overall Length	250	250
L_2	Distance between end tabs	150 ± 1	150 ± 1
b_1	Width	25 ± 0.5	15 ± 0.5
h	Thickness	2	1 ± 0.2
L_0	Gauge Length	50 ± 1	50 ± 1
L	Initial distance between grips	150 ± 1	136
L_t	Length of end tabs	50	50
h_t	Thickness of end tabs	1	1

Another aspect to be considered for the manufacturing of specimens is the tabs requirements to help grab the coupon to the machine while testing it. Figure 2.3 shows the specimen's dimensions with these tabs according to Table 2.5.

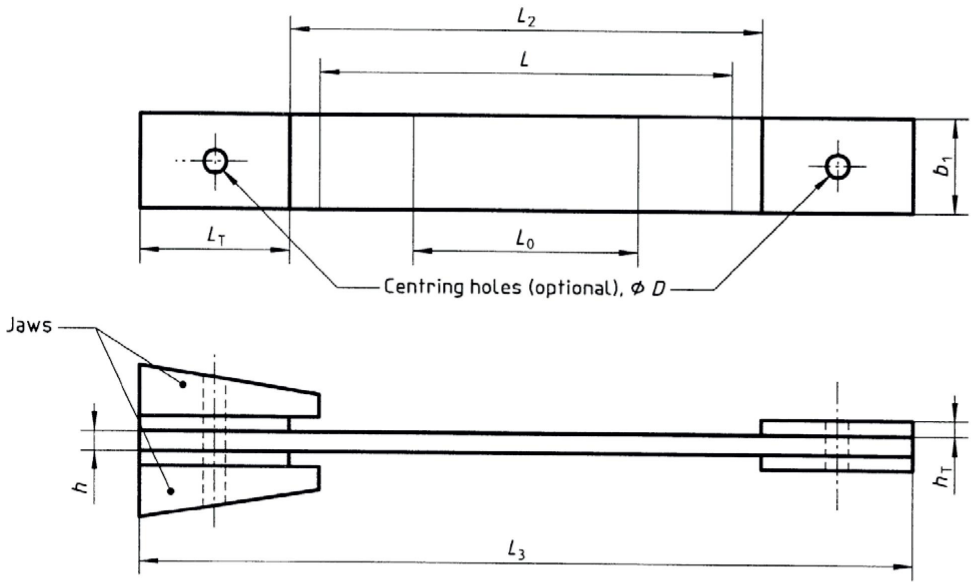

Figure 2.3: Tension test dimensions. Retrieved from ISO/DIS 527-4 (2020a).

The test speed for tensile testing is 2 mm/min. In order to calculate the specimen's mechanical properties, the following equations given by the ISO 527-1 (2019) are presented. The first eq. (2.1) shows how to calculate the tensile stress (σ) for each data point in MPa, where F represents the applied load in N, and A the average cross-section area in mm^2.

$$\sigma = \frac{F}{A} \tag{2.1}$$

To calculate tensile and ultimate tensile strains, an extensometer is required to be positioned in the

center of one of the two laminate sides. Strain (ε), dimensionless, can be deduced by the displacements measured in the extensometer via eq. (2.2), where ΔL_0 represents the increase of the specimen length between the gauge marks, expressed in mm, and L_0 is the gauge length of the test specimen, also expressed in mm.

$$\varepsilon = \frac{\Delta L_0}{L_0} \tag{2.2}$$

Despite being the most correct method to obtain the extensions, the fact that every time a test was run an extensometer would break revealed to be an expensive methodology. A proposed alternative method was to simply measure the displacement of the testing machine grips and estimate the laminate extension. This method can lead to some measurement errors associated such as short tabs slippage from the clamps during testing, and grips displacement which includes machine clearances and deformation.

Engineering stress and strain were calculated since only initial lengths and areas were considered. The instantaneous specimen cross-section area for the calculation of true stress and the instantaneous length for the true strain value was not considered. Though a true stress-strain curve was more appropriate for material property analysis, the opposing method was better for determining the ultimate tensile strength of the material and was easier to calculate (Brandon, 2020). Adding that, both results are the same for elastic behaviour analysis.

The tensile modulus of elasticity, also known as Young's modulus (E), is a measure of the material's stiffness. It is calculated as the ratio of the two previous parameters, the tensile stress and the tensile strain, for the elastic region, as shown by eq. (2.3). For the case of computer-aided equipment, a linear regression can be applied to the strain interval $0.0005 \leq \varepsilon \leq 0.0025$. The Young's modulus corresponds to the slope of the regression equation.

$$E = \Delta\sigma/\Delta\epsilon \tag{2.3}$$

Poisson's ratio (ν) relates the strain in the transverse axis with the one in the longitudinal axis where tension is applied. In order to measure this property, an extensometer positioned along the transversal direction would be required. However, since the extensometer will not be used due to the above mentioned reasons, Poisson's ratio was not estimated.

2.2.2.2 Flexural Testing

In order to obtain flexural mechanical properties, bending tests are required. ISO 14125:1998 + AC:2002 + A1:2011 (2011) shows two different ways to obtain them, which are three-point (method A) and four-point (method B) loading tests. Method A, presented in Figure 2.4(a), shows a load F being applied at the top center of the specimen. In method B, the load is applied at two different points equally distanced from the beam's center, just as Figure 2.4(b) shows. In both cases, the beam is simply supported at its ends.

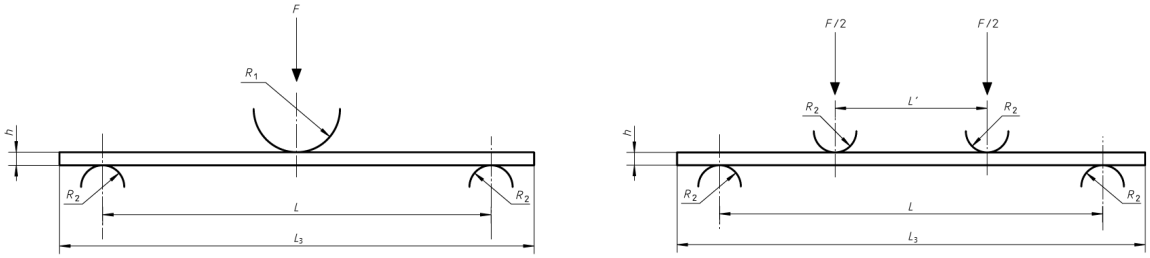

(a) Method A - three-point system.

(b) Method B - four-point system.

Figure 2.4: Loading diagrams. Adapted from ISO 14125:1998 + AC:2002 + A1:2011 (2011).

In this work, a three-point bending test set was used. According to the standard, the two procedures give slightly different property values. One major difference between both configurations is the location of the maximum bending moment and maximum flexural stress. In the four-point loading system, the bending moment is constant, and consequently, the flexural stress is uniform, between both loading points. Whereas in the three-point loading system both maximum values occur in the force application point on the beam. Another difference is the nonexistence of resultant vertical shear force between both application points in the four-point configuration. In the three-point configuration, the resultant only cancels at the center of the beam, where force is applied.

The standard refers a minimum number of five specimens must be tested. As for the test specimen's dimensions, there are four different classes based on fiber's alignment and material. Class IV specimen's dimension has been chosen since they are related to unidirectional and multidirectional carbon fiber composites. This standard values apply to all specimens being tested and are shown in Table 2.6. Figure 2.4(a) also shows the geometric specifications for the specimen.

Table 2.6: Bending specimen geometry recommendations. Retrieved from ISO 14125:1998 + AC:2002 + A1:2011 (2011).

Figure 2.4(a) Symbol's	**Designation**	**Class IV [mm]**
L_3	Specimen Length	$100 + 10$
L	Test Span	80 ± 1
b_1	Width	15 ± 0.5
h	Thickness	2 ± 0.2
R_1	Loading Member's Radius	5 ± 0.2
R_2	Support's Radius	2 ± 0.2

As for the speed (v'), it can be calculated from eq. (2.4). It depends on the method and the class of the specimen. The speed value shall be selected from Table 1 of ISO 14125:1998 + AC:2002 + A1:2011 (2011) that gives a strain rate (ε') as close to 0.01. The speed defined for the test is 5 mm/min.

$$v' = \frac{\varepsilon' L^2}{6h} \tag{2.4}$$

Flexural properties can be obtained from the following equations, where values from Table 2.6 will be used. For three-point bending, the maximum flexural stress (σ_f), which occurs at the mid-span's outer surface, can be obtained by the formula in eq. (2.5).

$$\sigma_f = \frac{3FL}{2b_1h^2} \tag{2.5}$$

The flexural strength is the maximum stress at the outer surface, obtained from the previous equation, before the specimen's failure. Also at the mid-span's outer surface occurs the maximum flexural strain (ε_f), and it may be calculated by eq. (2.6), where s is the specimens deflection.

$$\varepsilon_f = \frac{6sh}{L^2} \tag{2.6}$$

To calculate the flexural modulus (E_f) one must obtain the deflections for strains $\varepsilon_f = 0.0005$ and $\varepsilon_f = 0.0025$, and the corresponding applied force. These are directly obtained from the experimental results. Then, through eq. (2.7) one can calculate E_f.

$$E_f = \frac{L^3}{4b_1h^3}\frac{\Delta F}{\Delta s} \tag{2.7}$$

2.2.3 Statistical Analysis

All ISO Standards recommend five specimens per test to be built. However, since it is pretended to have a reliable data sample to infer the final mechanical properties, it is required to have a higher number of specimens, produced in different batches. The document produced by Tomblin et al. (2003) and released by the Federal Aviation Administration, provides the A-basis and the B-basis methods for qualification to help ensure the control on getting composite material properties and the processes to apply them in aircraft products.

This means, for the present test, a wider range of specimens must be built. The reduced B-basis requires a higher number of specimens to be built compared to the five proposed by the standards. This method includes specimens from different batches in order to account for raw materials and manufacturing uncertainties.

Reduced B-basis method requires 3 batches, each of them composed of 2 panels, having 3 specimens in each panel, which gives a total number of 18 specimens per test condition, as shown in Figure 2.5.

In this work, because of cost constraints, different materials batches were not used for specimens' manufacture. Therefore, it was previously decided to produce 10 specimens per test condition from two panels of the same material batch.

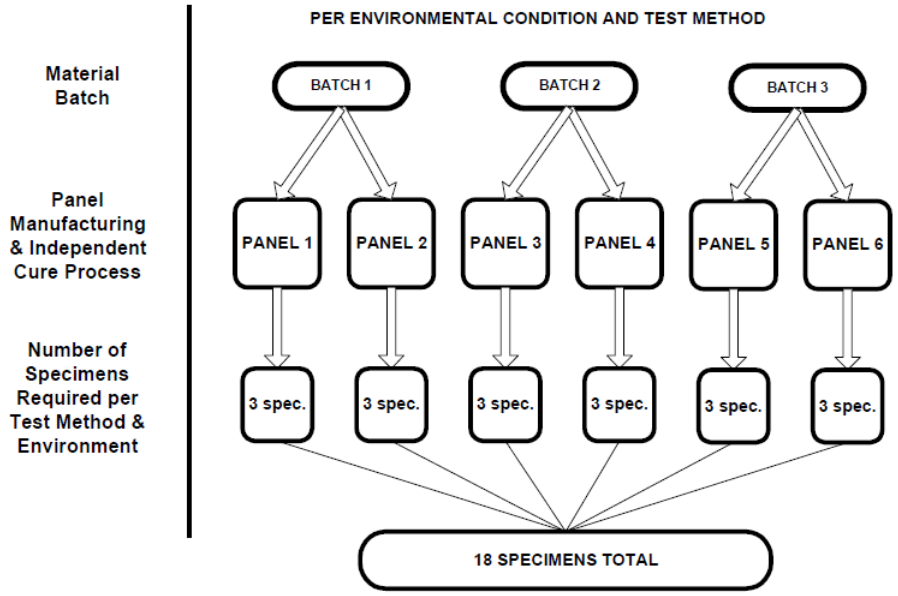

Figure 2.5: Specimen selection methodology and traceability. Retrieved from Tomblin et al. (2003)

2.3 Structural Analysis

In this section, the relation between the material model and the mechanical properties obtained for further computational use is explained. Ply failure criteria and linear analyses to be performed are briefly explained.

2.3.1 Constitutive Equations

Solid materials' mechanical properties follow stress-strain relations, which are called constitutive equations or constitutive relations. These equations characterize the applied load reaction of an individual material (Reddy, 2004). Furthermore, these equations are only applied to the material's elastic regime.

Material body stress (σ_{ij}) and strain (ε_{ij}) states can be defined by their respective tensors. These are represented in eqs. (2.8) and (2.9), relative to a three-dimensional Cartesian coordinate system.

$$\sigma_{ij} = \begin{bmatrix} \sigma_{11} & \sigma_{12} & \sigma_{13} \\ \sigma_{21} & \sigma_{22} & \sigma_{23} \\ \sigma_{31} & \sigma_{32} & \sigma_{33} \end{bmatrix} \tag{2.8}$$

$$\varepsilon_{ij} = \begin{bmatrix} \varepsilon_{11} & \varepsilon_{12} & \varepsilon_{13} \\ \varepsilon_{21} & \varepsilon_{22} & \varepsilon_{23} \\ \varepsilon_{31} & \varepsilon_{32} & \varepsilon_{33} \end{bmatrix} \tag{2.9}$$

For a linear constitutive model, generalized Hooke's law is defined by eq. (2.10). The stress tensor is proportionally related to the strain tensor through the stiffness tensor (C), plus the initial stress state configuration (σ_{ij}^0).

$$\sigma_{ij} = C_{ijkl}\varepsilon_{ij} + \sigma_{ij}^0 \tag{2.10}$$

Since stress and strain tensors are symmetric the stiffness tensor is also symmetric. Assuming that the solid material is hyperelastic (Reddy, 2004), this leads to a decrease in the number of independent stiffness components from 81 to 21. For further simplifications, it is assumed that the body's initial configuration is stress and strain free, $\sigma_{ij}^{0} = 0$. Eq. (2.11) presents the simplified Hooke's law.

$$\sigma_{ij} = C_{ij}\varepsilon_{ij} \tag{2.11}$$

The inverse equation, eq. (2.12), can also be applied through the inverse of the stiffness tensor, which is the compliance tensor (C), $S = C^{-1}$.

$$\varepsilon_{ij} = S_{ij}\sigma_{ij} \tag{2.12}$$

Therefore, an anisotropic material is a body that has different mechanical properties' values for each of its directions. This means that values are direction-dependent (Reddy, 2004). Eq. (2.12) can be expanded into the matrix notation shown by eq. (2.13).

$$\begin{Bmatrix} \varepsilon_{11} \\ \varepsilon_{22} \\ \varepsilon_{33} \\ 2\varepsilon_{23} \\ 2\varepsilon_{13} \\ 2\varepsilon_{12} \end{Bmatrix} = \begin{bmatrix} S_{11} & S_{12} & S_{13} & S_{14} & S_{15} & S_{16} \\ S_{21} & S_{22} & S_{23} & S_{24} & S_{25} & S_{26} \\ S_{31} & S_{32} & S_{33} & S_{34} & S_{35} & S_{36} \\ S_{41} & S_{42} & S_{43} & S_{44} & S_{45} & S_{46} \\ S_{51} & S_{52} & S_{53} & S_{54} & S_{55} & S_{56} \\ S_{61} & S_{62} & S_{63} & S_{64} & S_{65} & S_{66} \end{bmatrix} = \begin{Bmatrix} \sigma_{11} \\ \sigma_{22} \\ \sigma_{33} \\ \sigma_{23} \\ \sigma_{13} \\ \sigma_{12} \end{Bmatrix} \tag{2.13}$$

Two material cases will be presented according to their planes of symmetry.

Orthotropic Materials

For the case of a material that has three orthogonal planes of symmetry, the stiffness and compliance independent components will be reduced to nine. Also, some matrix entries will be zero. Replacing the compliance matrix coefficients with the corresponding engineering constants, one obtains the matrix eq. (2.14). E, G, and ν are the Young's modulus, shear modulus, and the Poisson's ratio, respectively, for the direction/plane denoted by their subscript.

$$\begin{Bmatrix} \varepsilon_{11} \\ \varepsilon_{22} \\ \varepsilon_{33} \\ 2\varepsilon_{23} \\ 2\varepsilon_{13} \\ 2\varepsilon_{12} \end{Bmatrix} = \begin{bmatrix} \frac{1}{E_1} & -\frac{\nu_{21}}{E_2} & -\frac{\nu_{31}}{E_3} & 0 & 0 & 0 \\ -\frac{\nu_{12}}{E_1} & \frac{1}{E_2} & -\frac{\nu_{32}}{E_3} & 0 & 0 & 0 \\ -\frac{\nu_{13}}{E_1} & -\frac{\nu_{23}}{E_2} & \frac{1}{E_3} & 0 & 0 & 0 \\ 0 & 0 & 0 & \frac{1}{G_{23}} & 0 & 0 \\ 0 & 0 & 0 & 0 & \frac{1}{G_{13}} & 0 \\ 0 & 0 & 0 & 0 & 0 & \frac{1}{G_{12}} \end{bmatrix} \begin{Bmatrix} \sigma_{11} \\ \sigma_{22} \\ \sigma_{33} \\ \sigma_{23} \\ \sigma_{13} \\ \sigma_{12} \end{Bmatrix} \tag{2.14}$$

Since the stiffness matrix is symmetric, and the inverse of a symmetric matrix is also symmetric, this means that the compliance matrix is symmetric too. Thus, eq. (2.14) can be simplified by replacing the following entries from eq. (2.15) with their equal.

$$\frac{\nu_{21}}{E_2} = \frac{\nu_{12}}{E_1}, \frac{\nu_{31}}{E_3} = \frac{\nu_{13}}{E_1}, \frac{\nu_{32}}{E_3} = \frac{\nu_{23}}{E_2} \tag{2.15}$$

Thereby the nine independent components are the ones given by eq. (2.16).

$$E_1, E_2, E_3, G_{23}, G_{13}, G_{12}, \nu_{12}, \nu_{13}, \nu_{23} \tag{2.16}$$

Isotropic Materials

When an infinite number of planes of material symmetry occurs, one obtains the relations presented in eq. (2.17).

$$E_1 = E_2 = E_3 \equiv E, \;\; G_{12} = G_{13} = G_{23} \equiv G, \;\; \nu_{12} = \nu_{13} = \nu_{23} \equiv \nu \tag{2.17}$$

In this case, there is a specific relation between the three components represented by eq. (2.18). This means that for isotropic materials, the number of independent components is reduced to just two.

$$G = \frac{E}{2(1+\nu)} \tag{2.18}$$

Therefore, strain-stress relations for an isotropic material are given by eq. (2.19).

$$\begin{Bmatrix} \varepsilon_{11} \\ \varepsilon_{22} \\ \varepsilon_{33} \\ 2\varepsilon_{23} \\ 2\varepsilon_{13} \\ 2\varepsilon_{12} \end{Bmatrix} = \begin{bmatrix} \frac{1}{E} & -\frac{\nu}{E} & -\frac{\nu}{E} & 0 & 0 & 0 \\ -\frac{\nu}{E} & \frac{1}{E} & -\frac{\nu}{E} & 0 & 0 & 0 \\ -\frac{\nu}{E} & -\frac{\nu}{E} & \frac{1}{E} & 0 & 0 & 0 \\ 0 & 0 & 0 & \frac{1+\nu}{E} & 0 & 0 \\ 0 & 0 & 0 & 0 & \frac{1+\nu}{E} & 0 \\ 0 & 0 & 0 & 0 & 0 & \frac{1+\nu}{E} \end{bmatrix} \begin{Bmatrix} \sigma_{11} \\ \sigma_{22} \\ \sigma_{33} \\ \sigma_{23} \\ \sigma_{13} \\ \sigma_{12} \end{Bmatrix} \tag{2.19}$$

2.3.2 Failure Criteria

Several theories can be applied to predict laminate failure while under stress. The most simple ones address only the first ply failure and not the complete laminate failure. On one hand, maximum stress and strain criteria assume that failure occurs if the material's stress and strain attain the corresponding limit value. These are the tensile, compressive, and shear stress and strain limits and these can be obtained from experimental tests on the material. On the other hand, a couple of polynomial criteria, such as the Tsai-Hill and Tsai-Wu theories, provide a correlation between the above-mentioned stress limits in a quadratic inequation. The difference between both is that Tsai-Hill assumes tensile and compressive limits to be the same, while Tsai-Wu differentiates them (Herakovich, 1998).

Taking into account that only tensile and flexural tests were performed and that carbon fiber-reinforced composites have a brittle behaviour (Swolfs et al., 2015), a similar approach to the maximum stress criterion was chosen for the numerical analysis. Samuel and Weir (1999) state that the maximum principal stress failure predictor defines that brittle materials' failure occurs whenever the maximum principal

stress, due to a multiaxial stress system, exceeds the material's strength.

Two possible cases arise. The first is principal directions being aligned with the stacking directions, which means there are no shear stresses. Thus axial stress can be directly evaluated by the tensile strength obtained from the experiments. The second is related to the principal directions not being the same as the stacking ones. This leads to axial stresses in the stacking direction being lower than the principal stresses, while shear stress occurs. Since no shear testing was performed on the materials, the shear strength limit was not evaluated in the numerical analysis for failure purposes. Relating to the axial stress in the stacking directions, both cases are conservative for the maximum principal stress criterion, which means, axial stress in the stacking directions was never higher than the maximum principal stress.

In eq. (2.20), the maximum principal stress ($|\sigma|$), which is considered tensile or compressive, must be lower than the ultimate tensile strength (UT) obtained in the experimental tests, considering a laminate composite design safety factor (F_d).

$$|\sigma| \leq \frac{UT}{F_d} \tag{2.20}$$

2.3.3 Numerical Analysis

Over the course of time, engineers have developed mathematical models to describe physical processes, using the laws of physics through algebraic, differential, and integral equations (Reddy, 2006). As computer processing was introduced, more complex equations could be solved in significantly lower process times. The combination of numerical methods and computer processing is called numerical simulation.

In order to simplify the wing model analysis, instead of producing the structure and performing tests on it, one can previously design it using Computer-Aided Design (CAD) software and then simulate the applied loads to obtain the results. The Finite Element Method (FEM) is one of the numerical simulation methods that allow one to obtain approximate solutions of the real structure's response. In this thesis, the software Siemens NX, which allows for CAD design, is used.

For the case of laminates, shell elements, which represent the 2D surface of the structure were chosen for the structure's mesh. Meshes are mainly composed of quadrilateral elements (see Figure 2.6(b)) since greater accuracy can be achieved, while triangular elements (see Figure 2.6(a)) have low usage. These are mainly for modelling transitions on the mesh or for regions where quadrilateral elements do not fit (Siemens, 2019). Only first order elements, also called linear, were used.

The size of the elements is determined by the user. For the first analysis, one must perform a mesh refinement in order to obtain the result's convergence. This means that the size of the elements must be reduced to guarantee that the final results are not varying. Elements with great size might lead to inaccurate results, while too small elements can lead to great processing times.

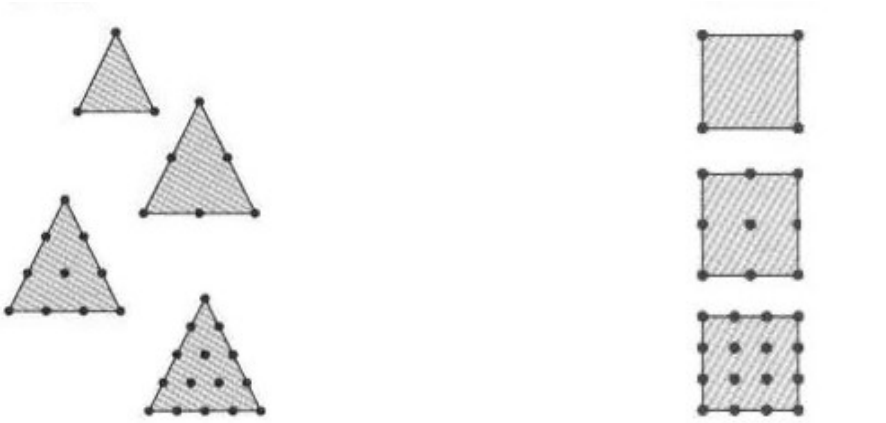

(a) Triangular elements (b) Quadrilateral elements

Figure 2.6: Examples of shell elements. Retrieved from Reddy (2006).

Two different analyses will be performed on the UAV main spar and wing structures. The first will be a linear static analysis and the second a linear buckling analysis.

Linear Static Analysis

In order to obtain stress and strain values due to an applied load, one can perform a linear static analysis. This assumes the geometric linearity hypothesis, where obtained results are linearly proportional to the applied loads. One can also obtain from this analysis the nodal displacements and rotations, and the constraint reaction's force and moment.

A linear analysis is performed since only the elastic range of the materials is analysed and deformation is assumed to be small. For first estimates, before performing nonlinear analyses, linear statics are often used. Nonlinear analyses are often used to study nonlinear effects associated with the structure's large deformations and the material's yielding (Femto Engineering, 2022).

Linear Buckling Analysis

This type of analysis is associated with compressive loads that lead to instability phenomena and consequential deformations. Linear buckling analysis does not assume a geometric linearity hypothesis. It allows to obtain the relative buckling loads. This parameter can be multiplied by all applied loads in the structure to obtain the buckling loads that lead to the structure's instability. For a relative buckling load lower than one, the structure will suffer from buckling effects.

Different buckling deflection patterns can be obtained. This corresponds to the buckling modes of the structure, which are the eigenfunctions. Each buckling mode is induced by a specific buckling load, which are the eigenvalues of the problem (Simitses & Hodges, 2005). The lowest buckling load, which leads to the first buckling mode is usually called the critical buckling load.

Chapter 3

Mechanical Properties - Specimen Experimental Tests

In this chapter, the experimental procedure will be explained in full detail, from specimen preparation to the final production of the test sample. Tensile and flexural tests of these specimens were performed based on ISO standards at the CIAFA's laboratory and at *Instituto Superior Técnico's* (IST) Mechanical Engineering Department, in Lisbon.

3.1 Preliminary Mass Calculations

To estimate the necessary resin, hardener and fiber mass quantities for the experimental part, initial calculations had to be performed based on theoretical equations from the laminates' rule of mixtures.

3.1.1 Specimen Data

After getting the specimens' sizes from Section 2.2.2, one can compute the necessary fiber, resin, and hardener mass to produce one specimen. It is still necessary to obtain both resin and hardener's density, which were given by each manufacturer, and also the carbon fiber mass density value.

Based on Gulgunje et al. (2015), common low density carbon fibers have their density vary between 1.75 - 1.93 $\times$ 10^3 kg/m^3. Adding that, Toray's T700G carbon fiber has a 1.80 $\times$ 10^3 kg/m^3 density (Toray Composite Materials America, 2018). This last value was used for the following calculations.

The epoxy resin and hardener densities are listed in Table 3.1. Recalling the designations given in Table 2.4, Resin 1 is the Sicomin SR8200 + SD 7206, and Resins 2 and 3 are the HexaMatrix without and with graphene, respectively. The fiber and matrix volume ratios were 60/40%. As for the matrix mixture between the resin and the corresponding hardener, both weight and volume ratios are also presented in the Table 3.1. Each composite density (ρ_c) was calculated using eq. (3.1). V corresponds to the volume ratio and ρ to the mass density of the matrix, resin, hardener, and fibers, denoted by the subscripts m, r, h, and f, respectively.

Table 3.1: Epoxy resins and hardener's densities and mixing ratios.

	Resin Density [kg/m^3]	Hardener Density [kg/m^3]	Mix Weight Ratio	Mix Volume Ratio
Resin 1	1175 $\pm$ 10	1040 $\pm$ 10	100 g Res. - 37 g Hard.	100 mL Res. - 42 mL Hard.
Resin 2	1158	942	100 g Res. - 22 g Hard.	100 mL Res. - 27 mL Hard.
Resin 3	1158	942	100 g Res. - 22 g Hard.	100 mL Res. - 27 mL Hard.

$$\rho_c = V_m \cdot (V_r \cdot \rho_r + V_h \cdot \rho_h) + V_f \cdot \rho_f \tag{3.1}$$

After calculating the composite density, the resin (W_r), hardener (W_h), and fiber (W_f) weight ratios were obtained through eqs. (3.2), (3.3), and (3.4), respectively.

$$W_r = \frac{V_r \cdot V_m \cdot \rho_r}{\rho_c} \tag{3.2}$$

$$W_h = \frac{V_h \cdot V_m \cdot \rho_h}{\rho_c} \tag{3.3}$$

$$W_f = \frac{V_f \cdot \rho_f}{\rho_c} \tag{3.4}$$

The composite specimen final mass (m_c) was calculated through eq. (3.5). Specimen size values were extracted from Tables 2.5 and 2.6.

$$m_c = L_3 \cdot b_1 \cdot h \cdot \rho_c \tag{3.5}$$

Last, through the mass of the composite and the corresponding weight ratios, one obtained the necessary resin (m_r), hardener (m_h), and fiber (m_f) mass to produce one specimen, with eqs. (3.6), (3.7), and (3.8).

$$m_r = m_c \cdot W_r \tag{3.6}$$

$$m_h = m_c \cdot W_h \tag{3.7}$$

$$m_f = m_c \cdot W_f \tag{3.8}$$

Bidirectional and unidirectional tensile specimen's results are presented in Tables 3.2 and 3.3.

Table 3.2: Composite density and weight ratios, and bidirectional tensile test specimens composition by mass.

	ρ_c [kg/m^3]	W_r	W_h	W_f	m_c [g]	m_r [g]	m_h [g]	m_f [g]
Resin 1	1534.0	0.22	0.08	0.70	19.18	4.22	1.53	13.43
Resin 2	1524.8	0.24	0.05	0.71	19.06	4.58	0.95	13.53
Resin 3	1524.8	0.24	0.05	0.71	19.06	4.58	0.95	13.53

Table 3.3: Unidirectional tensile test specimens composition by mass.

	$\mathbf{m}_c$ [g]	$\mathbf{m}_r$ [g]	$\mathbf{m}_h$ [g]	$\mathbf{m}_f$ [g]
Resin 1	5.75	1.26	0.46	4.03
Resin 2	5.72	1.37	0.29	4.06
Resin 3	5.72	1.37	0.29	4.06

Since both bending bidirectional and unidirectional specimens are the same size, both mass results are presented in Table 3.4.

Table 3.4: Bending test specimens composition by mass

	$\mathbf{m}_c$ [g]	$\mathbf{m}_r$ [g]	$\mathbf{m}_h$ [g]	$\mathbf{m}_f$ [g]
Resin 1	4.60	0.99	0.37	3.24
Resin 2	4.57	1.09	0.24	3.24
Resin 3	4.57	1.09	0.24	3.24

3.1.2 Panel Data

Taking into account what was last mentioned in Section 2.2.3, 10 specimens per test condition were planned to be built. The laminate panels' dimensions are presented in Table 3.5. The panel dimension choice took into consideration the minimum amount of wasted carbon fibers. The selected bidirectional carbon fiber mat is 1 m wide, and the unidirectional tape is 0.10 m wide. The glass fiber mat is the same size as its carbon fiber counterpart. The distance between each specimen is 10 mm, with a 25 mm margin on all sides.

Table 3.5: Laminates panels sizes.

	Bi. Tensile P.	**Uni. Tensile P.**	**Bi. Flexural P.**	**Uni. Flexural P.**	**Glass Fiber End Tab P.**
L_3 [mm]	300	290	150	140	290
b_1 [mm]	215	100	165	100	215
h [mm]	2	1	2	2	1

For each bidirectional test condition, two panels, containing five specimens each, were produced, while for the unidirectional case, due to the tape's width, three panels were manufactured bearing three specimens each.

The final masses of resin, hardener, and fibers for each panel are presented in Tables 3.6 and 3.7.

Table 3.6: Tensile test panels composition by mass.

	Bidirectional Panel				Unidirectional Panel			
	$\mathbf{m}_c$ [g]	$\mathbf{m}_r$ [g]	$\mathbf{m}_h$ [g]	$\mathbf{m}_f$ [g]	$\mathbf{m}_c$ [g]	$\mathbf{m}_r$ [g]	$\mathbf{m}_h$ [g]	$\mathbf{m}_f$ [g]
Resin 1	197.89	42.70	15.87	139.32	44.49	9.60	3.57	31.32
Resin 2	196.70	47.05	10.33	139.32	44.22	10.58	2.32	31.32
Resin 3	196.70	47.05	10.33	139.32	44.22	10.58	2.32	31.32

Table 3.7: Bending test panels composition by mass.

	Bidirectional Panel				Unidirectional Panel			
	$\mathbf{m}_c$ [g]	$\mathbf{m}_r$ [g]	$\mathbf{m}_h$ [g]	$\mathbf{m}_f$ [g]	$\mathbf{m}_c$ [g]	$\mathbf{m}_r$ [g]	$\mathbf{m}_h$ [g]	$\mathbf{m}_f$ [g]
Resin 1	75.93	16.38	6.09	53.46	42.95	9.27	3.44	30.24
Resin 2	75.48	18.05	3.97	53.46	42.69	10.21	2.24	30.24
Resin 3	75.48	18.05	3.97	53.46	42.69	10.21	2.24	30.24

The glass fiber (E-glass) density according to Wallenberger and Bingham (2010) is 2580 kg/m^3. Table 3.8 presents the glass fiber panel's mass. A total of ten panels were produced, all made with resin 1.

Table 3.8: Tensile test specimen's tab composition by mass.

	$\mathbf{m}_c$ [g]	$\mathbf{m}_r$ [g]	$\mathbf{m}_h$ [g]	$\mathbf{m}_f$ [g]
Resin 1	95.65	15.81	5.88	73.96

The final total masses of fibers and epoxy resin and hardener are presented in Table 3.9.

Table 3.9: Theoretical total fiber, resin, and hardener mass.

	Total fiber mass [g]
Bidirectional Fibers	1156.68
Unidirectional Fibers	554.04
Glass Fibers	739.56

	Total resin mass [g]	Total hardener mass [g]
Resin 1	332.89	123.75
Resin 2	192.57	42.30
Resin 3	192.57	42.30

During the production of the laminated panels, a matrix excess is necessary to compensate for its waste and to guarantee a good impregnation of the fibers. A CIAFA's experimental technique is to increase the mass of fiber by 10%. Then the obtained value will be multiplied by 1.5 to obtain the total matrix mass, leading to higher values of resin and hardener than the ones obtained before. Table 3.10 presents the preliminary resin and hardener masses for specimen production.

Table 3.10: Preliminary total fiber, resin, and hardener mass.

	Total matrix mass [g]	Total resin mass [g]	Total hardener mass [g]
Resin 1	2161.16	1577.49	583.67
Resin 2	940.90	771.23	169.67
Resin 3	940.90	771.23	169.67

3.2 Laminate Specimen Manufacturing Process

In this second section, specimen production will be thoroughly explained. This part will be divided into three main subsections. Firstly, material preparation will be performed based on initial data and numerical calculations. Secondly, the laminate manufacturing process by hand layup will take place, and thirdly, the panels will be cut and sanded according to specs.

3.2.1 Fibers and Matrix Preparation

ISO standards mentioned in Section 2.2.2 requires the specimens for both flexural and bidirectional tensile to be 2 mm thick and the unidirectional tensile specimen to be 1 mm thick. After performing some preliminary testing, it was determined that ten plies were necessary to get a 2 mm bidirectional carbon laminate. As for the unidirectional carbon laminate, eight and four plies were required for the construction of flexural and tensile panels, respectively. The glass fiber panels required ten plies in order for the end tabs to be at least 1 mm thick. After cutting the necessary fabric/tape, these were weighed before moving to the specimen production stage.

The required resin and hardener were calculated in accordance with the same theoretical expressions from Section 3.1. These were prepared and mixed in accordance with the suppliers' ratio specs. For resins 2 and 3 extra steps were required. Graphenest recommends some procedure steps to increase its efficiency:

1. Vigorously shake the hardener container for a minimum of 3 minutes;
2. Transfer the content of the hardener to a cup, then homogenize the mixture through a stirring process at 1000 rpm with ultrasound (40 kHz) for 1 hour;
3. Add resin to the cup in the appropriate amounts, and mix it using a stirrer at 280 rpm and ultrasound (40 kHz) for 5 minutes;
4. Place the mixture under vacuum for 5 minutes to remove air bubbles;
5. Apply the matrix to the sample piece to create the desired specimen.

Due to the lack of equipment available, some of the previously mentioned steps were skipped. Only steps 1, 4, and 5 were fully performed, while steps 2 and 3 were not totally completed, since CIAFA does not have an ultrasonic bath machine. As for the mechanical agitation, a cylindrical magnet (resembling a

magnetic stir bar) was used to stir the resin/hardener and matrix. This equipment could not measure the number of rotations per minute, however, we were able to assure a good mixing process on all prepared samples. In Figure 3.1 it is shown the used equipment, the magnetic stirrer on the left and the vacuum pump on the right.

(a) Magnetic stirrer.

(b) Vacuum pump.

Figure 3.1: Laboratory equipment.

3.2.2 Laminates Production

During the hand layup production method (explained in Section 2.2.1 and depicted in Figure 3.2), a peel ply the same size as the panel was laid under the first carbon/glass fiber ply. After the last carbon/glass fiber was applied another peel ply. The presence of the peel ply in the process increases the roughness of the panel's surface, enabling increased contact between the specimen's surface and the glass fiber end tabs. It also contributes to improve flexural results, by decreasing the probability of specimen slippage during tests.

At the end of the hand layup process, three extra layers were added to the specimens before closing the system to initiate the vacuum process. Two green absorbing cloths and, in between, a plastic sheet. The first applied green cloth will absorb the excess resin that escapes from the panel and the peel ply. The non-porous plastic sheet will help prevent resin from flowing out of the green cloth to the vacuum system. The top absorbing green cloth works as a breather ensuring that vacuum is applied to the entire component.

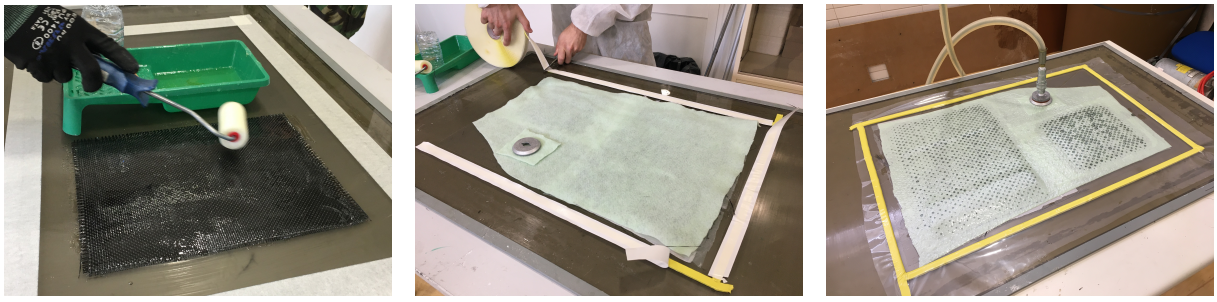

(a) Matrix application on a bidirectional carbon fabric.

(b) Vacuum bag ready to close.

(c) Vacuum bag closed.

Figure 3.2: Laminates production phases.

After sealing the vacuum bag, the vacuum hose is connected to the through-bag vacuum connector and the vacuum system is initiated. Trapped air and resin start being sucked through the pump, and

small wet spots start to show up on top of the green cloth revealing a good wettability of the carbon/glass matrix fibers (see Figure 3.2(c)). After this process, the initial curing stage takes place for the duration of 24h in a temperature-controlled room at 23 ℃ (this initial curing stage is similar across all resins).

At the end of this curing process, the vacuum bag is removed, and the post-curing process starts. Sicomin recommends for resin 1 to go through a post-cure cycle of 10 days at RT (23 ℃) in order to obtain the best mechanical properties. For resins 2 and 3, Graphenest recommends a post-cure cycle of 24 hours at a temperature of 40 ℃, which can only be obtained in a small oven. These post-curing conditions guarantee the best mechanical results according to the resin technical data sheet. Figure 3.3 shows the post-curing oven and a couple of finished bidirectional carbon flexural panels. Each panel was identified with the type of test (Tensile or Flexural), then the type of carbon fibers (BI for bidirectional and UNI for unidirectional), and finally a letter coding system to organize them.

(a) Post-curing oven.

(b) Finished bidirectional carbon flexural panels.

Figure 3.3: Post-curing oven and some finished panels.

3.2.3 Computer Numerical Control (CNC) Milling Machine

After the post-cure cycle, specimens can be cut out from the panels. To perform this step it was used a CNC machine specialized in milling (see Figure 3.4(a)). This automates the milling process, increasing the precision of the specimens cut. The CNC machine reads the coordinates information from the CAD files used to schematize the specimen's position in each panel, accompanied by further input data by the computer operator, and proceeds with the cutting of the samples according to the specifications presented in Table 3.11.

Table 3.11: CNC milling machine specifications.

End Mill Diameter	Pass Depth	Feed Rate	Spindle Speed
3.5 mm	0.5 mm	400 mm/min	1000 rpm

Before starting the milling process, each panel must be manually attached and secured to a table by screws. At the end, for safety reasons, each specimen must be sanded to prevent handling injuries from

splinters. The identification of each specimen was performed in a similar fashion as the panels, plus an additional number to identify the specimens in each panel (see Figure 3.4(b)).

Afterwards, end tabs were glued to the tips of tensile specimens. ISO/DIS 527-4 (2020a) mentions that they should be bonded with a high-stretch adhesive. Two possibilities arose to achieve this bonding, the first was to use Resin 1, and the second was to use a common epoxy glue (Araldite Standard) which is cheaper and easier to apply. Tensile preliminary tests were run to determine which of these performed better and the Araldite came on top achieving greater results during these tests. After applying the glue, spring clamps were used to apply pressure and thus guarantee a greater bonding between the elements (see Figure 3.4(c)). The curing of this resin was performed for 24h at RT, and after it was complete, the end tabs were sanded, to ensure alignment between them and the specimens.

(a) CNC milling machine.

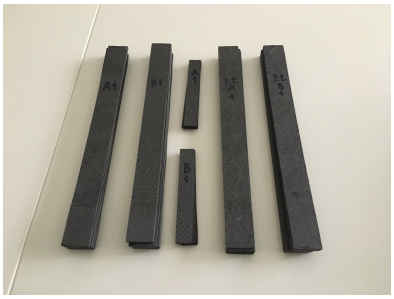

(b) Some specimens after being milled and sanded.

(c) Spring clamps.

Figure 3.4: Specimen's milling and end tabs attachment processes.

3.3 Testing and Results

This section explains the calculations that were run previous to the testing to obtain data that characterizes each specimen to be tested, such as their sizes and the experimental fiber/matrix volume ratios. It also explains the tests themselves and presents the obtained results.

3.3.1 Specimen Measurements

All data presented in this subsection was collected in order to calculate the specimen's fiber and matrix volume ratios. This was accomplished before bonding the end tabs to the tensile specimens. This data is fundamental to understand if the panels are being produced following the same relative quantities of matrix, while also enabling the discussion of variations in the test's results. First, each specimen was weighed in a Nahita-Blue series 5173 balance with a precision of $\pm$ 0.001 g (see Figure 3.5(a)).

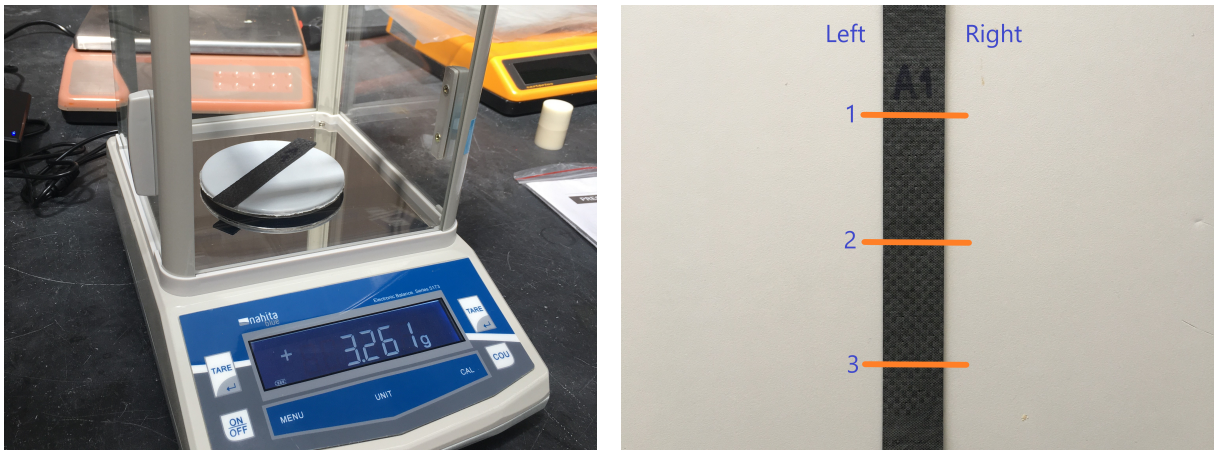

(a) Analytical balance weighing one specimen.

(b) Specimen's regions (1/2/3) and sides (Left/Right).

Figure 3.5: Specimens measurements.

Second, the specimens' length, width, and thickness were measured with a Mitutoyo series 500 digital caliper with a precision of $\pm$ 0.01 mm. Since tensile specimens were longer than 150 mm, their length had to be measured with a ruler with a precision of $\pm$ 0.5 mm. Each specimen's thickness was measured 6 times, once for each of the three regions and for both sides (see Figure 3.5(b)). The length was measured on each side and the width in each region.

Length, width, and thickness mean values were calculated and are presented in Table 3.12. From now on, the Bidirectional Tensile Panel - A will be used as an example throughout this section of the document. The mean values of length, width, and thickness were used to estimate the specimen cross-section area, surface area, and volume. Table 3.13 presents the obtained results.

Table 3.12: Bidirectional tensile panel - A: specimens' dimensions.

Specimen	Mean Thickness [mm]	Mean Width [mm]	Mean Length [mm]	Mass [g]
A1	1.86	24.98	249.5	15.947
A2	1.92	25.02	249.5	16.283
A3	1.98	24.96	249.5	16.581
A4	1.96	24.97	249.5	16.578
A5	1.92	25.26	249.5	16.447

Table 3.13: Bidirectional tensile panel - A: specimens' mean areas and volumes.

Specimen	Cross-Sec. Area [mm^2]	Surface Area [mm^2]	Volume [mm^3]
A1	46.55	6232.51	11613.24
A2	48.12	6248.75	12018.42
A3	49.39	6234.59	12334.10
A4	49.02	6236.26	12243.85
A5	48.46	6309.52	12103.76

To calculate the fiber-matrix volume ratio, it is necessary to calculate the fiber's mass. This can be estimated using the areal weight of the carbon fiber fabric and tape. A small sample of both carbon fibers was cut and weighed to calculate the respective areal weight. The results are presented in Table 3.14.

Table 3.14: Bidirectional fabric and unidirectional tape's areal weight.

	Bidirectional Carbon Fiber Fabric	**Unidirectional Carbon Fiber Tape**
Areal Weight [g/m^2]	160.1	227.6

The specimen fiber's mass was calculated from eq. (3.9).

$$m_f = Surface\ Area \times Areal\ Weight \times Number\ of\ Layers \tag{3.9}$$

By subtracting this from the specimen's mass, one gets the estimated matrix mass. Then, through eqs. (3.10) and (3.11) both fiber and matrix weight ratios can be respectively obtained.

$$W_f = \frac{m_f}{m_c} \times 100 \tag{3.10}$$

$$W_m = \frac{m_m}{m_c} \times 100 \tag{3.11}$$

Table 3.15 shows the obtained values for the example.

Table 3.15: Bidirectional tensile panel - A: fiber/matrix weight ratios.

Specimen	**No. Of Layers**	**Fiber Mass [g]**	**Matrix Mass [g]**	**Fiber Weight Ratio [%]**	**Matrix Weight Ratio [%]**
A1	10	9.978	5.969	62.6	37.4
A2	10	10.004	6.279	61.4	38.6
A3	10	9.982	6.599	60.2	39.8
A4	10	9.984	6.594	60.2	39.8
A5	10	10.102	6.346	61.4	38.6

Finally, the volume ratios can be calculated using the matrix density. To calculate this, the epoxy resin and the hardener's densities were recalled from Table 3.1. The matrix density (ρ_m) results from the resin and hardener density and it can be calculated with eq. (3.12).

$$\rho_m = V_r \cdot \rho_r + V_h \cdot \rho_h \tag{3.12}$$

The results obtained for the resins are presented in Table 3.16.

Table 3.16: Matrices' density.

	Matrix Density [kg/m^3]
Resin 1	1135
Resin 2	1112
Resin 3	1112

Using the matrix density, the matrix volume (v_m) was calculated from eq. (3.13).

$$v_m = \frac{m_m}{\rho_m} \tag{3.13}$$

Assuming that the specimen is comprised of matrix and fiber, the matrix volume ratio (V_m) is given by eq. (3.14), where v_c is the composite specimen volume.

$$V_m = \frac{v_m}{v_c} \times 100 \tag{3.14}$$

Results for panel A are presented in Table 3.17.

Table 3.17: Bidirectional tensile panel - A: fiber/matrix volume ratios.

Specimen	Matrix Volume [mm^3]	Fiber Volume Ratio [%]	Matrix Volume Ratio [%]
A1	5258.49	54.7	45.3
A2	5531.60	54.0	46.0
A3	5814.10	52.9	47.1
A4	5809.11	52.6	47.4
A5	5590.37	53.8	46.2

3.3.2 Mechanical Testing

3.3.2.1 Tensile Testing

Tensile tests were run on the CIAFA's MTS Systems model 810 tensile testing machine with a 100 kN load cell. The test was configured and executed using the software TestWorks 4. Figure 3.6 shows the CIAFA's mechanical testing laboratory and its testing equipment.

Figure 3.6: Tensile testing machine and its computers.

Specimen's end tabs were placed in the machine clamps using a square to make sure the specimen is perpendicular to the clamps. The tensile test is run at a strain rate of 2 mm/min. With the specimen's length, width, and thickness as input data, the software outputs the Young's modulus, maximum stress, and strain at break, for each specimen.

It is worth mentioning that all bidirectional specimens broke in the center region (see Figure 3.7(a)). However, some also broke at the top and/or bottom, near the end tabs (see Figure 3.7(b)). This was due to the specimen's stress decompression after the first breakage. As for the unidirectional specimens, because transversal fibers are being connected with very thin glass fiber, these had a more aggressive breaking. Some of them totally shattered across a region (see Figure 3.7(c)). Others had groups of fibers breaking in different regions (see Figure 3.7(d)).

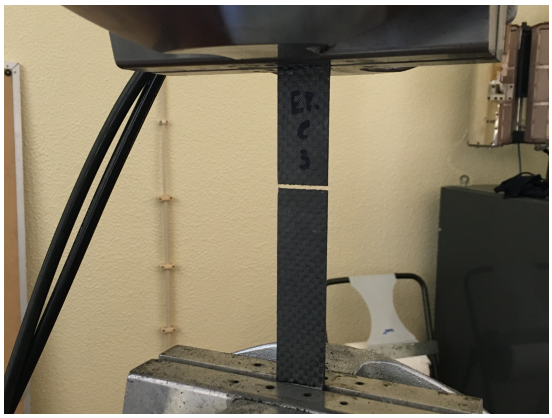

(a) Bidirectional specimen breaking at the center.

(b) Bidirectional specimen breaking in three different points.

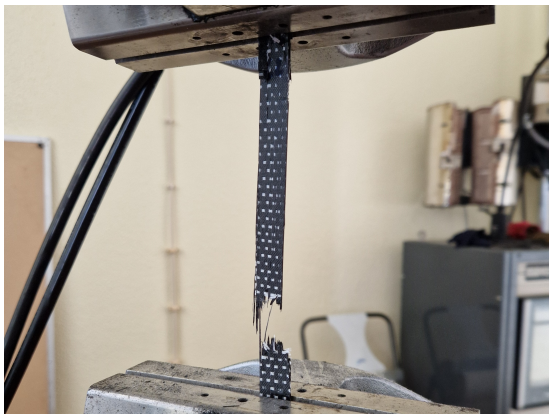

(c) Unidirectional specimen totally breaking.

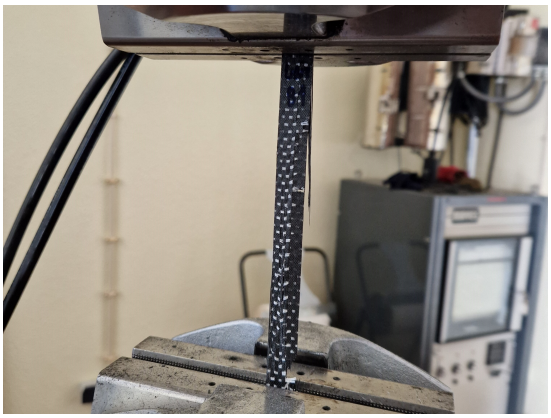

(d) Unidirectional specimen partially breaking.

Figure 3.7: Tensile specimens after being tested.

3.3.2.2 Flexural Testing

For flexural testing, it was estimated that a point load of magnitude of approximately 400 N was sufficient to break the specimen. Since the MTS 810 at CIAFA's facilities is equipped with a 100 kN load cell, sensitivity would have been very low, leading to an increased difficulty to obtain precise stress and strain values at break. Therefore, the flexural testing was performed at the IST's Mechanical Engineering

Department, in Lisbon, using an Instron model 5566 testing equipment with a 500N load cell.

For the three-point flexural test (see Figure 3.8), a rate of displacement of 5 mm/min was set and the displacement and the applied force were obtained with a sampling frequency of 50Hz. After which, each specimen's stress and strain values were calculated by the user, and the stress/strain curve was obtained.

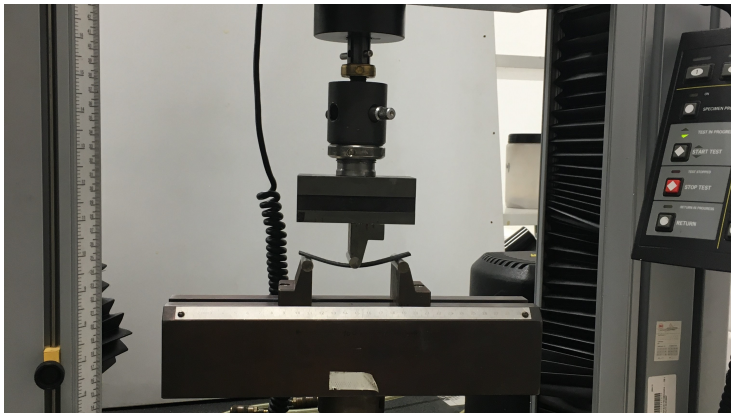

Figure 3.8: Three-point flexural testing machine.

In resemblance to the tensile test, the bidirectional specimens also broke at the center (see Figure 3.9(a)). As for the unidirectional, almost none had completely been broken into two pieces. The majority only broke several outer plies (see Figure 3.9(b)).

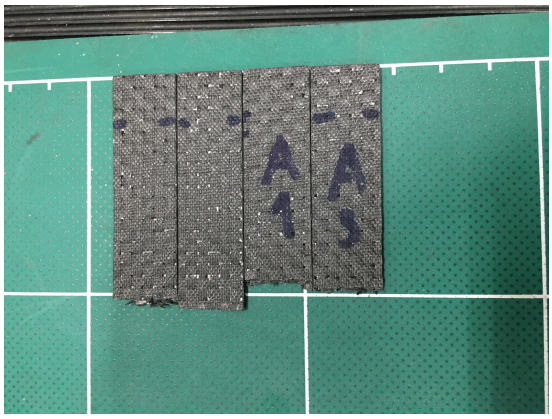

(a) Bidirectional specimens breaking at the center.

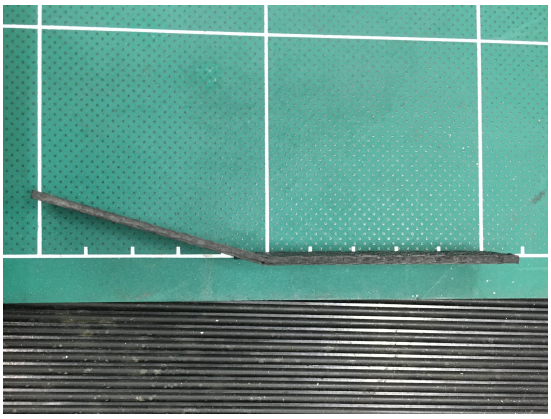

(b) Unidirectional specimen breaking several plies.

Figure 3.9: Flexural specimens after being tested.

3.3.3 Obtained Results

During the production and testing phases, several issues occurred: some panels had a low matrix volume ratio; the CNC milling machine cut some specimens out of the determined limits; and also, one end tab slipped out during the tensile test. All of these issues led to outliers. In order to eliminate undetected problems, an interquartile range method was applied to the mechanical properties, and to the obtained stress and strain values.

This interquartile range method seeks to calculate lower and upper boundaries for the specimens' results. Final properties were calculated for the different types of carbon fibers used, which means different panels were grouped to obtain their mean values. This way, for a total of nine to ten results, depending on the kind of test (flexural or tensile), the first (Q_1) and third (Q_3) quartiles were obtained. Then the interquartile range (IQR), which is the difference between these two values, was calculated. Afterwards, the lower ($LBound$) and upper ($UBound$) boundaries were also calculated through eqs. (3.15) and (3.16).

$$LBound = Q_1 - 1.5 \cdot IQR \qquad (3.15) \qquad\qquad UBound = Q_3 + 1.5 \cdot IQR \qquad (3.16)$$

As an example, in this subsection are presented only the results for panels A and B, which were both manufactured with bidirectional carbon fiber and resin 1. Table 3.18 presents the Young's modulus, peak load, and peak stress for panel A and B specimens. The lower and upper bounds for each parameter can be found in Table 3.19.

Table 3.18: Bidirectional tensile panels - A and B: obtained results.

Specimen	E [GPa]	Peak Load [N]	Peak Stress [MPa]	Strain At Break [%]
A1	41.519*	31634.56	679.65	1.69
A2	39.570	32115.56	668.46	1.75
A3	38.649	26588.16	538.39*	1.48
A4	38.726	27594.56	562.88	1.51
A5	38.733	33199.30	685.05	1.86
B1	39.277	33578.70	696.43	1.88
B2	39.732	32661.07	699.52	1.89
B3	38.654	29685.39	622.70	1.69
B4	37.708	33488.91	697.97	1.98
B5	37.808	32728.29	678.26	1.92

* Values out of the Lower/Upper boundaries range (outliers)

Table 3.19: Bidirectional tensile panels - A and B: interquartile range outlier method.

	E [GPa]	Peak Load [N]	Peak Stress [MPa]	Strain Break [%]
Q_1	38.650	30172.68	634.14	1.69
Q_3	39.497	33081.55	693.59	1.89
IQR	0.846	2908.86	59.45	0.20
$LBound$	37.381	25809.39	544.97	1.40
$UBound$	40.767	37444.84	782.76	2.18

3.3.3.1 Tensile Results

Mean values from each group of tests were extracted for comparison with the final results. The following tables present the necessary data for the numerical part of this thesis where the final mean value, the standard deviation (S.D.), and the 95% confidence interval are presented. It is worth mentioning that both the standard deviation and the confidence interval are recommended by standards ISO 527-1 (2019) and ISO 14125:1998 + AC:2002 + A1:2011 (2011), in order to be 95% confident that the true mean is within the last value range. Tables 3.20 and 3.21 present the bidirectional and unidirectional carbon fiber specimen tensile results for resin 1-3 respectively.

Table 3.20: Bidirectional carbon fiber specimen tensile results.

		Thickness [mm]	Fiber Volume Ratio [%]	Matrix Volume Ratio [%]	E [GPa]	Peak Stress [MPa]
Resin 1	**Final Mean Value**	1.91	53.6	46.4	38.776	663.91
	Final S.D.	0.03	0.6	0.6	0.698	44.81
	95% Confid. Int.	-	-	-	0.483	31.05
Resin 2	**Final Mean Value**	1.88	54.8	45.2	38.745	657.41
	Final S.D.	0.05	1.9	1.9	1.189	49.97
	95% Confid. Int.	-	-	-	0.777	32.64
Resin 3	**Final Mean Value**	1.85	56.5	43.5	38.506	663.96
	Final S.D.	0.03	1.4	1.4	0.252	20.75
	95% Confid. Int.	-	-	-	0.175	14.38

Table 3.21: Unidirectional carbon fiber specimen tensile results.

		Thickness [mm]	Fiber Volume Ratio [%]	Matrix Volume Ratio [%]	E [GPa]	Peak Stress [MPa]
Resin 1	**Final Mean Value**	0.98	63.1	36.9	83.664	1621.46
	Final S.D.	0.01	0.6	0.6	1.899	68.81
	95% Confid. Int.	-	-	-	1.316	47.68
Resin 2	**Final Mean Value**	0.96	67.7	32.3	82.204	1386.08
	Final S.D.	0.01	1.0	1.0	2.069	53.68
	95% Confid. Int.	-	-	-	1.813	47.05
Resin 3	**Final Mean Value**	0.98	66.2	33.8	82.227	1341.88
	Final S.D.	0.02	1.6	1.6	1.627	97.33
	95% Confid. Int.	-	-	-	1.127	67.44

3.3.3.2 Flexural Results

The same method was applied to the flexural results. The flexural modulus (E_f) was obtained by eq. (2.7), with the deflections for strains $\varepsilon_f = 0.0005$ and $\varepsilon_f = 0.0025$, and their corresponding applied force. Tables 3.22 and 3.23 present the bidirectional and unidirectional carbon fiber specimen flexural results for the three resins, respectively.

Table 3.22: Bidirectional carbon fiber specimen flexural results.

		Thickness [mm]	Fiber Volume Ratio [%]	Matrix Volume Ratio [%]	E [GPa]	Peak Stress [MPa]
Resin 1	**Final Mean Value**	1.78	57.6	42.4	35.887	664.82
	Final S.D.	0.04	1.5	1.5	2.543	22.82
	95% Confid. Int.	-	-	-	1.576	14.14
Resin 2	**Final Mean Value**	1.81	55.9	44.1	36.918	661.54
	Final S.D.	0.02	1.2	1.2	1.114	35.01
	95% Confid. Int.	-	-	-	0.690	21.70
Resin 3	**Final Mean Value**	1.83	56.1	43.9	38.124	645.36
	Final S.D.	0.03	1.3	1.3	1.962	27.94
	95% Confid. Int.	-	-	-	1.216	17.32

Table 3.23: Unidirectional carbon fiber specimen flexural results.

		Thickness [mm]	Fiber Volume Ratio [%]	Matrix Volume Ratio [%]	E [GPa]	Peak Stress [MPa]
Resin 1	**Final Mean Value**	1.96	57.2	42.8	87.430	926.54
	Final S.D.	0.03	1.5	1.5	5.647	75.85
	95% Confid. Int.	-	-	-	3.690	49.56
Resin 2	**Final Mean Value**	1.75	67.7	32.3	49.677	684.65
	Final S.D.	0.06	2.3	2.3	7.934	41.56
	95% Confid. Int.	-	-	-	5.183	27.15
Resin 3	**Final Mean Value**	1.94	59.7	40.3	73.394	820.28
	Final S.D.	0.02	0.9	0.9	7.566	53.74
	95% Confid. Int.	-	-	-	6.054	43.00

3.4 Analysis and Discussion

In this last section, the results attained from the tensile and flexural tests will be analysed and scrutinised. The end values from this analysis will be used in the upcoming numerical chapter.

3.4.1 Tensile Test Analysis

The obtained tensile results were precise, with low S.D. values. These values were between 2% to 3% of the Young's modulus. The highest difference between bidirectional moduli was around 270 MPa, and resin 1 presented the highest stiffness value, while resin 3 presented the lowest stiffness value. For the unidirectional moduli, the difference was approximately 1460 MPa, and resin 1 also presented the highest stiffness value, while resin 2 presented, in this case, the lowest stiffness value.

It is worth mentioning that during tensile tests, some issues were detected:

- One specimen from the unidirectional resin's 1 third panel had its tabs slipping during the test;
- During the milling phase, four unidirectional resin's 2 specimens had a narrow cut;
- These and other specimens that were out of boundary limits were considered outliers and did not count for the mean values presented in the previews section. A total of 11 outliers out of the original 57 specimens were excluded.

3.4.2 Flexural Test Analysis

Comparing the obtained results from the unidirectional and the bidirectional flexural modulus, the bidirectional were more precise, with a lower S.D. value. The flexural modulus standard deviations from the bidirectional were between 3% to 7%. Still, the unidirectional resin 1 value was more accurate (6.46%) then compared to the values from resins 2 (15.97%) and resin 3 (10.30%). Comparing the tensile and the flexural tests, S.D. values were lower on the first one.

As for the difference between flexural moduli, in the bidirectional carbon specimens, resin 3 presented the highest stiffness, while resin 1 presented the lowest stiffness. For the bidirectional moduli, the difference was approximately 2237.50 MPa. For unidirectional carbon, the difference was higher due to some specimen production problems.

For the flexural test, a total of 12 specimens out of 57, including the unidirectional resin 2, were considered outliers due to several issues:

- Bidirectional resin 1 batches were too thin. Most specimens were under the 1.8 mm thickness limit. Still, that difference was lower than 1% and the standard deviation was also low, so there were no outliers.
- For resin 2 and resin 3, thickness values were also low, but they did not cross the 1.8 mm lower bound limit.
- The unidirectional resin 3 had its third panel being produced with a very low matrix volume ratio, around 33%, as opposed to the other two panels which were 40.28%. This led to these three specimens' thicknesses crossing below the 1.8 mm limit. This third panel was considered an outlier.

- Panel production from resin 2 also presented the same problem. This time, the three panels were produced with a very low matrix volume ratio, leading to thin specimens that crossed the lower bound of 1.8 mm, leading to the complete disregard of the resin 2 unidirectional results.

3.4.3 Discussion and Final Results

In general, both tensile and flexural results were performed with no major issues apart from the flexural unidirectional resin 2 and 3. Unidirectional panels should have had more resin, in order to increase their matrix volume ratio. For flexural bidirectional panels, the number of plies should have been increased to 12 so that they could surpass the 1.8 mm lower bound limit.

Although the tested population was small, there is a relation between the matrix volume ratio and the Young's/flexural modulus. By comparing the three resins in each test, one can infer that the increase in the matrix volume ratio leads to an increased Young's modulus. The only exception for this correlation was for bidirectional flexural resins 2 and 3. Despite both matrix volume ratios' similarity, resin 3 had a lower matrix volume ratio than resin 2, but its thickness was higher, consequently, the flexural modulus was also higher.

Comparing tensile and flexural elastic modulus, unidirectional resin 1, in which flexural specimens had a higher matrix volume ratio (42.8%) compared with the tensile (36.9%), both Young's moduli were high. Still, there was a considerable difference of 4.5% between them, having the flexural one been the highest. This shows that the effect of a high matrix volume ratio is more preponderant on the flexural tests, especially in the unidirectional laminates, due to the interlaminar shear stress effect that leads to the specimen's failure. For the flexural test, stress distribution varies through the laminate thickness, while it is constant for the tensile test. Figure 3.10(a) shows maximum tensile stress along the specimen thickness, while Figure 3.10(b) shows maximum compressive stress at the top and maximum tensile stress at the bottom of the specimen. As for the fiber/matrix volume ratio limit value to obtain the highest Young's/flexural modulus, there is not enough data to infer any conclusions.

(a) Tensile stress.

(b) Flexural stress.

Figure 3.10: Stress distribution through laminate thickness.

According to the classical laminate theory, since the specimen's stacking is equal for each test specimen and all the plies are oriented at zero degrees, the Young's modulus should be the same as the flexural modulus. This statement is independent of the number of plies stacked. Table 3.24 show the

modulus differences between Young's and flexural modulus results for bidirectional and unidirectional carbon fibers. The differences between the same modulus for different resins are shown in the last three columns of each table. Eq. (3.17) explains how to calculate those differences. Table 3.25 presents the same comparison for the peak stresses from both tests for both carbon fibers.

$$Difference\,[\%] = \frac{Second\,Value - First\,Value}{First\,Value} \times 100 \tag{3.17}$$

Table 3.24: Differences between Young's and flexural modulus results for bidirectional and unidirectional carbon fibers.

					Resins Differences [%]		
		Resin 1	**Resin 2**	**Resin 3**	**1 vs 2**	**2 vs 3**	**1 vs 3**
Bidirectional Carbon Fibers	**Young's Modulus [GPa]**	38.776	38.745	38.506	-0.1	-0.6	-0.7
	Flexural Modulus [GPa]	35.887	36.918	38.124	2.9	3.3	6.2
	Modulus Difference [%]	-7.4	-4.7	-1.0	-	-	-
Unidirectional Carbon Fibers	**Young's Modulus [GPa]**	83.664	82.204	82.227	-1.7	0.0	-1.7
	Flexural Modulus [GPa]	87.430	49.677	73.394	-43.2	47.7	-16.0
	Modulus Difference [%]	4.5	-39.6	-10.7	-	-	-

Table 3.25: Differences between peak stresses results from tensile and flexural tests for bidirectional and unidirectional carbon fibers.

					Resins Differences [%]		
		Resin 1	**Resin 2**	**Resin 3**	**1 vs 2**	**2 vs 3**	**1 vs 3**
Bidirectional Carbon Fibers	**Tensile Peak Stress [MPa]**	663.91	657.41	663.96	-1.0	-1.0	0.0
	Flexural Peak Stress [MPa]	664.82	661.54	645.36	-0.5	-2.4	-2.9
	Peak Stress Difference [%]	0.1	0.6	-2.8	-	-	-
Unidirectional Carbon Fibers	**Tensile Peak Stress [MPa]**	1621.46	1386.08	1341.88	-14.5	-3.2	-17.2
	Flexural Peak Stress [MPa]	926.54	684.65	820.28	-26.1	19.8	-11.5
	Peak Stress Difference [%]	-42.8	-50.6	-38.9	-	-	-

For the following part of this thesis, the numerical software requires the elastic modulus from each material to be considered as the Young's modulus. Since the test case was a wing structure, the loads applied to these structures are mainly of the flexural type. As such, flexural test loads were used as they were the ones that most closely matches the aerodynamic loads, and the flexural modulus was the one to be considered in the numerical part.

With this decision, two problems arose. The first was the fact that unidirectional resin 2 test results were discarded. The second is that the results from the unidirectional resin 3 were compromised due to the low matrix volume ratio. This rendered the flexural modulus value almost 11% lower than the corresponding tensile value, as opposed to the 4.50% increase that was observed in resin 1. The

expected tendency for the unidirectional values for the three resins, if they had approximately the same matrix volume ratio, was to increase along the three resins, just as it happened with bidirectional fibers. An estimation for flexural modulus, thickness, and peak stress was performed for resins 2 and 3 (resin X), following eq. (3.18). This way, unidirectional flexural modulus resins difference values from Table 3.24 will now be the same as the bidirectional ones. The same occured for the peak stress and the percentage differences from Table 3.25. Due to time constrictions, more tests could not be performed on these materials in order to increase available data and results accuracy.

$$Estimated\,Value\;for\;Resin\;X = \frac{Bidirectional\;Resin\;X}{Bidirectional\;Resin\;1} \times Unidirectional\;Resin\;1 \tag{3.18}$$

Table 3.26 shows the final results for each resin. The materials' mass density accounts for the fiber/matrix volume ratios, and are not the initial calculated theoretical values. The mass density of the estimated material is the same as the respective bidirectional carbon fibers laminate. In the table's two last lines, the ultimate tensile strength is the peak stress value obtained on the tests. Despite originally being an ultimate flexural strength, flexural peak stresses were lower or almost the same as tensile peak stresses. This makes way for a more conservative approach in the structural analysis. Subscripts 1 and 2, in the mechanical properties, represent the specimen's longitudinal and transversal directions, respectively.

Table 3.26: Final geometric and mechanical material properties to be used in the numerical solution.

		Resin 1		Resin 2		Resin 3	
		Bidirectional	**Unidirectional**	**Bidirectional**	**Unidirectional**	**Bidirectional**	**Unidirectional**
Ply Thickness [mm]		0.178	0.246	0.181	0.250*	0.183	0.252*
Mass Density [kg/m^3]		1518.7	1515.5	1492.1	1492.1	1493.5	1493.5
Area Density [g/m^2]		270.79	372.37	270.66	372.87	272.72	375.77
Young's Modulus [GPa]	**E_1**	35.887	87.430	36.918	89.943*	38.124	92.881*
	E_2	35.887	-	36.918	-	38.124	-
Ult. Tens. Streng. [MPa]	**UT_1**	664.82	926.54	661.54	921.98*	645.36	899.43*
	UT_2	664.82	-	661.54	-	645.36	-

* Estimated values using eq. (3.18)

For comparison purposes, the area density was calculated for each one of the materials. It is possible to check that a bidirectional carbon fiber panel is significantly lighter than a unidirectional one, due to the great thickness differences. Also, unidirectional resin 1 laminates are a little lighter than resin 2, and the opposite occurs for bidirectional. As for the graphene-based resin 3, the same-size panels were a bit heavier. For aircraft structure's design, weight is one of the most significant pillars of the project phase. It must be reduced to a minimum while guaranteeing the necessary stiffness of the structure.

Chapter 4

UAV Wing Design

This chapter addresses the design of a UAV wing using the materials characterized in the previous chapter. The main objective is to compare the materials' application and find out the benefits of including graphene in the matrix for aeronautical structures. To that end the wing structure obtained by Sá (2021) is used as baseline for the preliminary design of an electric vertical take-off and landing (eVTOL) Class I UAV. The wing is designed to meet airworthiness specifications, and it is used linear static and linear buckling analyses.

4.1 Baseline Design

4.1.1 Conceptual Design Specifications

The wing baseline design that will be analysed is the main wing of the conceptual design of an eVTOL Class I UAV (Alves et al., 2021), represented in Figure 4.1. The UAV conceptual design resulted in a fixed-wing with an inverted V-tail configuration with a maximum take-off weight of 21.7 kg. For take-off and landing, four propeller electric engines are installed in two booms which connect the wing to the V-tail. An additional propeller electric engine is installed at the fuselage back end for fixed-wing flight. The UAV power source is a hydrogen fuel cell. Sá (2021) has done the preliminary design of the main wing for this UAV, which is used as the baseline design to study the impact of including graphene in the composite matrix for aeronautical structures. Baseline design specifications are presented in Table 4.1.

Figure 4.1: UAV conceptual design CAD model. Retrieved from Alves et al. (2021).

Table 4.1: Wing baseline design specifications. Retrieved from Sá (2021).

Specification	**Value**
Wingspan	4.00 m
Rectangular section wingspan	1.50 m
Chord at the root of the wing	0.399 m
Chord at the tip of the wing	0.220 m
Wingtip horizontal offset	0.040 m
Wingtip vertical offset	0.008 m
Wing's aspect ratio	12.0

The baseline design was obtained for the following flight envelope (Sá, 2021):

- Positive limit load factor: 4;
- Negative limit load factor: -1.34;
- Ultimate load factor, which is obtained a safety factor of 1.5, as defined in STANAG 4703 (2014): 6.

Sá also considered gust load factors, but it was concluded that gusts do not affect the UAV flight envelope. Therefore, it is not necessary to include gust load factors in the wing design.

Since the wing is designed with composite materials, is necessary to include a safety factor on the material properties to account for uncertainties related to the manufacturing process and material properties characterization. According to Hollmann (2003), laminate's ultimate tensile strength must be divided by 2, if mechanical properties were obtained at room temperature. Otherwise, if the test temperature was the same as for flight conditions, the safety factor should be 1.5.

The baseline wing was designed with the known properties from the materials used in CIAFA, which were studied by Silva (2017). It was designed considering:

- Bidirectional carbon fibers: plain weave fabric, 3K, High Strength, 160 g/m^2;
- Unidirectional carbon fibers: 15 cm tape, 3K, High Strength, 215 g/m^2;
- Epoxy resin: Sicomin SR 1500 + Hardener: SD 2505 (100 g Epoxy - 33 g Hardener);
- Foam core: Airex C70.75, thickness 3 mm (isotropic material).

Table 4.2 shows the properties used by Sá (2021) in the preliminary wing design. Ultimate tensile strength already takes into account the safety factor above mentioned. Comparing with Table 3.26, it is possible to observe that the material used by Sá had the following differences:

- Higher: bidirectional ply thickness, Young's modulus;
- Lower: unidirectional ply thickness, mass density, ultimate tensile strength;

Table 4.2: Geometric and mechanical material properties retrieved from Sá (2021) for comparison.

	Bi-Carbon + Epoxy	Uni-Carbon + Epoxy	Airex + Epoxy
Ply Thickness [mm]	0.190	0.222	3.00
Mass Density [kg/m^3]	1300.0	1450.0	422
E_1 [GPa]	44.793	95.070	0.066
E_2 [GPa]	53.193	9.173	0.066
UT_1 [MPa]	225.00	442.30	1.00
UT_2 [MPa]	225.00	-	1.00

4.1.2 Baseline Wing Model and Structural Analysis Results

Figure 4.2 shows the CAD rendered image of the wing's baseline model design.

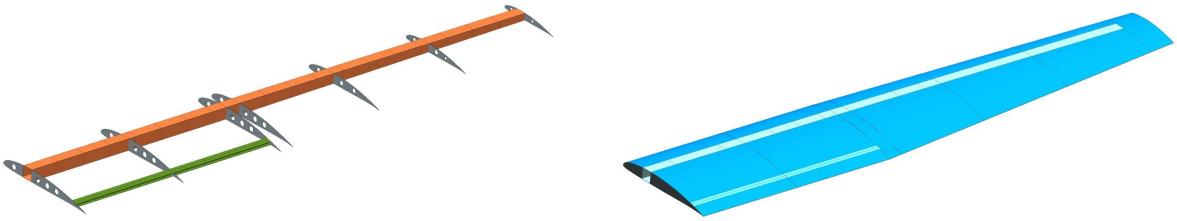

(a) Internal structure. (b) External structure.

Figure 4.2: Wing's CAD model. Retrieved from Sá (2021).

The main spar has a rectangular cross-section with the dimensions presented in Table 4.3.

Table 4.3: Baseline spar dimensions. Adapted from Sá (2021).

Width	40 mm
Root Height	38 mm
Tip Height	20 mm
Span	1900 mm

To define the spar laminate, the spar's caps and webs were divided into nineteen 100 mm long sections. The spar design achieved by Sá (2021) is presented in Table 4.4. The base value represents the number of plies, and the exponent the number of sections having that number of plies. The summation of all exponents will be 19, the number of sections in the spar. Caps were composed of unidirectional carbon fibers composite aligned with the span direction. Webs were composed of bidirectional carbon fibers at a 45º arrangement, where 0º is the span-wise direction. This will be the starting point for Section 4.2.

Table 4.4: Baseline spar laminate distribution. Adapted from Sá (2021).

Top Cap	Lower Cap	Webs
5^1 / 4^3 / 3^3 / 2^4 / 1^8	5^1 / 4^2 / 3^3 / 2^4 / 1^9	2^5 / 1^{14}

Sá (2021) applied a distributed load along the spar's caps equal to the wing load for the ultimate load factor considered. The first 1400 mm had a load of 527.7 N equally distributed by all mesh elements. For the last 500 mm, the load was 113.04 N. Figure 4.3 presents the main spar's applied loads distribution. The value was calculated in his conceptual phase of the project. The obtained static analysis results for the spar's model are presented in Table 4.5. Last column presents the displacements percentage relative to the total wingspan size of 2000 mm.

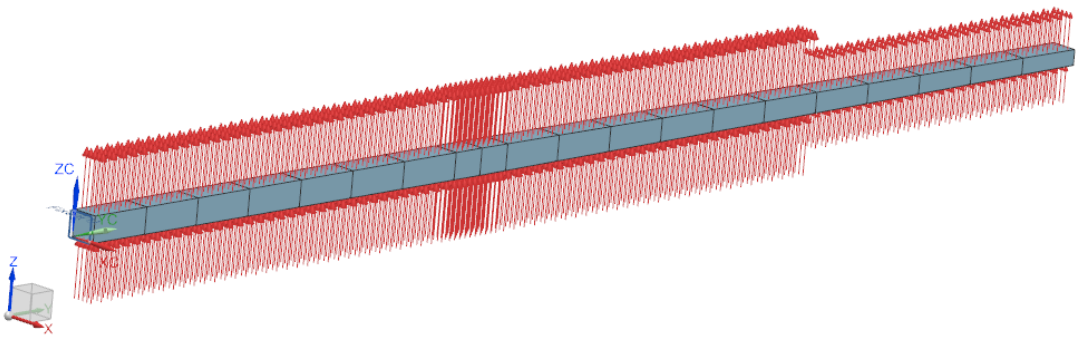

Figure 4.3: Baseline main spar applied loads distribution.

Table 4.5: Baseline main spar maximum stress and displacement. Adapted from Sá (2021).

Maximum Stress	Maximum Displacement	Wingspan %
423.39 MPa	259.0 mm	12.95%

Concerning the wing, the main spar is at 33.5% of the wing's chord, where the airfoil thickness is maximum. The secondary spar is at 85% of the chord and it has a 750 mm length, which corresponds to the rectangular part of the wing. Instead of a rectangular cross-section shape, it has an I shape, with a 20 mm cap width. The caps are composed of a unidirectional carbon fiber composite, with a laminate of two plies aligned with the span direction. The web is composed of a sandwich panel made of two bidirectional plies at a 45º arrangement with a core of 3 mm Airex C70.75 foam.

A total of seven ribs give the airfoil shape to the wing. Table 4.6 shows their position, considering the distance from the root of the wing, the number of holes, and their diameter. Ribs 1 to 4 are composed of four bidirectional plies at a 45º arrangement with the chord-wise direction, and one unidirectional in the middle, perpendicular to the chord-wise. Ribs 5 to 7 have two bidirectional plies and one unidirectional

in between, with the same respective alignment directions as the ribs previously mentioned. The wing tip has the same stacking. Finally, the skin is composed of two bidirectional plies at a 45º arrangement, where 0º is the span-wise direction.

Table 4.6: Baseline wing ribs position. Adapted from Sá (2021).

Rib	Distance From the Root [mm]	Number of Holes	Holes' Diameter [mm]
1	0	4	18
2	375	4	18
3	750	4	18
4	800	4	18
5	1165	3	15
6	1530	3	14 / 15 / 10
7	1900	2	11 / 10

A pressure load, equivalent to the aerodynamic load corresponding to the ultimate load factor, was applied to the wing skin. The static analysis results obtained are shown in Table 4.7. All stress results are Von-Mises stresses.

Table 4.7: Baseline wing maximum stresses and displacement. Adapted from Sá (2021).

Maximum Bi-Carbon Stress	Maximum Uni-Carbon Stress	Maximum Displacement	Wingspan %
217.41 MPa	421.70 MPa	168.3 mm	8.4%

4.2 Main Spar Design

In this section, the object of study is the main spar. Its laminate configuration will be determined to withstand the static load represented in Figure 4.3 and buckling phenomena. The laminate is defined for resin 1 and the results for the other two resins are extracted after. In order to apply the failure theory explained in Section 2.3.2, the worst principal stresses are used. These are the tensile or compressive highest values obtained in simulations for each element's principal direction. They can either be positive or negative.

4.2.1 FEM Input Data

The finite element analysis software requires the following material properties, in order to characterize an orthotropic material:

- Mass density;
- Young's modulus in all three directions;

- Poisson's ratio in all three directions;
- Shear modulus in all three directions.

In Chapter 3, it was obtained the Young's modulus and ultimate strength of the 3 resins considered in the study. Therefore, it was necessary to use standard values for carbon fiber composites to fill in the materials' properties required by the software. The properties list was completed with data retrieved from the study done by Silva (2017), where he combined experimental tests with a bibliography review to create a data set for bi and unidirectional carbon fiber composites. Table 4.8 presents the materials' properties used in the wing design.

Table 4.8: Material properties data set used in FEM analysis.

	Resin 1		**Resin 2**		**Resin 3**		
	Bi-Carbon	**Uni-Carbon**	**Bi-Carbon**	**Uni-Carbon**	**Bi-Carbon**	**Uni-Carbon**	**Airex + Epoxy**
Ply Thickness [mm]	0.178	0.246	0.181	0.250	0.183	0.252	3.000*
Mass Density [kg/m^3]	1518.7	1515.5	1492.1	1492.1	1493.5	1493.5	422.0*
E_1 [GPa]	35.887	87.430	36.918	89.943	38.124	92.881	0.066*
E_2 [GPa]	35.887	9.173*	36.918	9.173*	38.124	9.173*	0.066*
E_3 [GPa]	9.173*	9.173*	9.173*	9.173*	9.173*	9.173*	0.066*
ν_{12}	0.060*	0.262*	0.060*	0.262*	0.060*	0.262*	0.300*
ν_{13}	0.388*	0.262*	0.388*	0.262*	0.388*	0.262*	0.300*
ν_{23}	0.388*	0.396*	0.388*	0.396*	0.388*	0.396*	0.300*
G_{12} [GPa]	5.000*	5.000*	5.000*	5.000*	5.000*	5.000*	0.030*
G_{13} [GPa]	2.889*	5.000*	2.889*	5.000*	2.889*	5.000*	0.030*
G_{23} [GPa]	2.889*	3.470*	2.889*	3.470*	2.889*	3.470*	0.030*
UT_1 [MPa]	332.41	463.27	330.77	460.99	322.68	449.72	1.00*
UT_2 [MPa]	332.41	-	330.77	-	322.68	-	1.00*

* Values retrieved from Silva (2017)

The foam plus the epoxy is considered an isotropic material. The obtained values by Silva show equal values for the three directions. Still, these values do not verify the isotropic relation shown in eq. (2.18). Airex sandwich will be inserted in the software as an orthotropic material, to avoid any problems during computation.

Last, 2D Mapped Mesh from Siemens NX will be applied and will generate CQUAD4 elements, which are 4-node elements. This tool allows a few 3-node elements to improve the mesh, so CTRIA3 elements will be present too. For the spar analysis, Sá used elements with a 1 mm length, and for the wing analysis, elements with a 4 mm length, after performing a convergence analysis.

4.2.2 Linear Static Analysis

For a matter of simplicity, the following coordinate system will be considered for analysis purposes: the x-axis corresponds to the chord-wise direction, starting at the root leading edge; the y-axis is the span-wise direction, starting at the wing root; the z-axis is perpendicular to the plane defined by x and y-axes and is positive for the upper side of the wing.

A convergence study was performed with several mesh element sizes. For the convergence study, were selected two elements from the top cap at the constraint edge, since this was the critical stress region. Both elements are from the upper cap and the stress is monitored for the first ply. The first element is at the top corner and connects the cap with the front web. The second is the center element of the top cap. Both elements are marked in Figure 4.4. Due to the structure symmetry, convergence results are similar for the lower cap or to the other side of the cap.

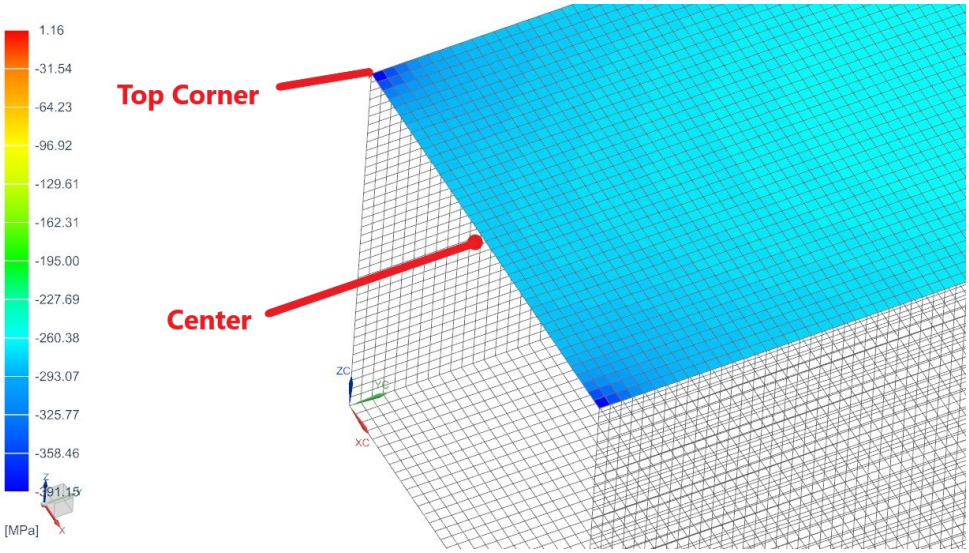

Figure 4.4: Spar's top cap ply 1 and convergence elements identification for a 1 mm element size mesh.

Stress (σ_{WP}) results at the two elements identified as well as the maximum stress value in the top cap and maximum displacement are presented in Table 4.9. For the two smallest meshes, maximum stress corresponds to the stress at the upper corner element. Figure 4.5 shows the stress variation in function of the mesh elements' number.

Table 4.9: Spar's top cap ply 1 linear static stress and displacement convergence.

	Top Corner Stress	**Center Stress**	**Maximum Stress**		
Element's Size	σ_{WP} **[MPa]**	σ_{WP} **[MPa]**	σ_{WP} **[MPa]**	**y-axis Location**	**Displacement [mm]**
10 mm	-286.64	-268.49	-375.09	100 mm	261.1
5 mm	-325.12	-288.32	-375.06	100 mm	243.4
2 mm	-360.92	-289.47	-382.48	100 mm	243.5
1 mm	-387.88	-289.88	-391.15	100 mm	243.5
0.8 mm	-395.38	-289.96	-395.38	0 mm	243.5
0.5 mm	-408.81	-290.08	-408.81	0 mm	243.5

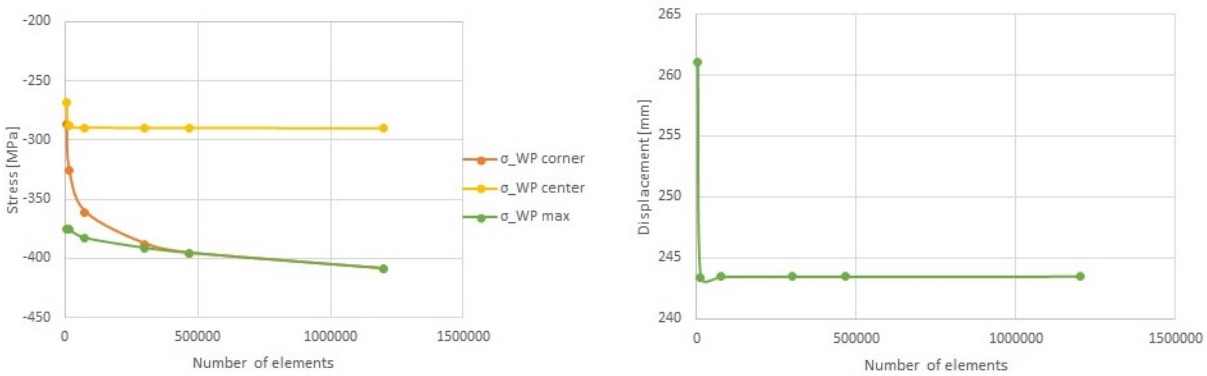

(a) Top cap ply 1 stress convergence.

(b) Displacement convergence.

Figure 4.5: Spar's linear static convergence graphics.

The displacement and the center stress convergence are achieved for a 2 mm element size mesh. The upper corner stress does not converge, thus it can be inferred that either is a stress singularity or a stress concentration. The second hypothesis can be put away since a thorough mesh refinement was performed and stress in that region never converged.

Taking into account results obtained, the static analysis of the spar is done with a 1mm element size mesh.

Stress Singularities

Stress singularities are points in the structure where pressure is theoretically infinite. It is one of the FEM analysis downsides, since decreasing the mesh will decrease the element's area and stress will increase infinitely (Skotny, 2022). Skotny explains several reasons that can lead to stress singularities in FEM analysis. Two of them apply to the spar analysis. The first is that there is a boundary condition applied to the spar's edge, which is a fixed constraint. The second explains why the effect occurs with greater intensity on the spar's corners. Skotny calls it sharp inside corners. It is related to the 90^{o} corner between caps and webs.

With this in mind, two problems must be solved. The first is whether the structure analysis is compromised or not. The second, if it is not compromised, is how to obtain the approximate stress value.

Saint Venant's principle states that further away from the stress singularity the results will not be disturbed (Acín, 2022). So, the analysis in regions away from the singularity is not compromised. Therefore the stresses at the singularity may be ignored if it happens in a region of no interest. This is not the case, since there is a connection between the cap and the web at the singularity and it is expected a stress increase in this region. Therefore, is a high probability for the laminate to fail.

Both authors, Skotny and Acín, propose several solutions to estimate the real stress value on singularity points. One is to change from a linear model to a nonlinear one. For example, using an elastic-plastic material model, the material would yield at the stress singularity, instead of having infinite stress. Another one is to model a fillet on the inside of the sharp corner between the cap and the web. This would allow stress concentrations to be reduced. A similar approach is used on airplanes' pressurized

cabin windows which have rounded corners in order to reduce stress concentration.

Both options are out of the scope of this work and are not applied. The first one requires to use other material than a fiber-reinforced composite laminate. The second implies a structural design modification that is not feasible. A third option is to estimate where stress singularities start along the constraint edge by using Saint Venant's principle and a mesh refinement study. It is possible to use the converged elements along the constraint edge to obtain tendency curve and estimate the stress value at the singularity point. Although this method does not provide the real stress value, it gives a good approximate value.

For meshes with element sizes equal to or lower than 2 mm (assumed convergent), it is possible to extract the worst principal stresses for the elements from the center (element 1) to the upper corner constraint edge (element 10). Results obtained are presented in Table 4.10. The standard deviation of each element for the different mesh sizes, shows if it is affected by the singularity or not. From the results in Table 4.10, it is possible to conclude that element 8, 9, and 10 stress values are affected by the singularity. Figure 4.6 shows a graphical perspective of converged and non-converged values.

Table 4.10: Spar's top cap ply 1 constraint edge principal stresses, in MPa.

Element	2 mm	1 mm	0,8 mm	0,5 mm	S.D.
1	-289.47	-289.93	-289.95	-290.08	0.2314
2	-289.68	-290.18	-290.14	-290.26	0.2271
3	-290.14	-290.70	-290.67	-290.66	0.2314
4	-290.97	-291.61	-291.30	-291.38	0.2291
5	-292.36	-293.15	-292.92	-293.05	0.3048
6	-294.71	-295.81	-296.04	-295.50	0.5002
7	-298.90	-300.68	-299.78	-299.99	0.6355
8	-306.73	-310.50	-311.36	-312.73	2.2257
9	-323.67	-332.83	-343.50	-339.47	7.5071
10	-360.92	-387.88	-395.38	-408.80	17.4690

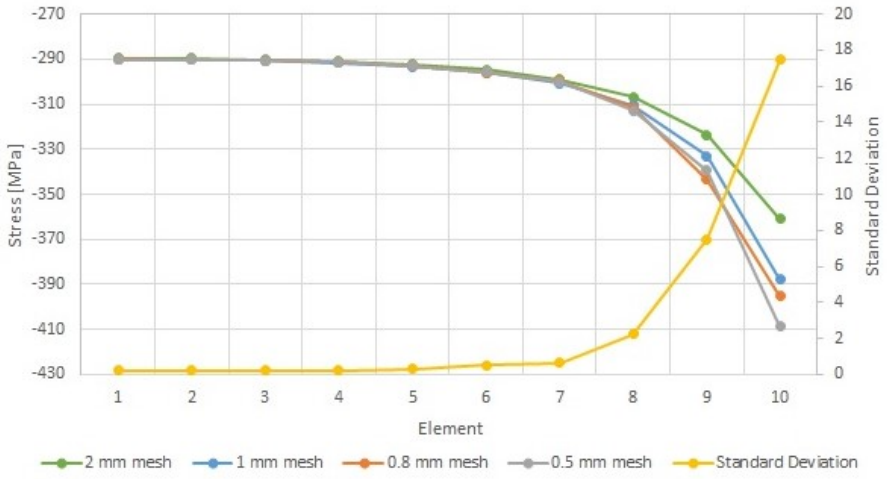

Figure 4.6: Spar's top cap ply 1 constraint edge convergence.

Once it is known the elements affected by the singularity, a polynomial regression is performed with the remaining elements. It was found that a first-order linear regression was a poor approach. There was a significant difference between the tendency line and the analysis results. The coefficient of determination (R^2) was low, between 0.818 and 0.836, which suggested that the polynomial order should be increased.

Table 4.11 presents the results obtained for quadratic regressions, and Figure 4.7 shows the match between the analysis values and the tendency lines.

Table 4.11: Spar's top cap ply 1 quadratic regressions' stress at singularity.

Mesh	R^2	Stress at Singularity [MPa]
2 mm	0.988	-312.62
1 mm	0.986	-316.36
0.8 mm	0.993	-314.75
0.5 mm	0.989	-314.96

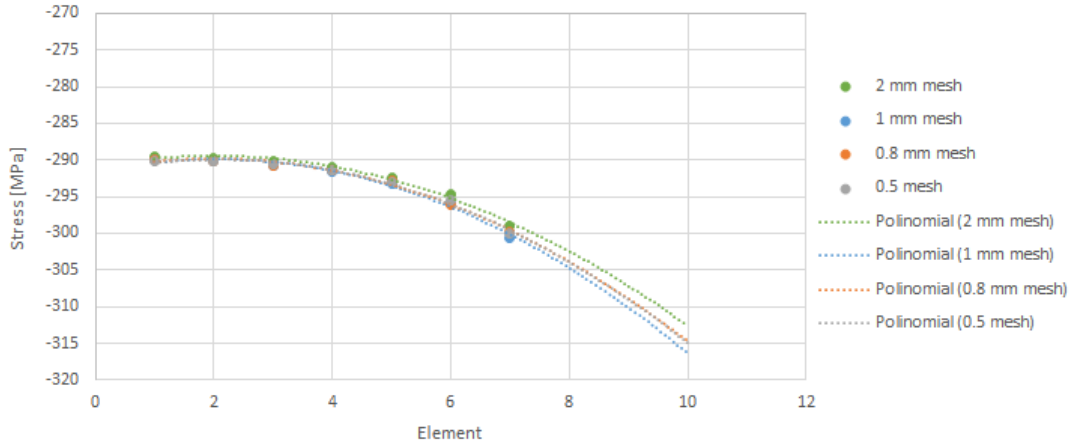

Figure 4.7: Spar's top cap ply 1 quadratic regressions graphical results.

The mean values of the quadratic regression are presented in Table 4.12. It can be observed that R^2 is close to one and that the S.D. between mesh refinements is very low, which means that there is a good fit between the tendency line and the data set. Also, the singularity stress value has a small variance for the meshes used in the study. The relative difference between the estimated top corner mean stress for the quadratic regression and the 1 mm mesh numerical value was -18.87%.

Table 4.12: Spar's top cap ply 1 quadratic regressions' mean stress at singularity.

R^2	R^2 S.D.	Stress at Singularity [MPa]	Stress S.D.
0.989	0.002	-314.67	1.34

Stress Discontinuities

Besides stress singularities at the constraint region, a different, but similar, problem occurred at the laminates discontinuities due to the ply's drop-off modeling. Every time the caps or webs' number of plies decreased a stress discontinuity occurred due to the sudden decrease in the material's thickness. Figure 4.8 shows the top cap first ply discontinuity at 100 mm from the constraint.

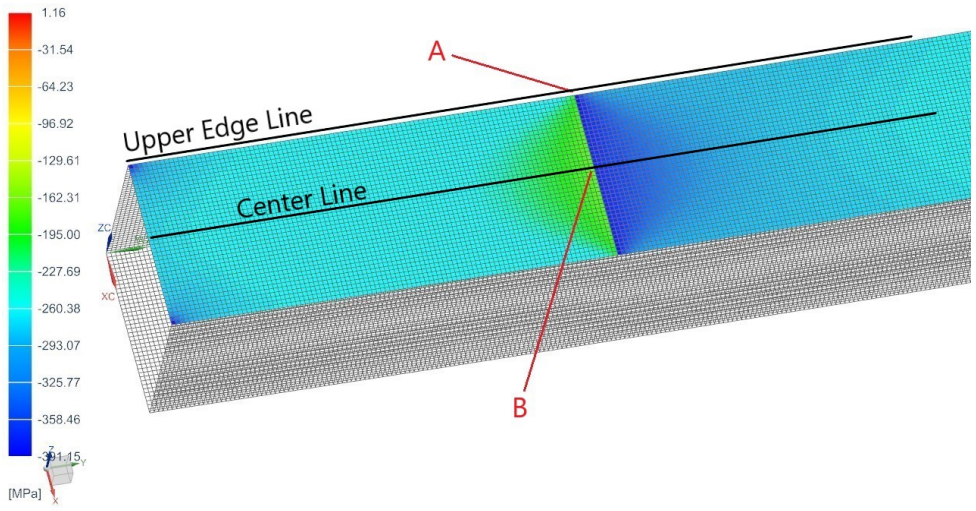

Figure 4.8: Spar's top cap ply 1 stress discontinuity at 100 mm distance from the constraint.

Across a plane at $y = 100mm$, the stress difference is 196.32 MPa at point A (see Figure 4.8). At the same plane, in point B, the difference is 201.71 MPa. The stress values at the left side of the plane are -197,40 and -179.08 MPa, respectively. This means that the stress approximately doubled in this discontinuity. Due to the uniformly distributed load along the spar, the bending moment will decrease quadratically from the cap's root to the tip. Eq. (4.1) shows the generic beam bending moment with respect to the x-axis (M_x) due to a uniformly distributed load, where $y = 0$ at the spar's root. Span-wise axial stress will then vary according to eq. (4.2), with $z = 0$ at the beam's cross-section centroid, and I_x being the spar's cross section area moment of inertia in order to the x-axis.

$$M_x(y) = F \cdot (1900 - y) \cdot \frac{(1900 - y)}{2} = \frac{F}{2} \cdot (1900 - y)^2 \tag{4.1}$$

$$\sigma_{yy}(z) = -\frac{M_x \cdot z}{I_x} \tag{4.2}$$

Taking into consideration eq. (4.2), the area moment of inertia is the only term changing from one side of the discontinuity to the other. Eq. (4.3) is used to calculate the area moment of inertia of a rectangle with respect to the x-axis, passing through its centroid. Being the the width (b) of the rectangle parallel to the x-axis, while its height (h) is parallel to the z-axis.

$$I_x = \frac{bh^3}{12} \tag{4.3}$$

The spar cross-section moment of inertia can be calculated as the difference between the outer and inner rectangular moments of inertia. Table 4.13 presents the area moment of inertia before (laminate with 5 plies) and after (laminate with 4 plies) the discontinuity.

Table 4.13: Spar's cross-section area moment of inertia, in mm^4.

	5 Plies		**4 Plies**	
Outer Rectangle	**Inner Rectangle**	**Cross-section ($I_{x,5}$)**	**Inner Rectangle**	**Cross-section ($I_{x,4}$)**
182907	146971	35936	153159	29748

The theoretical stress increase from the root to the tip of the spar at the $y = 100mm$ discontinuity was obtained through eq. (4.4), where the number in the subscript indicates the number of plies.

$$\frac{\sigma_{yy,4}(z)}{\sigma_{yy,5}(z)} = \frac{-\frac{M_x \cdot z}{I_{x,4}}}{-\frac{M_x \cdot z}{I_{x,5}}} = \frac{I_{x,5}}{I_{x,4}} \tag{4.4}$$

The expected variation of the stress for this change of area moment of inertia is 21%, much lower than the result obtained in the numerical simulation. Therefore, this does not justify why the stress doubled its value, whilst thickness only decreased from five to four plies.

Stress values along the cap's upper edge and center lines (see Figure 4.8) were extracted and plotted for the 2 mm, 1 mm, and 0.5 mm meshes for $0\ mm < y < 200\ mm$ (see Figures 4.9 and 4.10, respectively). The standard deviation values are also presented in both graphics, as they allow to identify the non-converged results. As expected, Figure 4.9 shows that the S.D. of the cap's edge's values is very high at the spar's constraint ($y = 0\ mm$), where it has a stress singularity as shown before. However, the S.D. is also significantly high at the laminate discontinuity ($y = 100\ mm$) in the cap's edge. This means that stress singularities also occur in the cap's edges' laminate discontinuities. The S.D. value is lower since there is no constraint, and the singularity is only affected by the laminate discontinuity and the sharp edge between the cap and the web.

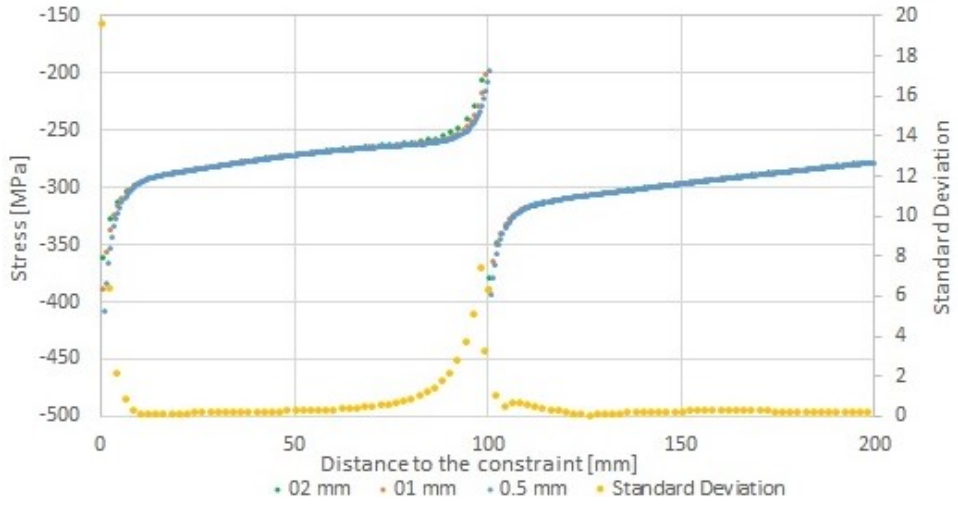

Figure 4.9: Spar's top cap ply 1 stress discontinuity at $y = 100mm$ - upper edge stress.

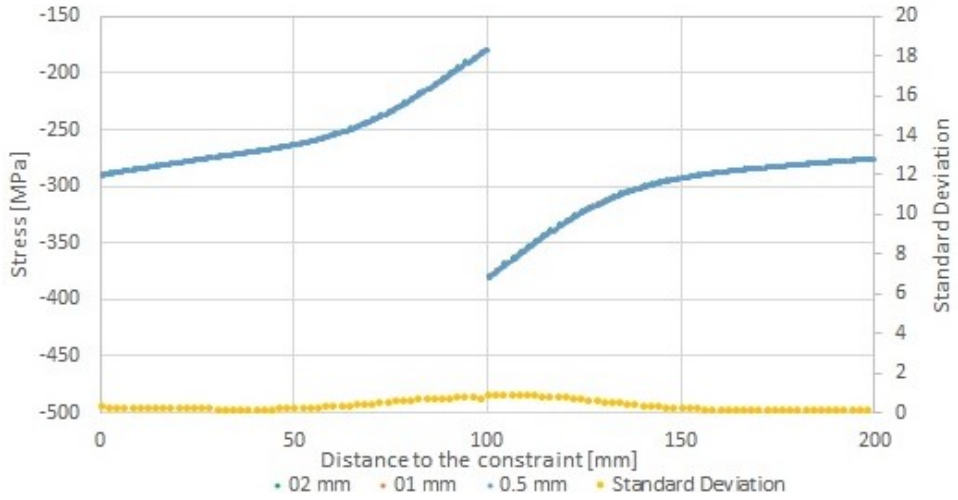

Figure 4.10: Spar's top cap ply 1 stress discontinuity at $y = 100mm$ - center line stress.

On the other hand, Figure 4.10 shows that the S.D. for the center line at the laminate discontinuity is very low. This means that the laminate discontinuity, by itself is not enough to create a stress singularity. Mortensen and Thomsen (1998) state that modelling layer drop-offs on laminate discontinuities will induce local bending effects, such as interlaminar and bending stresses.

Linear Static Results

The linear static results for the three resins are presented in the following tables. Only outer plies are presented since those are the ones with higher stresses. Table 4.14 summarizes the displacement difference between the three models. Comparing differences between displacement and stress, the first one had the most accentuated. Resin 3 displacement was 8% lower than resin 1. Since the displacement's wingspan percentage results are high, linear buckling analysis will dictate whether the structure needs greater stiffness or not.

Table 4.14: Spar's displacement comparison.

	Displacement [mm]	**Difference to Resin 1 [%]**	**Wingspan Percentage**
Resin 1	243.5	-	12.2
Resin 2	232.7	-4.4	11.6
Resin 3	223.9	-8.0	11.2

Stress values for the lower cap are presented in Table 4.15. Maximum stress for the outer ply was achieved in the second laminate discontinuity at $y = 300mm$. All maximum stresses were lower than the materials' ultimate strength. This means that ply failure does not occur. Relative to the laminate failure theory, it was not possible to implement any method on the software. Although the fact that the highest stress values occurred for stress singularity elements, the software would be falsely warning the user. This means these points must be analysed with extra care. Figure 4.11(a) presents the worst principal

stress distribution on the lower cap's first ply, where a black circle indicates the maximum stress element.

Table 4.15: Spar's lower cap stresses comparison.

	Upper Corner Stress		Center Stress		Maximum Stress	
	σ_{WP} [MPa]	Difference [%]	σ_{WP} [MPa]	Difference [%]	σ_{WP} [MPa]	Difference [%]
Resin 1	387.88	-	289.87	-	406.98	-
Resin 2	380.75	-1.8	285.18	-1.6	400.56	-1.6
Resin 3	377.74	-2.6	283.53	-2.2	398.26	-2.1

Table 4.16 shows the results for the spar web. Since the structure is symmetric, the results are equal for both webs. The maximum stress occurred at the root constraint at the upper corner (see black circle in Figure 4.11(b)). Once again, maximum stresses were lower than the ultimate strength. Greater stress differences were achieved for bidirectional fibers than unidirectional ones. These reached 3.5% on the center region, compared to the 2.6% on the lower cap top corner.

Table 4.16: Spar's back web stresses comparison.

	Upper Corner Stress		Center Stress	
	σ_{WP} [MPa]	Difference [%]	σ_{WP} [MPa]	Difference [%]
Resin 1	-116.86	-	-11.71	-
Resin 2	-114.52	-2.0	-11.43	-2.4
Resin 3	-113.32	-3.0	-11.30	-3.5

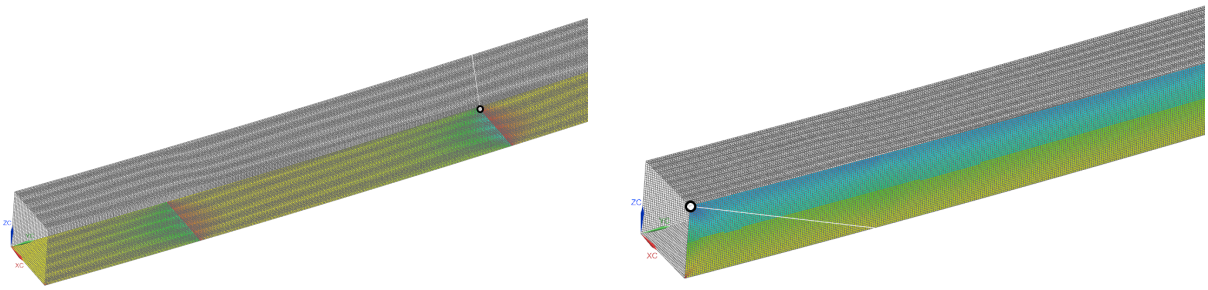

(a) Lower cap ply 1.

(b) Back web ply 1.

Figure 4.11: Spar's maximum stress results.

4.2.3 Linear Buckling Analysis

To start the linear buckling analysis, it was a made a convergence study to guarantee that the solution has converged. The design obtained in the static analysis was undersized for critical loads and it was necessary to reduce the wing load to 2% of the original value to have the simulation completed. The FEM software outputs a relative critical buckling load factor that must be multiplied by the load applied to

get the actual buckling load. Results are analysed in function of this factor that is identified as buckling factor from now on. For structural safety, the buckling factor must be higher than 1. Table 4.17 presents the relative critical buckling load factor for four different mesh sizes and Figure 4.12 shows the tendency in function of the mesh refinement. Results show that convergence is obtained for a mesh of elements with a 1 mm edge, which is used for further analysis.

Table 4.17: Spar's linear buckling convergence results. 2% of distributed load.

Element's Size	Critical Buckling Load Factor
10 mm	1.149
5 mm	1.089
2 mm	1.082
1 mm	1.081

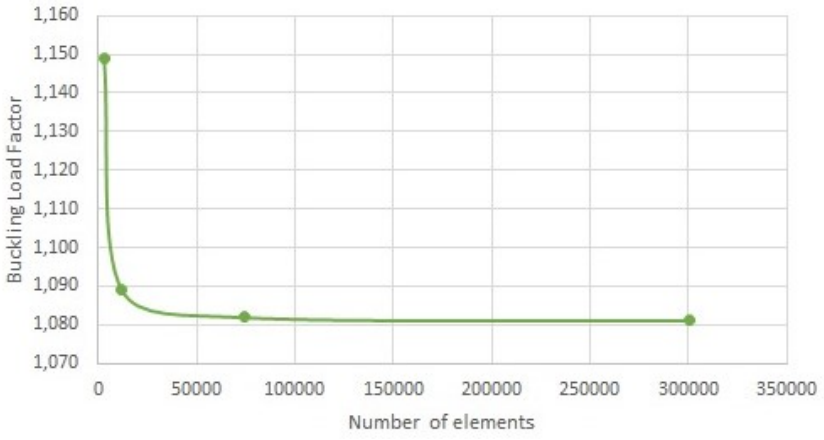

Figure 4.12: Spar's critical buckling load convergence graphic.

As mentioned before, it was necessary to reduce the applied load to 2% to have a buckling load of the magnitude of one. Therefore, the spar structure obtained from the linear static design is not suitable to withstand buckling loads.

It was necessary to reinforce the caps and webs of the spar. To reinforce the webs, two approaches were considered:

- Use a sandwich panel with a 3mm Airex C70 foam sheet as core;
- Increase the number of bidirectional plies of the web's laminate.

The approach used in the final design was selected in function of the component weight. To that end, the 3mm Airex C70 impregnated with epoxy weight (see Table 4.8) was compared with the weight of a monolithic panel of bidirectional and unidirectional carbon fibers. Taking into account Table 4.8, it was found that a monolithic panel of 5 or more plies of bidirectional carbon fiber is heavier than the 3 mm

Airex C70 impregnated with epoxy. The same study showed that a monolithic panel of 4 or more plies of unidirectional carbon fibers is heavier than the Airex solution.

FEM simulations showed that a monolithic panel of 4 plies of bidirectional carbon fibers, with two extra outer bidirectional plies, was not enough to overcome the buckling problem at the spar webs. On the other hand, the sandwich panel with a core of 3mm Airex sheet plus two bidirectional outer plies solved the buckling problem. Therefore, the sandwich panel solution proved to be the lighter one for the buckling problem.

The spar caps also had to be reinforced with extra unidirectional plies. Table 4.18 presents the laminate configuration of the lower and upper cap along the wingspan. Recalling the nomenclature, base value represents the number of plies, while the exponent is the number of sections (with 100 mm of length) having that number of plies. The spar webs are a sandwich panel with two bidirectional plies at 45 degrees and a core of 3 mm Airex C70 sheet. From now on, this spar model will be called spar's model 2, while the one obtained after linear static analysis was model 1.

Table 4.18: Spar's model 2 laminate distribution after buckling analysis.

Top Cap	**Lower Cap**
7^3 / 6^3 / 5^4 / 4^3 / 3^3 / 2^3	6^1 / 5^2 / 4^3 / 3^4 / 2^9

Tables 4.19 to 4.21 presents the static analysis results for the new spar design. Table 4.19 shows that the displacements for model 2 decrease by 32% when compared with model 1. Table 4.20 shows that the maximum stress (σ_{WP}) value decreased by 23.4% for all resins. Furthermore, the maximum stress at the lower cap occurs at $y = 100mm$ discontinuity, instead of $y = 300mm$. Table 4.21 presents the results for the spar web. In this case, the maximum stress is obtained at the lower corner of the web instead of at the upper corner. This happens because the upper cap was more reinforced than the lower cap, leading to higher stiffness at the top. The maximum stresses increased by 19%, compared to model 1 analysis. The stress singularities occurring at the webs' corners are responsible for the increase of the stress. Figure 4.13 presents the stress distribution from both plies and their respective maximum values.

Table 4.19: Spar's displacement comparison after buckling analysis.

	Displacement [mm]	**Difference [%]**	**Wingspan [%]**
Resin 1	165.5	-	8.3
Resin 2	158.4	-4.2	7.9
Resin 3	152.6	-7.8	7.6

Table 4.20: Spar's lower cap stresses comparison after buckling analysis.

	Upper Corner Stress		Center Stress		Maximum Stress	
	σ_{WP} [MPa]	Difference [%]	σ_{WP} [MPa]	Difference [%]	σ_{WP} [MPa]	Difference [%]
Resin 1	213.60	-	214.83	-	311.69	-
Resin 2	209.29	-2.0	211.16	-1.7	306.89	-1.5
Resin 3	207.33	-2.9	209.73	-2.4	305.17	-2.1

Table 4.21: Spar's back web stresses comparison after buckling analysis.

	Upper Corner Stress		Center Stress		Maximum Stress	
	σ_{WP} [MPa]	Difference [%]	σ_{WP} [MPa]	Difference [%]	σ_{WP} [MPa]	Difference [%]
Resin 1	-138.94	-	7.44	-	157.42	-
Resin 2	-136.28	-1.9	6.84	-8.1	154.47	-1.9
Resin 3	-135.00	-2.8	6.40	-14.0	153.10	-2.8

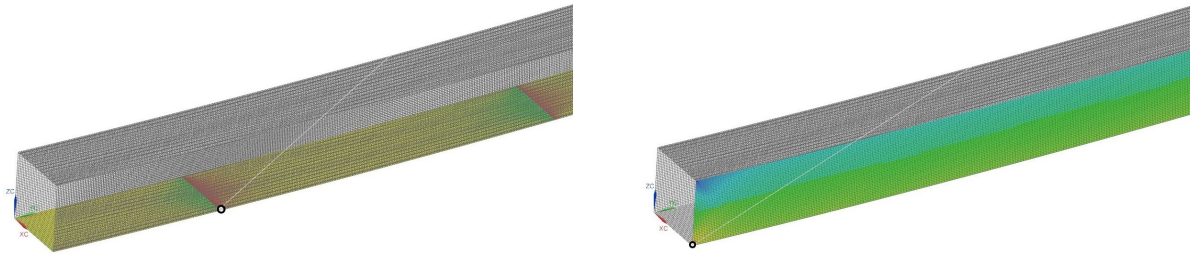

(a) Lower cap ply 1.

(b) Back web ply 1.

Figure 4.13: Spar's model 2 maximum stress results.

The critical relative buckling load factors for the three resin's first buckling mode are presented in Table 4.22. Deformations of the first five buckling modes occurred in the top cap, specifically in the first half-length, since this region is subjected to compressive loads.

Table 4.22: Main spar's critical relative buckling load factor and comparison with resin 1 value.

	Mode 1	
	Critical Buckling Load Factor	Difference [%]
Resin 1	1.087	-
Resin 2	1.154	6.2
Resin 3	1.193	9.8

Figure 4.14 shows the spar model 2 static response in a 2D side view. Figure 4.15(a) presents the

same 2D side view of the spar model 2 buckling's mode 1 response with a deformation enlargement scale of 10% of the spar's length. Despite numbers 1 and 3 on the last figure being under the spar, those represent top cap buckling valleys. No buckling deformations occur in the lower cap and the webs for the first mode. Figure 4.15(b) presents the same spar with a 3D view and a close-up of the buckling deformation (without scale factor applied). The three numbers correspond to the same three from Figure 4.15(a).

Figure 4.14: Spar's linear static analysis response. Deformation at 1:1 scale.

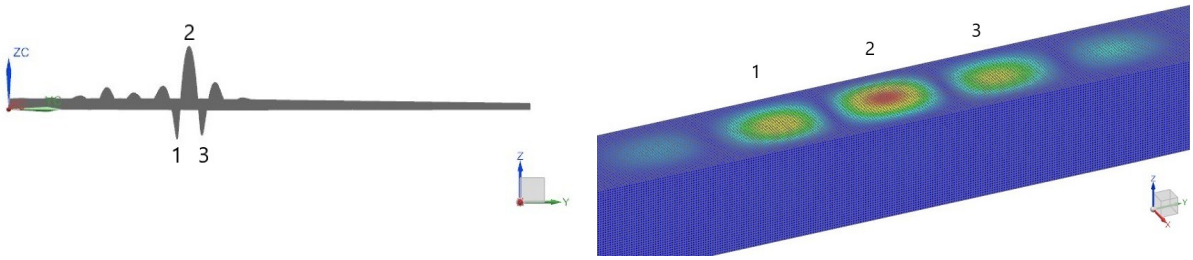

(a) 2D side view. Deformation at 10% model.

(b) 3D perspective view. Deformation at 1:1 scale.

Figure 4.15: Spar's linear buckling analysis mode 1 response.

4.3 Wing Design

In this section, the wing design process is described in detail. The wing structure is designed to withstand the ultimate load and it is used linear static and buckling analysis in the process. Three main designs were obtained that henceforward will be named initial design, static design, and buckling design. The final design's, buckling design, performance is compared for the 3 matrix systems used in this work.

Due to the results of the comparative study, two new designs are considered: first, it is proposed a wing structure configuration using components manufactured with resins 1 and 3; second, using these two resins in the manufacturing of the composite laminates, it is proposed a lighter design while fulfilling all requirements. For future reference, these designs will be named resin mix design and light design, respectively.

4.3.1 Initial Wing Design

As a first approach to the wing design, it was considered to include the spar model obtained in Section 4.2.3 in the wing baseline design (see Section 4.1.2). This structural model was discretised using 4 mm elements size and analysed for the aerodynamic load considered by Sá (2021). Sá has done a convergence study of the wing mesh and proved that the results converge for a mesh with 4 mm elements size. The model is subjected to linear static and buckling analysis.

Linear static analysis shows that the maximum stress occurs at the wing root at the main spar lower cap upper corner, which is the closest to the wing's leading edge. Maximum stress is 41.5% lower than the ultimate design strength value given in Table 4.8.

Buckling occurs in the wing skin as expected. However, the buckling load is 0.239, which means that the skin must be reinforced.

Although the wing structure fulfills all static requirements, the structure is oversized because the main spar's maximum stress is much lower than the allowed values. Therefore, this design is rejected and it is used Sá's wing design as the initial design for the static and buckling analysis. Sá's wing design has been validated for linear static load but it was not designed for buckling load. The wing initial design can be consulted in Section 4.1.2.

4.3.2 Linear Static Analysis

The wing's initial design was analysed for linear static load and the displacement results revealed convex deformations on the top skin and concave deformations on the bottom skin. These deformations are more evident near the wing root, closer to the second rib. This means that the two laminates used for the skin structure are not stiff enough to guarantee that the wing airfoil remains unchanged. It was necessary to reinforce the wing panels with extra plies. In order to control the weight, the extra plies were applied with a drop-off scheme in the spanwise direction. At the root, eight plies were applied that decreased continuously in the spanwise direction to two plies. Figure 4.16 shows the wing skin areas with different laminates, and Table 4.23 presents the number of layers per zone. A design that fulfills all linear static requirements, named static design henceforward, is obtained with this change.

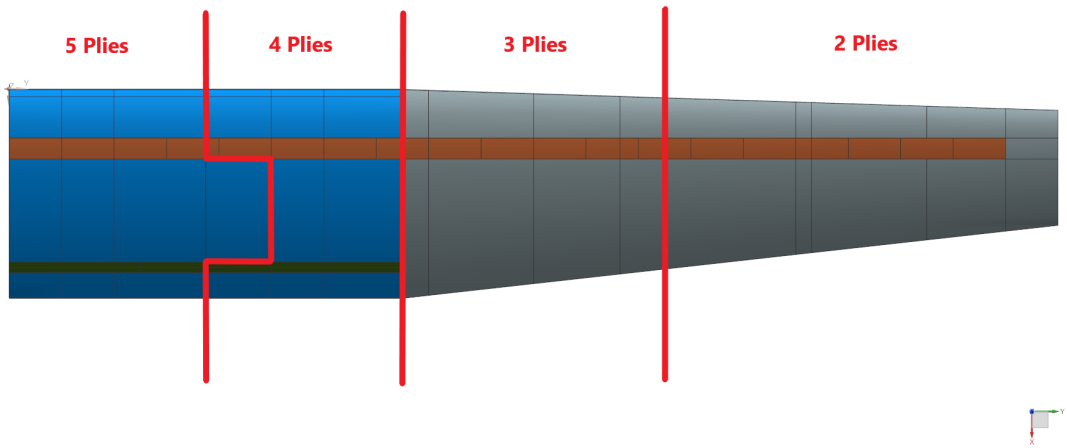

Figure 4.16: Static design - plies distribution along the span-wise.

Table 4.23: Static design - lay-up scheme.

Number of Plies	5	4	3	2
y-axis Position [mm]	0 - 375/500	375/500 - 750	750 - 1250	1250 - 2000

The following figures present the initial wing design versus the static design. Figure 4.17 presents a side view from the wing's trailing edge where it is possible to observe the skin deformation near the second rib.

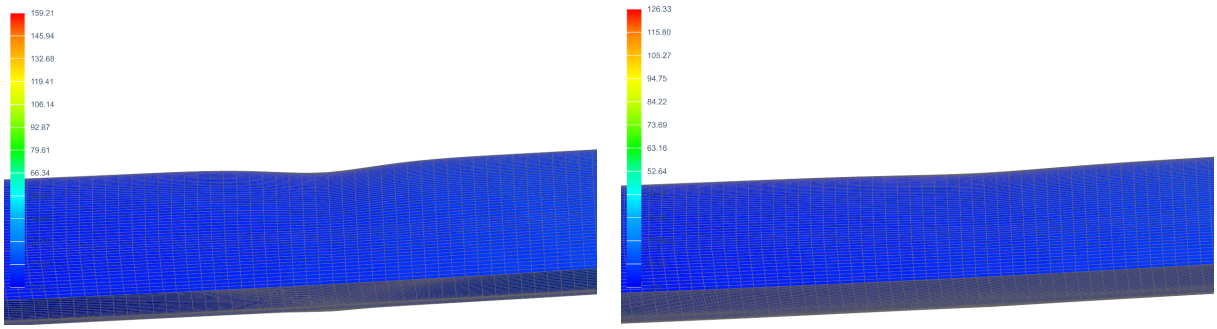

(a) Initial wing design.

(b) Static design.

Figure 4.17: Skin deformation near second rib for the initial design and static design.

Figure 4.18 plots the rotation values at the mesh nodes, which makes more evident the skin deformations, at the wing bottom skin. It is possible to observe that the initial design has a concave deformation between the first and second rib (see Figure 4.18(a)), while the static design has a smoother skin when subjected to the ultimate load factor (see Figure 4.18(b)).

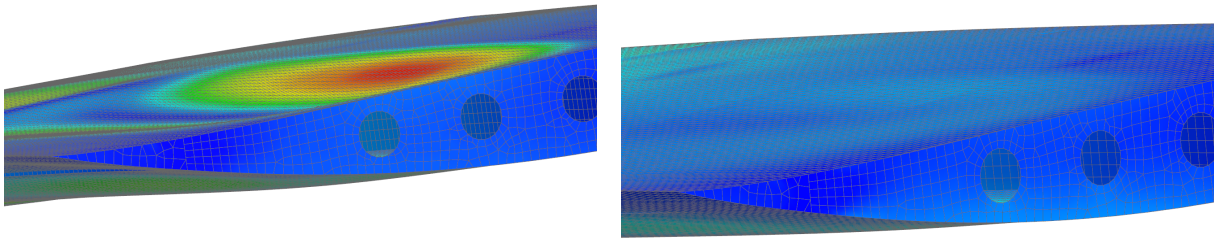

(a) Initial skin design. (b) Static design.

Figure 4.18: Bottom side skin nodal rotation near the second rib for the initial design and static design.

For the static design, maximum stress values are obtained at the main spar constraint and the surrounding areas. Figure 4.19 presents the wing's outer ply's worst principal stress. It is possible to observe that maximum stress occurs at the main spar constraint, more precisely on the corner furthest away from the leading edge. For bidirectional fibers, this maximum stress is obtained at the skin corner connection with the top cap. Maximum stress at unidirectional fibers is obtained at the top cap third ply (outermost unidirectional ply). These results may be stress singularities. Therefore, a convergence study is performed and the stress tendency at the constraint is analysed, both for the spar cap and wing skin.

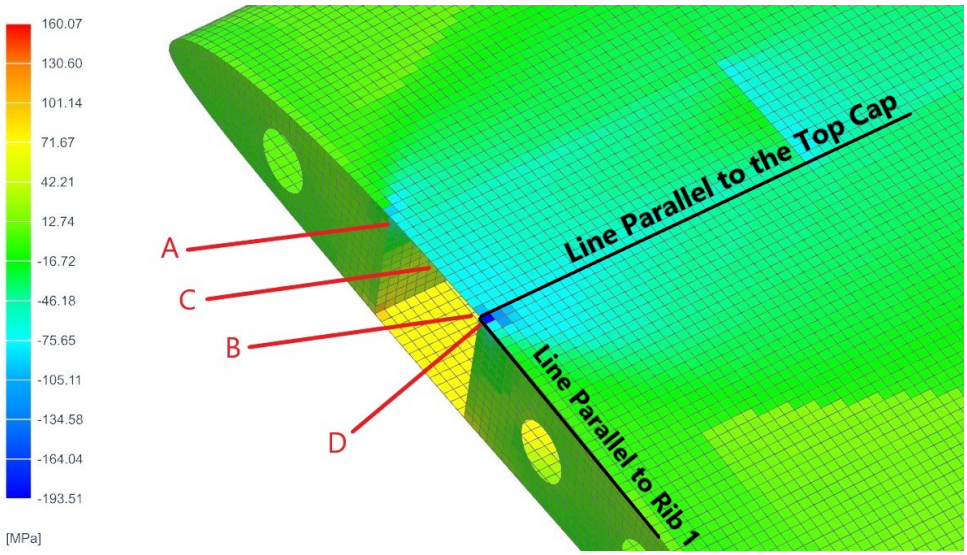

Figure 4.19: Wing's top side ply 1. Convergence elements identification. 3 mm element size mesh.

The convergence study was made for the skin's outer ply. Tendency lines are plotted in Figure 4.20 for points A, B, C, and D identified in Figure 4.19 for different mesh sizes.

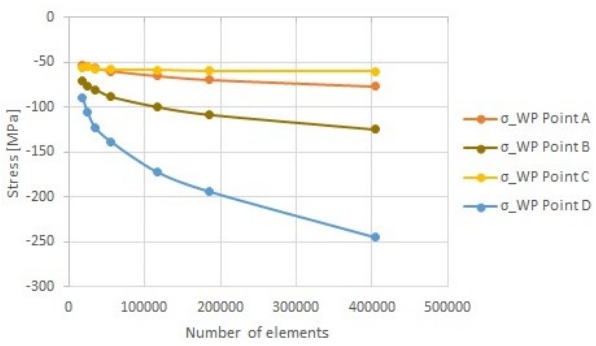

(a) Top cap ply 1 stress convergence.

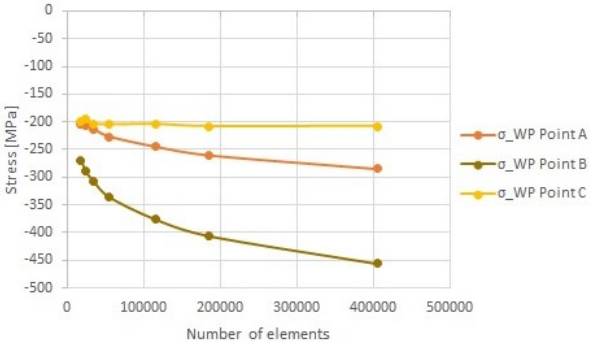

(b) Top cap ply 3 stress convergence.

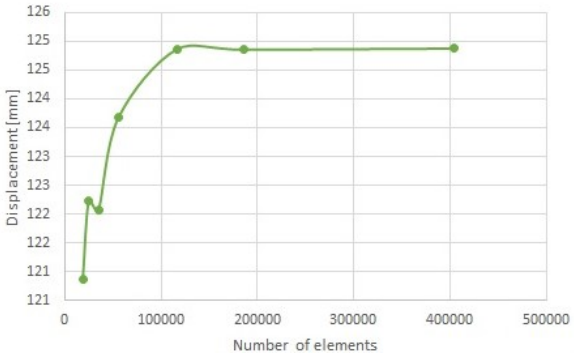

(c) Displacement convergence.

Figure 4.20: Wing mesh convergence study.

From the convergence analysis, one can infer that the stress maximum values obtained for the top cap and the skin did not converge, while their surroundings did. Convergence is achieved for a 4 mm mesh element size. Therefore, the study carries on with a 3 mm mesh element size.

As expected, maximum stress values at the root constraint are stress singularities. A study with 4 mm, 3 mm, and 2 mm element size meshes is made to obtain stress estimates at the singularity points. Stress variations along the top cap constraint edge for ply 1 and 3 are plotted in Figures 4.21(a) and 4.21(b), respectively.

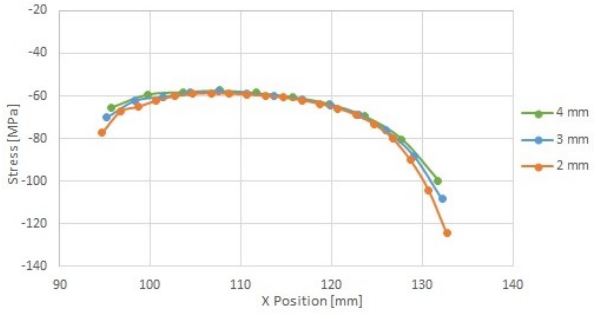

(a) Top cap ply 1.

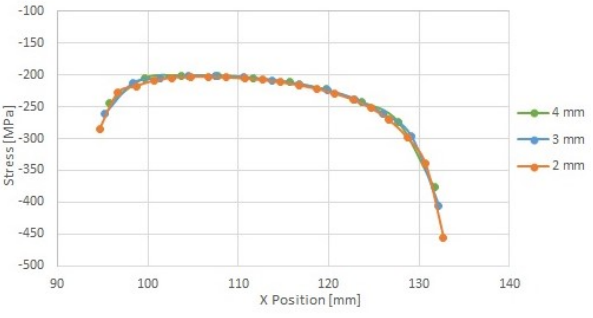

(b) Top cap ply 3.

Figure 4.21: Wing main spar top cap constraint edge stress convergence.

Quadratic regressions were traced from the converged values in Figure 4.21. The R^2 and the stress at singularity (σ_{WP}) mean results from the 4 mm, 3 mm, and 2 mm meshes are presented in Table 4.24, along with the respective S.D. values. The difference between the estimated mean stress at the singularity and the obtained value for the same point in the numerical solution for the 3 mm mesh is also shown.

All R^2 and their respective S.D. values have good results, which means that the regression is appropriate for the converged results. Still, the unidirectional carbon fiber ply (ply 3) had high S.D. values for the stress at the singularity. Despite that, stress at the singularity differences from the obtained value for the 3 mm mesh were within what was expected, and also similar to the -18.87% obtained in the main spar analysis (see Section 4.2.2), which means that these values can be accepted for failure load criteria.

Table 4.24: Wing's main spar's top cap quadratic regressions' mean stresses at singularities.

		R^2	R^2 S.D.	σ_{WP} [MPa]	Stress S.D.	Difference (3 mm mesh)
Ply 1	**Point A**	0.989	0.006	-67.52	2.77	-3.40%
	Point B	0.989	0.006	-89.22	4.06	-17.67%
Ply 3	**Point A**	0.993	0.003	-218.66	12.54	-16.04%
	Point B	0.993	0.003	-324.12	23.50	-20.12%

To study the stress singularity at the skin corner (point D) two approaches were followed. The first, which will be called method 1, was to analyse stress values of the elements from the skin's edge parallel to the top cap (see Figure 4.19). The second was method 2 where the same analysis was performed on the edge parallel to rib 1. Figure 4.22(a) presents the first method stress results for the same three meshes used before on the top cap analysis, where results do not have completely converged along the edge. This complicates choosing the converged interval to perform the quadratic regression. Figure 4.22(b), presents the same results for method 2. It shows that values have converged far from the singularity. However, before the singularity, where stress increases fast, results do not converge. Therefore, it is obtained a significant difference between the estimated value at the singularity and the result obtained with the 3 mm mesh. The difference is -55.51% and 70.89% for methods 1 and 2, respectively, as presented in Table 4.25.

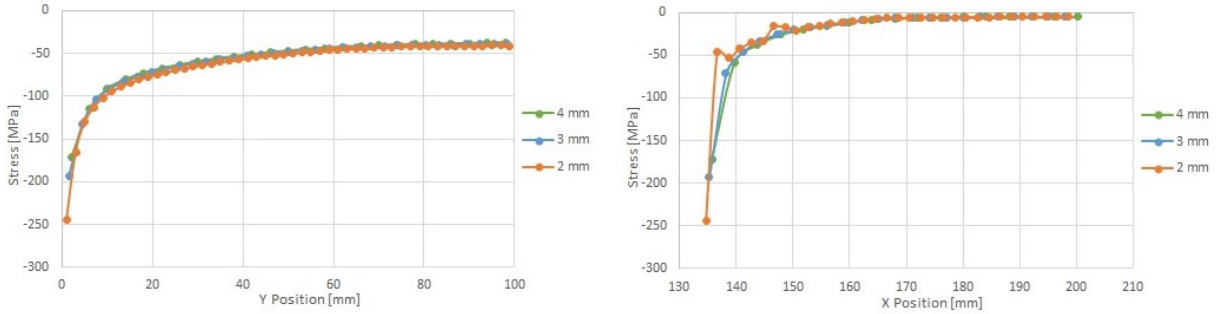

(a) Method 1.

(b) Method 2.

Figure 4.22: Wing's skin stress convergence.

Table 4.25 presents both approaches' results. For the second approach, it was used a cubic regression rather than a quadratic regression because it had a better fit to the converged results. The difference between the numerical simulation for the 3 mm mesh and the estimated stress values at the singularity point with both methods is very large, which means that this is the greatest stress singularity in the wing. Yet, method 1 mean stress (-86.10 MPa) is only 3.5% lower than the stress from the adjacent element on the spar cap, which was estimated to be -89.22 MPa (see Table 4.24). Since it is the most conservative value, it is adopted method 1 to estimate the stress value at the skin stress singularity.

Table 4.25: Wing's skin regressions' mean stress at singularity.

	R^2	R^2 S.D.	σ_{WP} [MPa]	Stress S.D.	Difference (3 mm mesh)
Method 1	0.997	0.001	-86.10	3.40	-55.51%
Method 2	0.998	0.001	-56.33	13.57	-70.89%

Summarizing, all obtained stress values were lower than the ultimate design strength. The displacement of this model was 124.8 mm, which represents 6.2% of the wingspan.

4.3.3 Linear Buckling Analysis

The static design was analysed for linear buckling using the 3mm mesh size from the linear static analysis. Buckling occurred at the main spar's webs with a relative critical buckling load factor of 0.179, much lower than 1 (minimum value admitted). To solve that issue, the spar's webs were replaced by a sandwich panel with a core of 3mm Airex C70 sheet and one bidirectional carbon fiber ply on each side (same solution used in Section 4.2.3).

With this modification, buckling occurred in the top skin between both spars for a relative buckling load of 0.759. In order to stiffen the skin, the skin laminate was reinforced with more bidirectional plies with a drop-off scheme from the root to the tip. The final design for the skin was obtained in an iterative manual process until reaching a relative buckling load greater than 1. Figure 4.23 presents the skin laminate zones between both spars. The leading and trailing edge and the bottom side of the wing drop-offs were kept the same from the static design. The lay-up scheme is indicated in Table 4.26.

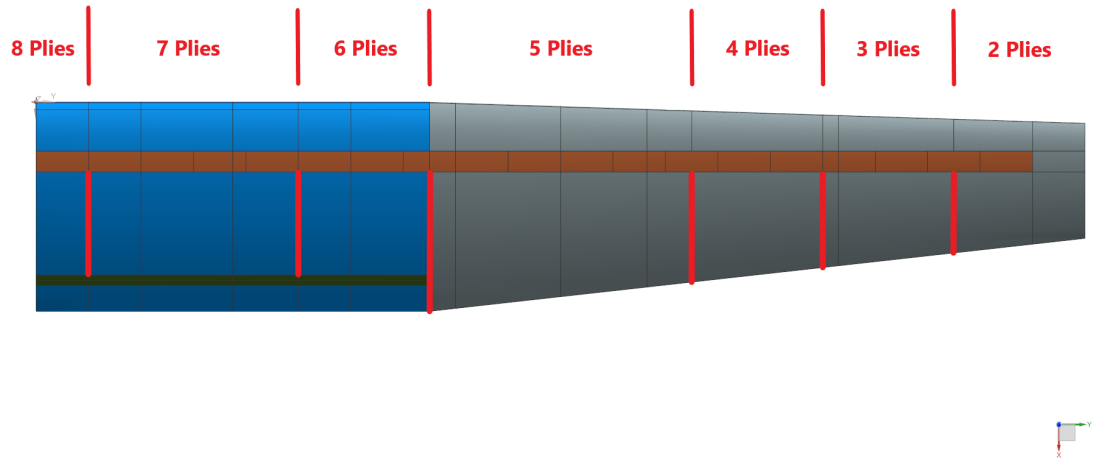

Figure 4.23: Buckling design - plies distribution along the span-wise.

Table 4.26: Buckling design - lay-up scheme.

Number of Plies	8	7	6	5	4	3	2
y-axis Position [mm]	0 - 100	100 - 500	500 - 750	750 - 1250	1250 - 1500	1500 - 1750	1750 - 2000

This design was used to perform the convergence study. Table 4.27 presents the relative critical buckling loads obtained for each mesh analysed in the previous section. From the graphical plot (see Figure 4.24) one can infer that buckling loads converge for the 6 mm mesh. This convergence has a low damping ratio, which leads to an oscillatory behavior of the result until it approximates the final converged value. Therefore the 3 mm mesh is used for further studies.

Table 4.27: Wing's linear buckling convergence.

Element's Size	**Critical Buckling Load Factor**
12 mm	1.046
10 mm	1,040
8 mm	1.039
6 mm	1.025
4 mm	1,027
3 mm	1,023
2 mm	1,025

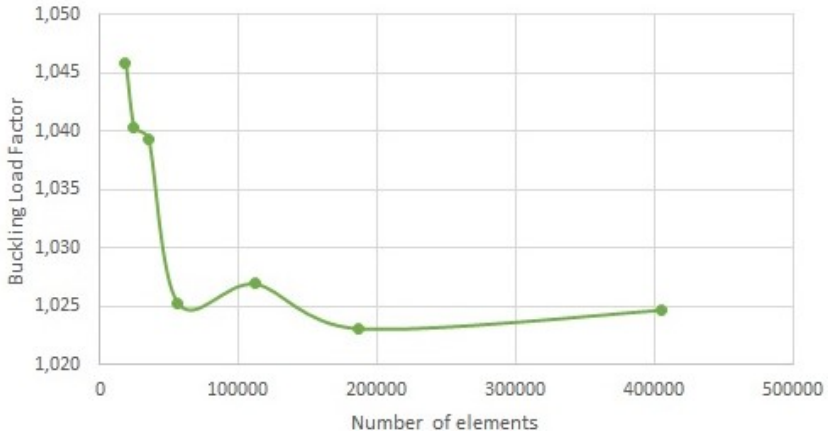

Figure 4.24: Wing's critical buckling load convergence graphic.

There are several methods to stiffen wing skin panels rather than monolithic composite laminates with a drop-off scheme. Two other possibilities were studied to try to obtain a lighter structure: 1) using a sandwich panel; 2) creating local reinforcements in the skin, similar to stringers, by adding localized unidirectional fiber reinforcements in the spanwise direction.

The first option only compensates if it is obtained a lighter skin panel. It must also be recalled that it was not possible to obtain the final structure's mass with Siemens NX FEM analysis mode, which would have proven fundamental for this thesis since mass results are fundamental in aeronautics. To estimate and compare the weight of the skin panel, it is considered the reinforced area (0.39 m^2) of the skin top, marked by the red line in Figure 4.25. Despite the skin having a small curvature from the airfoil, it is considered flat for the purpose of estimating its area. Using the information in Table 4.28, which presents the mass of all the materials per number of plies per square meter, the monolithic laminate with a drop-off scheme weight is 540.33 g while, for the same area, the sandwich panel, with one ply of bidirectional fiber on each side, weight is 704.94 g. For this example, both were made of resin 1. This means that the monolithic laminate with a drop-off scheme approach is 23.4% lighter than the sandwich panel with a core of Airex C70.

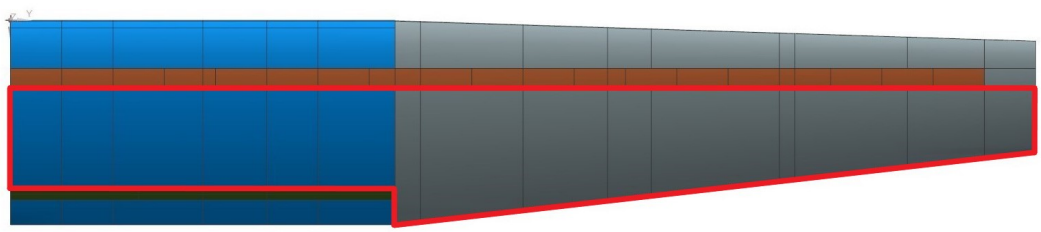

Figure 4.25: Wing's skin reinforced area.

Table 4.28: Carbon fiber laminates weight by number of plies, in g/m^2.

	Resin 1		Resin 2		Resin 3		Airex +
Number of Plies	**Bi-Carbon**	**Uni-Carbon**	**Bi-Carbon**	**Uni-Carbon**	**Bi-Carbon**	**Uni-Carbon**	**Epoxy**
1	270.77	372.33	270.61	372.90	272.74	375.84	1266.00
2	541.53	744.65	541.23	745.80	545.49	751.67	-
3	812.30	1116.98	811.84	1118.71	818.23	1127.51	-
4	1083.06	1489.30*	1082.46	1491.61*	1090.97	1503.34*	-
5	1353.83*	1861.63*	1353.07*	1864.51*	1363.72*	1879.18*	-

* Values higher than Airex + Epoxy's mass per square meter ($>$ 1266.00)

In the second option, the idea is to apply a unidirectional fiber tape in the span-wise direction to locally reinforce the skin. In this case, it was considered to apply a 50mm wide unidirectional laminate located at half distance from both spars (see Figure 4.26).

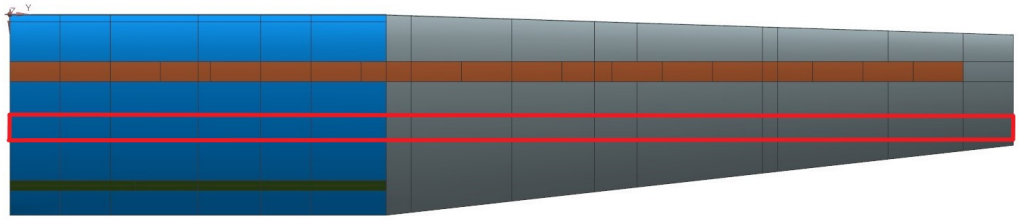

Figure 4.26: Wing's skin stringer area.

It was simulated a reinforcement with four plies and buckling occurred between the main spar and the reinforcement with a relative buckling load lower than 1. Increasing the reinforcement thickness does not solve the problem. Adding more local reinforcements would be almost equivalent to adding a complete skin ply and even though it would not guarantee to solve the problem. Preparing the CAD Model to include more local reinforcements is a complex task and time demanding. Therefore this option was not further explored.

The results obtained show that the monolithic laminate with a drop-off scheme is the best solution to solve the buckling problem at the skin.

Considering the results for the skin panel, the configuration of the spars' webs was revisited. The sandwich panel of both spars' webs was replaced by a monolithic laminate of four plies of bidirectional carbon fiber at 45^o. No buckling occurred in this structure, and the relative critical buckling load was 1.014. This value was also lower than the one obtained for the convergence study in Table 4.27 (1.023), obtained with a sandwich panel at the main spar webs. Table 4.29 presents the final laminate distribution of the main spar. The secondary spar has no layer drop-offs, which means the number of plies along its length is constant. Results for both caps and the web are presented in Table 4.30.

Table 4.29: Buckling design - main spar laminate distribution.

Top Cap	Lower Cap	Webs
5^1 / 4^3 / 3^3 / 2^4 / 1^8	5^1 / 4^2 / 3^3 / 2^4 / 1^9	4^{19}

Table 4.30: Buckling design - secondary spar laminate distribution.

Top Cap	Lower Cap	Webs
2	2	4

Concluding, the buckling design is comprised of:

- a main spar with the configuration described in Table 4.29;
- a secondary spar with the configuration described in Table 4.30;
- a leading/trailing edge and bottom side skin panel with a monolithic laminate of bidirectional carbon fiber plies at 45º with a drop-off scheme as depicted in Table 4.23;
- a top side skin panel between spar with a monolithic laminate of bidirectional carbon fiber plies at 45º with a drop-off scheme as depicted in Table 4.26;
- seven ribs, which were kept the same as the original model from Sá (see Table 4.6).

4.3.4 Matrix Comparative Results

The buckling design was used to study the impact of the 3 matrix solutions considered in this work. Table 4.31 presents the numerical simulation displacement results obtained for the 3 matrix models. The results are compared with resin 1, which is currently used in CIAFA. Wing tip displacement decreased by 6.1% when using resin 3 instead of resin 1.

Table 4.31: Wing's displacement comparison after buckling analysis.

	Displacement [mm]	Difference [%]	Wingspan [%]
Resin 1	112.1	-	5.6
Resin 2	108.2	-3.5	5.4
Resin 3	105.3	-6.1	5.3

Stress differences between the three resins were also obtained for different wing parts. Appendix B presents the obtained stresses for the corners and center of the constraint edges from both spars (see Tables B.1 - B.6). It also presents the maximum stresses obtained for the skin outer ply (see Table B.7), on both sides, and for the second rib (see Table B.8) which was the one with higher stress values.

The wing's maximum stress value occurs at the main spar's top cap singularity close to the skin region between spars for resin 1 (-431.22 MPa), which has already been analysed in Section 4.3.2. The back web obtained a maximum stress value of -95.36 MPa for the point adjacent to the previous. The secondary spar had lower values compared to the main spar, on both caps and web, where their values were -276.60 MPa and -31.92 MPa, respectively.

The skin had the highest mean stress difference between resin 1 and 3. Maximum stress for the top side of the wing was obtained at the singularity between both spars, close to the main spar. As for the bottom side, maximum stress was obtained for the same singularity between spars. Maximum values were, respectively, -199.85 MPa and -155.47 MPa, both for resin 1. It is noteworthy that the difference between maximum stress values between the leading edge (which was also close to the main spar) and the value between spars is much lower for the bottom side (9.4%) than the one from the top side (58.6%).

The ribs were the only part of the wing's structure that obtained lower stresses for resin 1 compared to the other two resins, specifically in the trailing edge area. Analysing rib 2 values, the leading edge and the region between spars, in general, had a slight decrease in stress for resins 2 and 3, having resin 2 registered the lowest stresses. Maximum bidirectional stress was 31.91 MPa obtained for the leading edge tip-side ply of resin 3, while the unidirectional highest value was attained for resin 1 on the region between both spars. In general, these differences were lower ($\approx$ -1.3%) compared to the differences obtained for the main spar ($\approx$ -3.1%), the secondary spar ($\approx$ -3.2%), and the skin ($\approx$ -4.6%).

Buckling analysis results are presented in Table 4.32. It is worth mentioning that from all three variables being studied, the relative critical buckling load was the one which had the highest difference between using resin 1 and 3 (11.0%). As opposed to displacements and stress, the relative buckling factor increased, leading to a stiffer structure. Deformations from the first buckling mode occurred on the skin's top side between spars and ribs 2 and 3.

Table 4.32: Wing's relative critical buckling load comparison after buckling analysis.

	Mode 1	
	Critical Buckling Load Factor	**Difference [%]**
Resin 1	1.014	-
Resin 2	1.083	6.8
Resin 3	1.126	11.0

Results show that resin 3 has better behavior than resin 1 on aeronautical structures. In particular, results show that there are opportunities to get a lighter structure since maximum stress values are lower than allowable material stress limits and the relative buckling load can be reduced. This means several modifications can be performed to the model in order to obtain the best mechanical properties and reduce the wing's weight.

4.3.5 Resin Mix Design

In order to reduce the relative buckling load to 1 while keeping maximum stress lower than the allowed values, the first modification performed was to mix resin 1 and 3 in the same model. To that end, it is identified the components that had lower stress values with resin 1.

After analysing the stress data in Section 4.3.4, it was decided to use resin 3 in the wing structure with the exception of the ribs and the wing tip which will be made of resin 1. This new design is called resin mix design henceforward. Tables 4.33 and 4.34 present the comparison between the displacement and relative buckling load for the resin mix design and the buckling design with resin 3.

Results show that there are no differences in the displacement, and the buckling load has a marginal decrease. Stress differences in the whole structure were also minimum. This modification allowed a small decrease in the wing's weight since resin 1 plies are lighter than the ones from resin 3.

Table 4.33: Wing's displacement comparison for the resin mix model.

Model	Displacement [mm]	Difference [%]	Wingspan [%]
Resin 3	105.3	-	5.3
Mix	105.3	0.0	5,3

Table 4.34: Wing's relative critical buckling load comparison for the resin mix model.

	Mode 1	
Model	**Critical Buckling Load Factor**	**Difference [%]**
Resin 3	1.126	-
Mix	1.125	-0.1

4.3.6 Light Design

The light design has the resin mixture from the resin mix design, while some plies are removed. The main goal is to reduce the number of plies from parts subjected to buckling because the behavior of the structure to buckling improved with the use of resin 3. Therefore, there is room to get a lighter structure while fulfilling the buckling criteria. The structural components considered in the study were the top skin panel, between the main and secondary spar, and the main spar top cap. There will be a trade-off between the relative buckling load decrease and the increase of the displacement.

An iterative process was performed to obtain a new ply configuration. The best solution achieved had some plies removed from the skin panels. It was not possible to remove material from the main spar top cap. The new configuration for the skin panel between spars is depicted in Figure 4.27, and the new laminate zones are presented in Table 4.35.

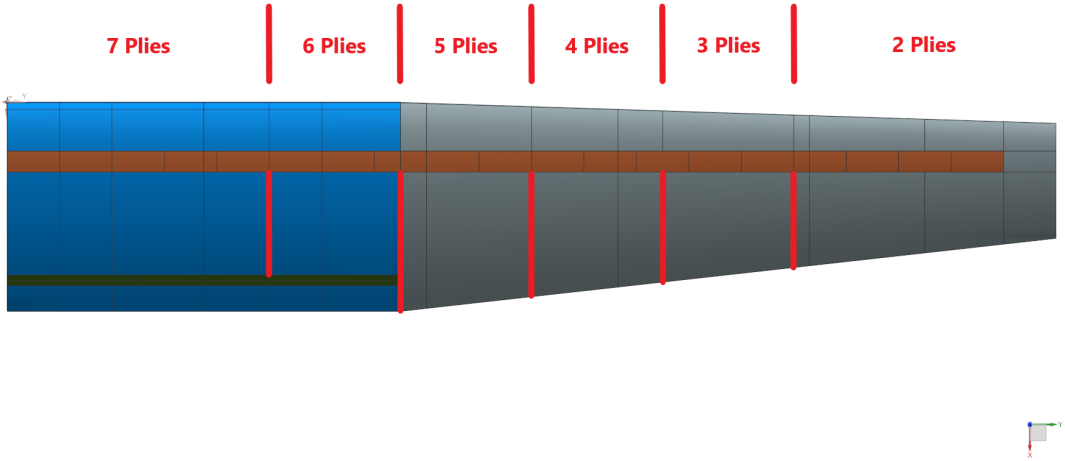

Figure 4.27: Light design - plies distribution along the span-wise.

Table 4.35: Light design - lay-up scheme.

Number of Plies	7	6	5	4	3	2
y-axis Position [mm]	0 - 500	500 - 750	750 - 1000	1000 - 1250	1250 - 1500	1500 - 2000

Figure 4.28 presents the static deformation of the light design wing in a side view. Deformations are presented in the same way as was for the spar in the previous section.

Figure 4.28: Wing's light design linear static analysis response. Deformation at 1:1 scale.

The first five buckling modes occurred in different places on the upper side of the wing. Figure 4.29 presents the buckling mode 1 deformation on the main spar's top cap close to rib 5. Following buckling modes occurred also in the main spar's top cap and on the secondary spar top cap close to the constraint. Adding that the wing's skin between both spars and ribs 2 and 3 is also a critical zone for

buckling to occur.

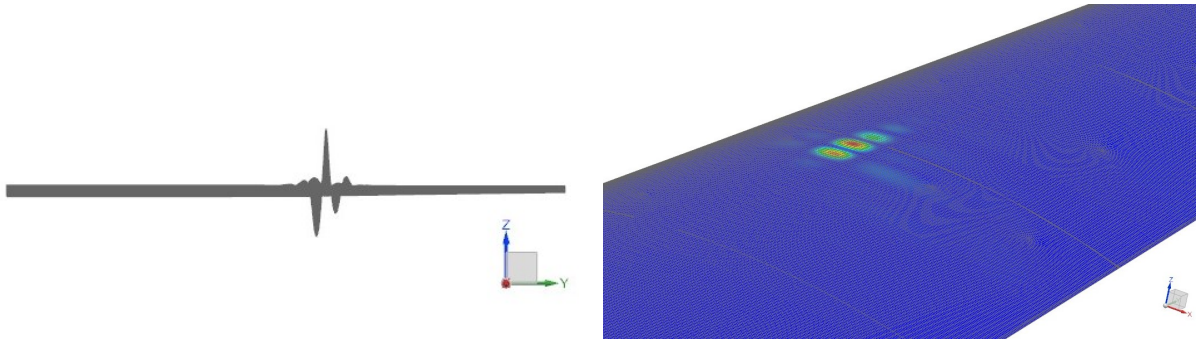

(a) 2D side view. Deformation at 10% model.

(b) 3D perspective view. Deformation at 1:1 Scale.

Figure 4.29: Wing's light design linear buckling analysis mode 1 response.

Taking into account the values presented in Table 4.28, the structural weight is estimated to reduce 43.3 g. Besides that, the manufacturing cost of the wing is also reduced because it requires less resin and fibers. Displacement and relative buckling load results for this design are presented in the next section, where it is compared with the previous four designs.

4.3.7 Results Comparison and Discussion

The final following tables present the main results for the buckling (resin 1, 2, and 3), resin mix, and light designs. The resin mix and light design comparative values are relative to the buckling design with resin 3 values while buckling design with resin 2 and 3 are compared with the same design with resin 1.

Table 4.36 summarizes the maximum wing displacement. Despite having increased 1.2%, the light design relative displacement percentage to the wingspan was kept the same as the one from the resin 3 model.

Table 4.36: Wing's displacement comparison.

Model	Displacement [mm]	Difference [%]	Wingspan [%]
Resin 1	112.1	-	5.6
Resin 2	108.2	-3.5	5.4
Resin 3	105.3	-6.1	5.3
Mix	105.3	0.0	5.3
Light	106.6	1.2	5.3

In general, the light design model's stress results were the lowest of all five. Revisiting appendix B to analyse the most critical structures in terms of stress from Section 4.3.4, the main spar had its stresses reduced by less than 1%. The top cap was an exception, where point B decreased by 7.1% and 3.0% for bidirectional and unidirectional CF plies, respectively, while point A had its stress increase by approximately 2% for both plies. The skin had its maximum stress value reduced by 0.8%, while the leading edge from both sides of the skin and the maximum value between spars from the bottom side

increased by a maximum of 0.9%. The trailing edge values decreased by 4.4% and 2.1% on the top and bottom sides, respectively.

Table 4.37 presents the critical relative buckling load and their differences. For the critical buckling load, it was possible to reduce it by 6.4% on the last model. Yet it was not possible to achieve a value closer to one to make it similar to the value from resin 1.

Table 4.37: Wing's relative buckling loads comparison.

	Mode 1	
Model	**Critical Buckling Load Factor**	**Difference [%]**
Resin 1	1.014	-
Resin 2	1.083	6.8
Resin 3	1.126	11.1
Mix	1.125	-0.1
Light	1.054	-6.4

To conclude, the light model is to be chosen as the final UAV wing model. It uses both resins in order to reduce weight and cost. The reduced number of plies from this model also allowed for a small weight decrease, considering it was only derived from changing the epoxy matrix, from resin 1 to resin 3, in almost all the structure.

The final wing design is comprised of:

- main and secondary spars made of resin 3 with the configuration described in Tables 4.29 and 4.30, respectively;
- leading and trailing edges, and a bottom side skin panel with a monolithic resin 3 laminate of bidirectional carbon fiber plies at 45º with a drop-off scheme as depicted in Table 4.23;
- a top side skin panel between spars with a monolithic resin 3 laminate of bidirectional carbon fiber plies at 45º with a drop-off scheme as depicted in Table 4.35;
- the original ribs made of resin 1 (see Table 4.6).

Chapter 5

Conclusions

5.1 Overview

This thesis aimed to achieve two main objectives. The first was to characterize laminated composite materials made of three distinct matrices, through experimental tensile and flexural tests, in order to evaluate the impact of graphene on the mechanical properties of laminates. The second was to analyse the impact of graphene on the mechanical performance of two aeronautical structures by applying the properties obtained in the first part. The aeronautical structures were subject to static and buckling analyses and structural modifications were applied to meet the design requirements determined by standards.

Carbon fibers were the only common component in the laminated composite materials. The aim of the comparison study stood around the epoxy matrices which were different. Graphene nanoplatelets at a 2 wt% were incorporated in HexaMatrix produced by Graphenest S.A.. The other two were neat HexaMatrix and Sicomin SR 8200 with hardener SD 7206, currently used by CIAFA.

The experimental part of the work revealed the importance of composite laminate production on its mechanical properties. The amount of matrix applied to the fibers led to production issues. Some specimens made of different epoxy matrices had scattered fiber/matrix relative volume percentages, which means that values were not precise. The limited experience of the producer proved to have a major impact on the specimens' quality and test performance. The unidirectional carbon fiber's flexural panels stand out as one of the compromised groups of specimens in which flexural tests should have been repeated. A 10.5% decrease in the matrix volume ratio, from resin 1 to resin 2, led to a 43.2% decrease in the flexural modulus.

In the numerical simulation, the mechanical properties obtained in tensile and bending tests were complemented with mechanical properties values from previous tests of similar materials and from literature (Silva, 2017).

As a starting point for the numerical simulation, it was used the wing structure design obtained by Sá (2021), as the baseline design. Linear static and linear buckling analyses were first performed on the wing's main spar to verify if design requirements were met. Due to the low number of plies on the

top cap, the structure was stiffened in order not to buckle. The same analyses were made to the wing structure, which led to modifications in the spar's webs and on the skin panels. It was necessary to increase the stiffness of the structural components to guarantee that buckle deformation did not occur for the design load factor.

Several modifications were also performed in order to decrease the weight of the structure. The original secondary spar's web, which was composed of a sandwich foam core and stood in between two bidirectional carbon laminates, was replaced by a bidirectional carbon fiber laminate at 45^{o} with four plies. It was also tested the implementation of a foam core skin panel and a unidirectional tape underneath the original skin panel to reduce buckling phenomena. It was proved that the drop-off layer scheme, also used in the main spar's caps, was the best option to increase the critical relative buckling load factor and reduce the structure's weight.

The static analysis showed stress singularities at the spars' constraints, and at the main spar's caps side edges close to the drop-off regions. The skin panel also presented singularities close to the main spar constraint. It was used a quadratic regression method, using converged values in the vicinity of the singularity to compute the approximate real stress at the singularity.

Stress discontinuities were found in the main spar's caps drop-offs. The cause of these required further investigation, which was not possible to perform during the available time for this project.

To take advantage of the graphene properties, two different wing structures were designed. The first was called the resin mix design, which mixed components manufactured using both resin 1 and 3. The choice of where to apply each resin was based on stress performance. The second was built upon the resin mix design and sought a decrease in the wing weight by decreasing the number of plies used in the top side skin panel while fulfilling static and buckling requirements. It was considered the final wing model design of this thesis.

5.2 Achievements

This thesis proved that a small concentration of graphene on the epoxy matrix will lead to a significant difference on the wing's displacement and stresses.

The experimental tests showed that graphene did not affect the specimen's tensile properties, since the results differences between the 3 resins for the two types of fibers were not significant.

As for the flexural modulus, bidirectional specimens presented a 3.3% increase between resin 1 and 2. For the graphene resin, this property improved by 6.2%. Due to the unidirectional issues above mentioned, their variations were tremendous when compared to the bidirectional specimens. These results were not coherent with the bidirectional ones, thus being eliminated from this study. Mechanical properties for the defective unidirectional specimens were estimated by having the same variations between matrices of bidirectional specimens. These were the ones mentioned at the beginning of the paragraph.

According to the classical laminate theory, since the specimen's stacking is equal for each test specimen and all the plies are oriented at zero degrees, Young's modulus is the same value as the flexural modulus, for each material. Thereby, it was considered to use the flexural modulus of the material as the

Young's modulus, since the loads to be applied on the wing structures are mainly of the bending type.

The numerical analysis showed even more significant differences between resin 1 and 3 compared to the ones from the experimental phase.

The use of HexaMatrix in the design of the main spar in spite of epoxy system SR8200 with hardener SD7206 allowed the following improvements:

- displacement decrease of 7.8%;
- critical buckling load increase of 9.8%;
- stress decrease between 2.1% and 14.0%.

The wing model presented similar improvements to the main spar when comparing the same two epoxy systems:

- displacement decrease of 6.1%;
- critical buckling load increase of 11.1%;
- stress decrease in most of the wing parts between 0.6% (rib 2 leading edge) and 6.2% (top side leading edge skin panel adjacent to the main spar).

An exception occurred for the trailing edge ribs, which had an increase of 1.8% for the bidirectional carbon fibers to 6.9% for the unidirectional. Maximum stress occurred at the main spar's top cap element close to the root and to the skin panel that is in between both spars.

The final light design model had some plies removed in order to get a lighter structure while fulfilling the buckling criteria. A trade-off between the displacement increase and the weight and buckling load decrease was analysed to guarantee that design safety requirements continued to be fulfilled. Stress could also vary, either by increasing or decreasing at different points of the wing structure.

Comparing results from the light design with the ones from the resin 3 buckling design, there was a:

- displacement increase of 1.2%;
- weight decrease of 43.3 g.
- critical buckling load decrease of 6.4%;
- stress decrease in most of the wing parts with the maximum difference being 7.1%, registered at the stress singularity of the main spar's top cap.
- stress increase in a few of the wing regions that had their values approximated to the ones from the resin 1 model, never exceeding the material's ultimate strength.

The trade-off between the displacement increase and the weight, buckling load, and stress decrease turned out to be positive since displacement was kept almost the same from the resin 3 buckling design, which were both 5.3% of the wingspan. The light model was chosen as the final UAV wing model since it uses both resins in order to reduce weight and costs.

5.3 Future Work

During the course of this dissertation, several additional analyses and methods could have been performed.

One suggestion would be to experimentally obtain the in-plane shear modulus (G_{12}) by the $\pm 45^{o}$ tension test method specified in ISO 14129:1997 (1997). The study of this mechanical property would have been of great interest since bidirectional carbon fiber laminates have this stacking on both structures. In order to overcome this situation, the necessary remaining data was obtained from Silva (2017).

Another suggestion is to include extensometers or strain gauges in both tensile and flexural tests to provide the true strain instead of the engineering strain and also to obtain the Poisson's ratio. Poisson's ratio is fundamental to characterizing orthotropic materials, thus it had to be obtained from the same bibliography.

It would be interesting to check if a post-cure process of ten days at room temperature, as it was done for the Sicomin matrix, would achieve better mechanical properties for HexaMatrix. SR8200 plus SD 7206 technical datasheet states that the matrix can achieve better mechanical results for these production conditions, compared to short time post-cure processes in an oven, and therefore the same should be studied for HexaMatrix.

Regarding the numerical part, a stress discontinuity study should be performed around the laminate's layer drop-off region. Simpler structures with simpler applied loads should be first analysed to infer conclusions on the spar and wing analyses. Mortensen and Thomsen (1998) suggest that computing layer drop-offs with 3D solid elements can be beneficial, leading to a decrease in the necessary layers composing the structure. Still, solid element's application on the wing model could lead to new obstacles in FEM implementations and increased computational times, thus it should be done only using simpler laminate design models.

To improve the FEM analysis results, it is recommended to perform nonlinear static and buckling analyses. Despite obtained displacements from linear analyses not showing considerable magnitudes, it is one of the recommendations made by Skotny (2022) and Acín (2022) to overcome the stress singularities effects.

The model has only been tested for the positive ultimate limit load factor, which led to higher stiffness differences between the upper and the lower parts of the structures. After the performed analyses, both the final spar and wing model should be tested for the negative ultimate limit load factor, followed by the necessary structural modifications.

Finally, it is suggested to manufacture and test one major component from the wing structure design, as per example the main spar. Using the specifications mentioned in Section 4.2.3, three equivalent structural components should be manufactured using the epoxy systems considered in this thesis. The main goal is to experimentally compare the three matrix systems' performance when applied in a structure subjected to the same forces used in the numerical analysis. At the same time, this study could be used to validate the method applied for linear static and linear buckling analyses in this work.

Bibliography

Acín, M. (2022). *Stress singularities and concentrations - mesh convergence in fea.* Retrieved from https://www.linkedin.com/pulse/stress-singularities-concentrations-mesh-fea-marcos-ac%C3%ADn-gonz%C3%A1lez

Aerospace Technology Institute, & The University of Manchester. (2018). Graphene exploitation material applications in aerospace. *INSIGHT papers*(Issue 6).

Airbus. (n.d.). *Technology leaders (1977-1979).* Retrieved from https://www.airbus.com/en/who-we-are/our-history/commercial-aircraft-history/technology-leaders-1977-1979

Allen, M. J., Tung, V. C., & Kaner, R. B. (2010). Honeycomb carbon: A review of graphene. *Chemical Reviews*, *110*(1), 132-145. Retrieved from https://doi.org/10.1021/cr900070d doi: 10.1021/cr900070d

Allied Engineering Publication, N. (2014). *Light unmanned aircraft systems airworthiness requirements - STANAG 4703 - AEP-83.* Retrieved from https://assets.publishing.service.gov.uk/government/uploads/system/uploads/attachment_data/file/391827/20140916-STANAG-4703_AEP-83_A__1_.pdf (NATO Unclassified)

Alves, B., Coelho, V., Silva, P., Marta, A., Afonso, F., Sá, P., & Caetano, J. (2021). Design of a hydrogen powered small electric fixed-wing uav with vtol capability. In *International conference on multidisciplinary design optimization of aerospace systems* (pp. 290–304).

Boehm, H., Setton, R., & Stumpp, E. (1986). Nomenclature and terminology of graphite intercalation compounds. *Carbon*, *24*(2), 241-245. Retrieved from https://www.sciencedirect.com/science/article/pii/0008622386901260 doi: https://doi.org/10.1016/0008-6223(86)90126-0

Brandon. (2020). *True stress-strain vs engineering stress-strain.* Retrieved from https://msestudent.com/true-stress-strain-vs-engineering-stress-strain/

Britannica, T. E. o. E. (2021). *Hall effect. encyclopedia britannica.* Retrieved from https://www.britannica.com/science/Hall-effect

Composite materials in the airbus. (1989). *Aircraft Engineering and Aerospace Technology*, *61*(12), 20–29. doi: 10.1108/eb036877

Cooper, D., D'Anjou, B., Ghattamaneni, N., Harack, B., Hilke, M., Horth, A., ... Yu, V. (2011). Experimental review of graphene. *ISRN Condens. Matter Phys.*, *2012*. doi: 10.5402/2012/501686

Coraux, J., N'Diaye, A., Busse, C., & Michely, T. (2011). 10 - epitaxial growth of graphene thin films on single crystal metal surfaces. In Z. Cao (Ed.), *Thin film growth* (p. 228-255).

Woodhead Publishing. Retrieved from https://www.sciencedirect.com/science/article/pii/B9781845697365500104 doi: https://doi.org/10.1533/9780857093295.2.228

Dorworth, L. C., Gardiner, G. L., & Mellema, G. M. (2009). *Essentials of advanced composite fabrication & repair, washington: Aviation supplies & academics.* Inc.

Dreyer, D. R., Park, S., Bielawski, C. W., & Ruoff, R. S. (2010). The chemistry of graphene oxide. *Chem. Soc. Rev.*, *39*, 228-240. Retrieved from http://dx.doi.org/10.1039/B917103G doi: 10.1039/B917103G

Femto Engineering. (2022). *In short explained: Linear and nonlinear structural analysis.* Retrieved from https://www.femto.eu/stories/linear-non-linear-analysis-explained/

Flynn, D. G. (2010). *The quantum hall effect in graphene*. Retrieved from http://www.physics.drexel.edu/~bob/TermPapers/Flynn_QuantumPaper.pdf

Fraga, T. J., Sobrinho, M. A. d. M., Carvalho, M. N., & Ghislandi, M. G. (2020). State of the art: Synthesis and characterization of functionalized graphene nanomaterials. *Nano Express*, *1*(2), 022002. doi: 10.1088/2632-959x/abb921

Geim, A. K. (2012). Graphene prehistory. *Physica Scripta*, *T146*, 014003. Retrieved from https://doi.org/10.1088/0031-8949/2012/t146/014003 doi: 10.1088/0031-8949/2012/t146/014003

Gulgunje, P. V., Newcomb, B. A., Gupta, K., Chae, H. G., Tsotsis, T. K., & Kumar, S. (2015). Low-density and high-modulus carbon fibers from polyacrylonitrile with honeycomb structure. *Carbon*, *95*, 710-714. Retrieved from https://www.sciencedirect.com/science/article/pii/S0008622315302001 doi: https://doi.org/10.1016/j.carbon.2015.08.097

Herakovich, C. T. (1998). *Mechanics of fibrous composites*. John Wiley & Sons.

Hollmann, M. (2003). *Composite aircraft design* (5th ed.). Aircraft Designs, INC.

International Organization for Standardization. (1997). Iso 14129:1997 - fibre-reinforced plastic composites — determination of the in-plane shear stress/shear strain response, including the in-plane shear modulus and strength, by the plus or minus 45 degree tension test method [Computer software manual].

International Organization for Standardization. (2011). Iso 14125:1998 + ac:2002 + a1:2011 - fibre-reinforced plastic composites — determination of flexural properties [Computer software manual].

International Organization for Standardization. (2017). ISO/TS 80004-13:2017(en) Nanotechnologies — Vocabulary — Part 13: Graphene and related two-dimensional (2D) materials. *Online Browsing Platform (OBP) - ISO*. Retrieved from https://www.iso.org/obp/ui/#iso:std:iso:ts:80004:-13:ed-1:v1:en

International Organization for Standardization. (2019). Iso 527-1 - plastics - determination of tensile properties - part 1: General principles [Computer software manual].

International Organization for Standardization. (2020a). Iso/dis 527-4 - plastics - determination of tensile properties - part 4: Test conditions for isotropic and orthotropic fibre-reinforced plastic composites [Computer software manual].

International Organization for Standardization. (2020b). Iso/dis 527-5 - plastics - determination of tensile properties - part 5: Test conditions for unidirectional fibre-reinforced plastic composites [Computer

software manual].

Iowa State University - Center for Nondestructive Evaluation. (n.d.). *Fracture toughness.* Iowa State University. Retrieved from https://www.nde-ed.org/Physics/Materials/Mechanical/FractureToughness.xhtml

Katti, P., Verma, K. K., Kumar, S., & Bose, S. (2021). Tuning the interface in epoxy-based composites and laminates through epoxy grafted graphene oxide enhances mechanical properties. *Nanoscale Adv.*, *3*, 6739-6749. Retrieved from http://dx.doi.org/10.1039/D1NA00437A doi: 10.1039/D1NA00437A

Kumar, N., Salehiyan, R., Chauke, V., Joseph Botlhoko, O., Setshedi, K., Scriba, M., ... Sinha Ray, S. (2021). Top-down synthesis of graphene: A comprehensive review. *FlatChem*, *27*, 100224. Retrieved from https://www.sciencedirect.com/science/article/pii/S2452262721000039 doi: https://doi.org/10.1016/j.flatc.2021.100224

Kumar, V., Kumar, A., Lee, D.-J., & Park, S.-S. (2021). Estimation of number of graphene layers using different methods: A focused review. *Materials*, *14*(16). Retrieved from https://www.mdpi.com/1996-1944/14/16/4590 doi: https://doi.org/10.3390/ma14164590

Kurkjian, C. R., Biswas, D. R., & Yuce, H. H. (1996). Intrinsic strength of light guide fibers. In H. H. Yuce, D. K. Paul, & R. A. Greenwell (Eds.), *Optical network engineering and integrity* (Vol. 2611, pp. 56 – 63). SPIE. Retrieved from https://doi.org/10.1117/12.230124 doi: 10.1117/12.230124

Lee, C., Wei, X., Kysar, J. W., & Hone, J. (2008). Measurement of the elastic properties and intrinsic strength of monolayer graphene. *Science*, *321*(5887), 385-388. Retrieved from https://www.science.org/doi/abs/10.1126/science.1157996 doi: 10.1126/science.1157996

Li, Z., Young, R. J., Backes, C., Zhao, W., Zhang, X., Zhukov, A. A., ... Coleman, J. N. (2020). Mechanisms of liquid-phase exfoliation for the production of graphene. *ACS Nano*, *14*(9), 10976-10985. Retrieved from https://doi.org/10.1021/acsnano.0c03916 doi: 10.1021/acsnano.0c03916

Martin-Gallego, M., Bernal, M., Hernandez, M., Verdejo, R., & Lopez-Manchado, M. (2013). Comparison of filler percolation and mechanical properties in graphene and carbon nanotubes filled epoxy nanocomposites. *European Polymer Journal*, *49*(6), 1347-1353. Retrieved from https://www.sciencedirect.com/science/article/pii/S0014305713001110 doi: https://doi.org/10.1016/j.eurpolymj.2013.02.033

Mortensen, F., & Thomsen, O. T. (1998). 1 layer drop-off. In *Theoretical background of esacomp analyses - part iv laminate discontinuities.* Retrieved from https://altairuniversity.com/wp-content/uploads/2018/06/4-Laminate-Discontinuities.pdf

Nair, R. R., Blake, P., Grigorenko, A. N., Novoselov, K. S., Booth, T. J., Stauber, T., ... Geim, A. K. (2008). Fine structure constant defines visual transparency of graphene. *Science*, *320*(5881), 1308-1308. Retrieved from https://www.science.org/doi/abs/10.1126/science.1156965 doi: 10.1126/science.1156965

Papageorgiou, D. G., Kinloch, I. A., & Young, R. J. (2017). Mechanical properties of graphene and graphene-based nanocomposites. *Progress in Materials Science*, *90*, 75-127. Retrieved from https://www.sciencedirect.com/science/article/pii/S0079642517300968 doi: https://doi

.org/10.1016/j.pmatsci.2017.07.004

Parente, J., Simões, R., & Reis, P. (2022). Effect of graphene nanoparticles on suspension viscosity and mechanical properties of epoxy-based nanocomposites. *Procedia Structural Integrity*, *37*, 820-825. Retrieved from https://www.sciencedirect.com/science/article/pii/S2452321622001706 (ICSI 2021 The 4th International Conference on Structural Integrity) doi: https://doi.org/10.1016/j.prostr.2022.02.014

Rafiee, M., Nitzsche, F., Laliberte, J., Thibault, J., & Labrosse, M. R. (2019). Simultaneous reinforcement of matrix and fibers for enhancement of mechanical properties of graphene-modified laminated composites. *Polymer Composites*, *40*(S2), E1732-E1745. Retrieved from https://onlinelibrary.wiley.com/doi/abs/10.1002/pc.25137 doi: https://doi.org/10.1002/pc.25137

Rafiee, M. A., Rafiee, J., Wang, Z., Song, H., Yu, Z.-Z., & Koratkar, N. (2009). Enhanced mechanical properties of nanocomposites at low graphene content. *ACS Nano*, *3*(12), 3884-3890. Retrieved from https://doi.org/10.1021/nn9010472 doi: 10.1021/nn9010472

Reddy, J. N. (2004). *Mechanics of laminated composite plates and shells: Theory and analysis*. CRC Press.

Reddy, J. N. (2006). *An introduction to the finite element method* (3rd ed.). McGraw-Hill.

Sá, P. (2021). *Projeto estrutural de um veículo aéreo não tripulado com uma célula de combustível de hidrogénio* (Unpublished master's thesis). Academia da Força Aérea.

Samuel, A. E., & Weir, J. (1999). *Introduction to engineering design*. Butterworth-Heinemann.

Shokrieh, M., & Kondori, M. S. (2020). Effects of adding graphene nanoparticles in decreasing of residual stresses of carbon/epoxy laminated composites. *Compos. Mater. Eng*, *2*(1), 53–64.

Siemens. (2019). Simcenter nastran element library reference [Computer software manual]. Retrieved from https://docs.plm.automation.siemens.com/data_services/resources/scnastran/2020_1/help/tdoc/en_US/pdf/element.pdf

Silva, J. (2017). *Design and optimization of a wing structure for a uas class i 145 kg* (Unpublished master's thesis). Portuguese Air Force Academy.

Simitses, G. J., & Hodges, D. H. (2005). *Fundamentals of structural stability*. Elsevier.

Singh, V., Joung, D., Zhai, L., Das, S., Khondaker, S. I., & Seal, S. (2011). Graphene based materials: Past, present and future. *Progress in Materials Science*, *56*(8), 1178-1271. Retrieved from https://www.sciencedirect.com/science/article/pii/S0079642511000442 doi: https://doi.org/10.1016/j.pmatsci.2011.03.003

Skotny, L. (2022). *Stress singularity - an honest discussion.* Retrieved from https://enterfea.com/stress-singularity-an-honest-discussion/

Swolfs, Y., Meerten, Y., Hine, P., Ward, I., Verpoest, I., & Gorbatikh, L. (2015). Introducing ductility in hybrid carbon fibre/self-reinforced composites through control of the damage mechanisms. *Composite Structures*, *131*, 259-265. Retrieved from https://www.sciencedirect.com/science/article/pii/S026382231500375X doi: https://doi.org/10.1016/j.compstruct.2015.04.069

Tang, J., Zhou, H., Liang, Y., Shi, X., Yang, X., & Zhang, J. (2014). Properties of graphene oxide/epoxy resin composites. *J. Nanomaterials*, *2014*. Retrieved from https://doi.org/10.1155/2014/

696859 doi: 10.1155/2014/696859

The Graphene Council. (n.d.). *What is graphene?* Retrieved from https://www.thegraphenecouncil.org/page/WhatIsGraphene

This Month in Physics History: October 22, 2004: Discovery of Graphene. (2009). *APS NEWS*, *18*(9), 2.

Tomblin, J. S., Ng, Y. C., & Raju, K. S. (2003). Material qualification and equivalency for polymer matrix composite material systems: Updated procedure [Computer software manual]. Office of Aviation Research Washington, D.C. 20591.

Toray Composite Materials America, I. (2018). T700g standard modulus carbon fiber (5th ed.) [Computer software manual].

Wallenberger, F. T., & Bingham, P. A. (2010). *Fiberglass and glass technology: Energy-friendly compositions and applications*. Springer.

Xu, Y., Zhu, J., Wu, Z., Cao, Y., Zhao, Y., & Zhang, W. (2018). A review on the design of laminated composite structures: constant and variable stiffness design and topology optimization. *Advanced Composites and Hybrid Materials*, *1*(3), 460–477. Retrieved from https://doi.org/10.1007/s42114-018-0032-7 doi: 10.1007/s42114-018-0032-7

Zhang, P., Ma, L., Fan, F., Zeng, Z., Peng, C., Loya, P. E., ... et al. (2014). *Fracture toughness of graphene* (Vol. 5) (No. 1). Springer Science and Business Media LLC. Retrieved from http://dx.doi.org/10.1038/ncomms4782 doi: 10.1038/ncomms4782

Zhang, Z., Fraser, A., Ye, S., Merle, G., & Barralet, J. (2019). Top-down bottom-up graphene synthesis. *Nano Futures*, *3*(4), 042003. Retrieved from https://dx.doi.org/10.1088/2399-1984/ab4eff doi: 10.1088/2399-1984/ab4eff

Appendix A

Specimens' Mechanical Properties

Young's or flexural modulus, the peak loads and stresses, and the strain at break of each tested specimen will be presented in the following tables from this appendix. Values that were out of the Lower/Upper boundaries range are marked with an asterisk (*).

A.1 Tensile Properties

A.1.1 Bidirectional Specimens

Table A.1: Bidirectional tensile specimens - Resin 1

Specimen	E [GPa]	Peak Load [N]	Peak Stress [MPa]	Strain At Break [%]
A1	41.519*	31634.56	679.65	1.69
A2	39.570	32115.56	668.46	1.75
A3	38.649	26588.16	538.39*	1.48
A4	38.726	27594.56	562.88	1.51
A5	38.733	33199.30	685.05	1.86
B1	39.277	33578.70	696.43	1.88
B2	39.732	32661.07	699.52	1.89
B3	38.654	29685.39	622.70	1.69
B4	37.708	33488.91	697.97	1.98
B5	37.808	32728.29	678.26	1.92

Table A.2: Bidirectional tensile specimens - Resin 2

Specimen	E [GPa]	Peak Load [N]	Peak Stress [MPa]	Strain At Break [%]
D1	40.378	26295.42	576.37	1.49
D2	39.490	28747.16	627.73	1.68
D3	39.823	27766.67	608.73	1.61
D4	39.953	27911.08	609.18	1.60
D5	40.343	28475.62	646.40	1.69
E1	39.056	33080.85	711.80	1.96
E2	38.061	34064.22	724.40	2.05
E3	37.569	33583.91	699.72	2.02
E4	37.420	32960.84	687.34	1.95
E5	36.963	32527.86	671.39	1.93

Table A.3: Bidirectional tensile specimens - Resin 3

Specimen	E [GPa]	Peak Load [N]	Peak Stress [MPa]	Strain At Break [%]
G1	39.261*	31882.51	680.82	1.86
G2	38.425	29596.57	631.88	1.75
G3	38.346	31278.48	663.48	1.84
G4	38.996	31904.72	684.39	1.91
G5	38.572	29922.55	643.34	1.77
H1	38.606	30309.56	661.03	1.85
H2	38.074	29536.16	648.67	1.82
H3	38.649	31169.60	693.52	1.93
H4	38.712	26467.50*	579.23*	1.57*
H5	38.376	30996.09	685.34	1.91

A.1.2 Unidirectional Specimens

Table A.4: Unidirectional tensile specimens - Resin 1

Specimen	E [GPa]	Peak Load [N]	Peak Stress [MPa]	Strain At Break [%]
A1	84.675	24724.73	1717.31	2.16
A2	82.393	24288.96	1677.23	2.16
A3	83.772	23652.60	1667.40	2.11
B1	86.993	21943.37	1552.83	1.90
B2	85.019	21815.61	1549.87	2.04
B3	84.136	21651.63	1514.43	1.91
C1	81.677	23900.81	1668.02	2.16
C2	80.646	23230.40	1624.62	2.11
C3	51.882*	15316.93*	1070.20*	12.60*

Table A.5: Unidirectional tensile specimens - Resin 2

Specimen	E [GPa]	Peak Load [N]	Peak Stress [MPa]	Strain At Break [%]
D1	80.251	19055.23	1358.63	1.80
D2	80.476	19509.40	1389.08	1.91
D3	81.058	18348.43	1300.66	1.85
E1	87.190	17050.45	1373.52	1.87
E2	-	-	-	-
E3	88.380	13401.41*	1291.98	1.83
F1	85.522	20488.49	1453.50	1.91
F2	83.714	18822.12	1428.53	1.85
F3	88.282	18013.19	1487.30	1.80

Table A.6: Unidirectional tensile specimens - Resin 3

Specimen	E [GPa]	Peak Load [N]	Peak Stress [MPa]	Strain At Break [%]
G1	81.066	21517.68	1474.43	2.02
G2	80.274	21744.73	1452.65	2.06*
G3	84.673	21257.86	1476.85	1.90
H1	80.540	19069.31	1282.14	1.90
H2	80.807	20180.89	1382.89	1.81
H3	80.252	18945.38	1315.17	1.82
I1	83.910	18987.79	1359.89	1.80
I2	83.197	17592.38	1271.31	1.82
I3	83.372	15839.48	1172.39	1.76

A.2 Flexural Properties

A.2.1 Bidirectional Specimens

Table A.7: Bidirectional flexural specimens - Resin 1

Specimen	E_f [GPa]	Peak Load [N]	Peak Stress [MPa]	Strain At Break [%]
A1	35.911	257.61	662.51	1.42
A2	33.069	253.25	687.56	1.40
A3	33.482	241.80	636.29	1.34
A4	33.204	247.65	655.28	1.40
A5	32.766	248.89	666.55	1.41
B1	36.510	262.00	657.84	1.43
B2	39.063	266.32	646.88	1.42
B3	40.152	281.65	668.50	1.47
B4	38.070	270.45	646.58	1.44
B5	36.642	295.09	720.15	1.63

Table A.8: Bidirectional flexural specimens - Resin 2

Specimen	E_f [GPa]	Peak Load [N]	Peak Stress [MPa]	Strain At Break [%]
D1	35.953	234.14	587.72	1.27
D2	36.151	270.70	660.25	1.47
D3	37.279	253.40	615.04	1.41
D4	38.467	276.75	672.69	1.43
D5	35.867	269.83	678.41	1.45
E1	38.532	288.09	686.19	1.58
E2	38.163	272.63	651.66	1.43
E3	37.334	278.94	671.68	1.49
E4	35.865	271.70	672.74	1.51
E5	35.572	280.49	719.03	1.53

Table A.9: Bidirectional flexural specimens - Resin 3

Specimen	E_f [GPa]	Peak Load [N]	Peak Stress [MPa]	Strain At Break [%]
G1	35.033	256.90	635.12	1.44
G2	39.230	276.22	659.04	1.49
G3	41.080	292.14	692.29	1.44
G4	40.174	281.26	678.63	1.41
G5	37.457	278.16	676.21	1.55
H1	35.970	251.73	627.11	1.39
H2	39.990	263.66	609.87	1.42
H3	39.113	263.93	618.14	1.46
H4	37.127	265.74	642.01	1.45
H5	36.067	248.60	615.19	1.34

A.2.2 Unidirectional Specimens

Table A.10: Unidirectional flexural specimens - Resin 1

Specimen	E_f [GPa]	Peak Load [N]	Peak Stress [MPa]	Strain At Break [%]
A1	86.814	465.89	1064.67	1.90
A2	90.884	449.31	935.34	2.98
A3	97.027	476.09	1029.33	2.11
B1	93.800	445.54	906.79	2.12
B2	80.886	393.89	822.50	2.52
B3	86.449	428.70	892.25	1.99
C1	89.292	426.19	932.61	2.30
C2	78.806	401.38	828.40	2.38
C3	82.910	435.16	927.00	2.39

Table A.11: Unidirectional flexural specimens - Resin 2

Specimen	E_f [GPa]	Peak Load [N]	Peak Stress [MPa]	Strain At Break [%]
D1	57.479	284.70	730.88	3.38
D2	53.679	259.64	641.44	2.91
D3	55.684	274.25	705.57	2.85
E1	46.740	231.12	685.90	2.32
E2	37.700	202.11	630.01	2.69
E3	47.382	229.13	647.00	2.50
F1	35.654	235.27	648.16	2.92
F2	54.213	271.12	737.46	2.93
F3	58.566	273.72	735.43	2.97

Table A.12: Unidirectional flexural specimens - Resin 3

Specimen	E_f [GPa]	Peak Load [N]	Peak Stress [MPa]	Strain At Break [%]
G1	68.315	355.19	795.04	2.18
G2	83.863	422.46	907.23	2.27
G3	61.529	330.91	746.88	2.17
H1	71.446	351.73	779.15	2.34
H2	81.347	395.27	864.83	2.29
H3	73.865	363.26	828.58	2.15
I1	42.650	220.44	592.11	2.98
I2	49.082	252.55	647.93	2.40
I3	48.916	248.72	633.79	2.90

Appendix B

Wing Designs' Stresses

Stresses at both spar's constraint and the maximum stresses from both sides of the skin and the second rib will be presented in the following tables from this appendix. The buckling design made of each of the three resins, the resin mix, and the light models' stress values will be presented along with their percentage difference relative to resin 1, for the second and third models, and relative to resin 3 for the fourth and fifth.

B.1 Main Spar Stresses

Table B.1: Main spar top cap plies 1 and 3 stresses.

	Ply 1 (Bidirectional CF)					
	Point A		**Point B**		**Point C**	
Model	σ_{WP} **[MPa]**	**Difference [%]**	σ_{WP} **[MPa]**	**Difference [%]**	σ_{WP} **[MPa]**	**Difference [%]**
Resin 1	-65.03	-	-141.51	-	-53.83	-
Resin 2	-63.81	-1.9	-138.67	-2.0	-52.73	-2.0
Resin 3	-63.21	-2.8	-137.21	-3.0	-52.17	-3.1
Mix	-63.24	0.0	-137.92	0.5	-52.20	0.0
Light	-64.67	2.3	-127.45	-7.1	-53.26	2.1

	Ply 3 (Unidirectional CF)					
	Point A		**Point B**		**Point C**	
Model	σ_{WP} **[MPa]**	**Difference [%]**	σ_{WP} **[MPa]**	**Difference [%]**	σ_{WP} **[MPa]**	**Difference [%]**
Resin 1	-237.08	-	-431.22	-	-191.46	-
Resin 2	-234.34	-1.2	-423.80	-1.7	-188.75	-1.4
Resin 3	-234.22	-1.2	-420.78	-2.4	-188.07	-1.8
Mix	-234.36	0.1	-420.63	-0.0	-188.17	0.0
Light	-239.17	2.1	-407.95	-3.0	-191.57	1.8

Table B.2: Main spar bottom cap plies 1 and 3 stresses.

	Ply 1 (Bidirectional CF)					
	Point A		Point B		Point C	
Model	σ_{WP} [Mpa]	Difference [%]	σ_{WP} [Mpa]	Difference [%]	σ_{WP} [Mpa]	Difference [%]
Resin 1	100.03	-	90.82	-	65.69	-
Resin 2	98.16	-1.9	88.97	-2.0	64.87	-1.2
Resin 3	97.48	-2.6	87.96	-3.1	64.76	-1.4
Mix	97.49	0.0	88.24	0.3	64.86	0.1
Light	97.84	0.4	88.02	0.1	64.95	0.3

	Ply 3 (Unidirectional CF)					
	Point A		Point B		Point C	
Model	σ_{WP} [Mpa]	Difference [%]	σ_{WP} [Mpa]	Difference [%]	σ_{WP} [Mpa]	Difference [%]
Resin 1	361.04	-	274.15	-	195.47	-
Resin 2	354.60	-1.8	269.38	-1.7	192.70	-1.4
Resin 3	354.55	-1.8	267.06	-2.6	191.97	-1.8
Mix	354.68	0.0	267.08	0.0	192.14	0.1
Light	355.98	0.4	266.58	-0.2	192.49	0.3

Table B.3: Main spar back web plies 1 and 4 stresses.

	Ply 1 (Bidirectional CF)					
	Point A		Point B		Point C	
Model	σ_{WP} [Mpa]	Difference [%]	σ_{WP} [Mpa]	Difference [%]	σ_{WP} [Mpa]	Difference [%]
Resin 1	-95.36	-	65.25	-	-12.74	-
Resin 2	-92.74	-2.7	63.66	-2.4	-12.39	-2.8
Resin 3	-91.06	-4.5	62.54	-4.2	-12.19	-4.3
Mix	-90.92	-0.2	62.42	-0.2	-12.21	0.2
Light	-90.16	-1.0	62.09	-0.7	-11.68	-4.1

	Ply 4 (Bidirectional CF)					
	Point A		Point B		Point C	
Model	σ_{WP} [Mpa]	Difference [%]	σ_{WP} [Mpa]	Difference [%]	σ_{WP} [Mpa]	Difference [%]
Resin 1	-94.93	-	71.66	-	-8.20	-
Resin 2	-92.40	-2.7	70.18	-2.1	-7.83	-4.4
Resin 3	-90.73	-4.4	69.20	-3.4	-7.59	-7.5
Mix	-90.46	-0.3	69.05	-0.2	-7.58	-0.1
Light	-90.50	-0.3	68.78	-0.6	-7.44	-1.9

B.2 Secondary Spar Stresses

Table B.4: Secondary spar top cap plies 1 and 3 stresses.

	Ply 1 (Bidirectional CF)					
	Leading Edge Corner		Trailing Edge Corner		Center Point	
Model	σ_{WP} [Mpa]	Difference [%]	σ_{WP} [Mpa]	Difference [%]	σ_{WP} [Mpa]	Difference [%]
Resin 1	-112.11	-	-29.23	-	-43.93	-
Resin 2	-110.14	-1.8	-28.81	-1.4	-43.26	-1.5
Resin 3	-108.77	-3.0	-28.48	-2.6	-42.85	-2.5
Mix	-109.90	1.0	-28.83	1.3	-43.21	0.8
Light	-107.40	-1.2	-27.45	-3.6	-42.18	-1.6

	Ply 3 (Unidirectional CF)					
	Leading Edge Corner		Trailing Edge Corner		Center Point	
Model	σ_{WP} [Mpa]	Difference [%]	σ_{WP} [Mpa]	Difference [%]	σ_{WP} [Mpa]	Difference [%]
Resin 1	-276.60	-	-11.29	-	-105.06	-
Resin 2	-272.03	-1.6	-11.45	1.4	-103.34	-1.6
Resin 3	-270.00	-2.4	-11.43	1.2	-102.59	-2.3
Mix	-271.14	0.4	-11.54	0.9	-102.96	0.4
Light	-272.98	1.1	-15.47	35.3	-105.22	2.6

Table B.5: Secondary spar bottom cap plies 1 and 3 stresses.

	Ply 1 (Bidirectional CF)					
	Leading Edge Corner		Trailing Edge Corner		Center Point	
Model	σ_{WP} [Mpa]	Difference [%]	σ_{WP} [Mpa]	Difference [%]	σ_{WP} [Mpa]	Difference [%]
Resin 1	65.18	-	60.42	-	40.84	-
Resin 2	63.75	-2.2	58.90	-2.5	40.13	-1.7
Resin 3	62.75	-3.7	57.83	-4.3	39.81	-2.5
Mix	63.38	1.0	57.87	0.1	39.99	0.4
Light	63.42	1.1	56.78	-1.8	39.72	-0.2

	Ply 3 (Unidirectional CF)					
	Leading Edge Corner		Trailing Edge Corner		Center Point	
Model	σ_{WP} [Mpa]	Difference [%]	σ_{WP} [Mpa]	Difference [%]	σ_{WP} [Mpa]	Difference [%]
Resin 1	178.45	-	206.65	-	125.32	-
Resin 2	174.95	-2.0	203.15	-1.7	122.94	-1.9
Resin 3	172.93	-3.1	201.70	-2.4	121.73	-2.9
Mix	173.38	0.3	201.72	0.0	121.88	0.1
Light	171.60	-0.8	199.00	-1.3	120.41	-1.1

Table B.6: Secondary spar web plies 1 and 4 stresses.

	Ply 1 (Bidirectional CF)					
	Upper Corner		Lower Corner		Center Point	
Model	σ_{WP} [Mpa]	Difference [%]	σ_{WP} [Mpa]	Difference [%]	σ_{WP} [Mpa]	Difference [%]
Resin 1	-31.92	-	16.88	-	-10.10	-
Resin 2	-31.14	-2.4	16.43	-2.7	-9.96	-1.4
Resin 3	-30.60	-4.2	16.12	-4.5	-9.90	-2.0
Mix	-30.68	0.3	16.01	-0.7	-9.89	-0.1
Light	-30.32	-0.9	15.78	-2.1	-9.74	-1.5

	Ply 4 (Bidirectional CF)					
	Upper Corner		Lower Corner		Center Point	
Model	σ_{WP} [Mpa]	Difference [%]	σ_{WP} [Mpa]	Difference [%]	σ_{WP} [Mpa]	Difference [%]
Resin 1	-31.32	-	18.14	-	-9.41	-
Resin 2	-30.45	-2.8	17.72	-2.3	-9.18	-2.5
Resin 3	-29.79	-4.9	17.44	-3.8	-9.00	-4.4
Mix	-29.93	0.5	17.35	-0.6	-9.05	0.5
Light	-29.72	-0.2	17.11	-1.9	-9.06	0.7

B.3 Skin Maximum Stresses

Table B.7: Skin top and bottom side outer ply maximum stresses.

	Top Side - Ply 1 (Bidirectional CF)					
	Leading Edge		Between Spars		Trailing Edge	
Model	σ_{WP} [Mpa]	Difference [%]	σ_{WP} [Mpa]	Difference [%]	σ_{WP} [Mpa]	Difference [%]
Resin 1	-82.67	-	-199.85	-	-24.39	-
Resin 2	-79.82	-3.4	-194.88	-2.5	-23.85	-2.2
Resin 3	-77.56	-6.2	-191.94	-4.0	-23.40	-4.1
Mix	-77.69	0.2	-192.85	0.5	-23.63	1.0
Light	-78.29	0.9	-190.41	-0.8	-22.38	-4.4

	Bottom Side - Ply 1 (Bidirectional CF)					
	Leading Edge		Between Spars		Trailing Edge	
Model	σ_{WP} [Mpa]	Difference [%]	σ_{WP} [Mpa]	Difference [%]	σ_{WP} [Mpa]	Difference [%]
Resin 1	140.81	-	155.47	-	89.76	-
Resin 2	137.60	-2.3	152.06	-2.2	87.46	-2.6
Resin 3	133.43	-5.2	149.89	-3.6	85.83	-4.4
Mix	134.13	0.5	150.89	0.7	86.00	0.2
Light	134.63	0.9	150.80	0.6	84.05	-2.1

B.4 Rib 2 Maximum Stresses

Table B.8: Rib 2 plies 1, 3, and 5 maximum stresses.

	Ply 1 (Bidirectional CF) - Root Side					
	Leading Edge		Between Spars		Trailing Edge	
Model	σ_{WP} [Mpa]	Difference [%]	σ_{WP} [Mpa]	Difference [%]	σ_{WP} [Mpa]	Difference [%]
Resin 1	-23.27	-	-21.11	-	-13.65	-
Resin 2	-23.02	-1.0	-20.89	-1.0	-13.68	0.2
Resin 3	-23.12	-0.6	-20.93	-0.8	-13.90	1.8
Mix	-22.83	-1.2	-20.83	-0.5	-13.28	-4.4
Light	-22.71	-1.8	-21.04	0.5	-13.21	-5.0

	Ply 3 (Unidirectional CF)					
	Leading Edge		Between Spars		Trailing Edge	
Model	σ_{WP} [Mpa]	Difference [%]	σ_{WP} [Mpa]	Difference [%]	σ_{WP} [Mpa]	Difference [%]
Resin 1	-60.55	-	93.00	-	11.18	-
Resin 2	-59.87	-1.1	91.66	-1.4	11.47	2.6
Resin 3	-60.12	-0.7	91.67	-1.4	11.95	6.9
Mix	-59.43	-1.1	89.76	-2.1	10.92	-8.6
Light	-59.37	-1.2	90.24	-1.6	10.87	-9.1

	Ply 5 (Bidirectional CF) - Tip Side					
	Leading Edge		Between Spars		Trailing Edge	
Model	σ_{WP} [Mpa]	Difference [%]	σ_{WP} [Mpa]	Difference [%]	σ_{WP} [Mpa]	Difference [%]
Resin 1	-31.84	-	-31.05	-	-13.93	-
Resin 2	-31.67	-0.6	-30.20	-2.7	-13.97	0.3
Resin 3	-31.91	0.2	-29.67	-4.4	-14.19	1.9
Mix	-31.28	-2.0	-29.46	-0.7	-13.60	-4.2
Light	-31.23	-2.1	-29.62	-0.2	-13.53	-4.7